Scholars' Mine

Doctoral Dissertations

Student Theses and Dissertations

Spring 2017

Additive manufacturing of glass using a filament fed process

Junjie Luo

Follow this and additional works at: https://scholarsmine.mst.edu/doctoral_dissertations

Part of the Mechanical Engineering Commons

Department: Mechanical and Aerospace Engineering

Recommended Citation

Luo, Junjie, "Additive manufacturing of glass using a filament fed process" (2017). *Doctoral Dissertations*. 2565.
https://scholarsmine.mst.edu/doctoral_dissertations/2565

This thesis is brought to you by Scholars' Mine, a service of the Missouri S&T Library and Learning Resources. This work is protected by U. S. Copyright Law. Unauthorized use including reproduction for redistribution requires the permission of the copyright holder. For more information, please contact scholarsmine@mst.edu.

ADDITIVE MANUFACTURING OF GLASS USING A FILAMENT FED PROCESS

by

JUNJIE LUO

A DISSERTATION

Presented to the Faculty of the Graduate School of the

MISSOURI UNIVERSITY OF SCIENCE AND TECHNOLOGY

In Partial Fulfillment of the Requirements for the Degree

DOCTOR OF PHILOSOPHY

in

MECHANICAL ENGINEERING

2017

Approved by:
Edward C. Kinzel, Advisor
Robert G. Landers
Douglas A. Bristow
Heng Pan
Richard K. Brow

© 2017
Junjie Luo
All Rights Reserved

PUBLICATION DISSERTATION OPTION

This dissertation consists of the following five articles that have been published, submitted for publication, or will be submitted for publication as follows:

Paper I, Pages 4 – 28 have been published in ASME Journal of Manufacturing Science and Engineering.

Paper II, Pages 29 – 60 have been published in ASME Journal of Manufacturing Science and Engineering.

Paper III, Pages 61 – 86 will be submitted to Optical Engineering

Paper IV, Pages 87 – 101 have been published in the 2016 SPIE Defense and Security conference PAPER

Paper V, Pages 102 – 125 will be submitted to Materials & Design

ABSTRACT

There are many scientific and engineering applications of glass including optics, communications, electronics, and hermetic seals, there has been minimal research towards the Additive Manufacturing (AM) of transparent glass parts. The special thermal and optical properties of glasses make them hard to be printed using conventional AM techniques. In this dissertation, two different AM techniques for glass AM were developed, Selective Laser Melting (SLM) and filament fed process.

Semi-transparent parts were printed with SLM process. However, the filament fed process was found to be more robust and promising for printing optically transparent glass parts. Therefore, this dissertation is focused on filament fed process for different types of glass, including soda lime glass, fused quartz and borosilicate glass.

For soda lime glass, the optical quality of the best printed part was found to be as good as furnace cast glass part using the same type of filaments. Optical defects and refractive index inhomogeneity can be linked to the molten region temperature. Furthermore, the mechanism of bubble formation in soda lime glass printing was also studied. Different regimes of bubble formation were found corresponding with different process parameters.

Though the melting temperature of fused quartz is very high (~2300 °C), 3D fully transparent cubes with high index homogeneity were printed. For borosilicate glass, 3D fully transparent parts were printed, and the optical quality of best printed sample is as good as conventionally manufactured borosilicate glass.

ACKNOWLEDGMENTS

First and most important, I would like to express my sincere gratitude to my advisor, Dr. Edward Kinzel, for his encouragement, insightful guidance, and support during my graduate study at Missouri University of Science and Technology. He patiently guided me through all stages of my research. He encouraged me all the time to explore unknown areas and challenge myself for new achievements. His diligence and passion on research and work will have a significant influence on my whole life. It is a great honor to have worked with him.

I would like to thank Dr. Robert Landers and Dr. Douglas Bristow for their advice and help in my research. Their direction in my graduate work was invaluable and will be forever appreciated.

I would also like to extend my appreciation to my dissertation committee members, Dr. Richard Brow and Dr. Heng Pan, for serving on my dissertation examination committee and the various ways in which they assisted me in my study.

The dissertation was supported by National Science Foundation (CMMI-1538464), Missouri S&T Materials Research Center, Air Force Research Laboratory and Lockheed-Martin.

I would like to express my deep thanks to my labmates, Luke Gilbert, John Hostetler, Chuang Qu, Tao Liu, Lan Li, Daniel Peters, Arvindvivek Ravichandran, Harsh Sahu, Jacob Wilson and Carl Nelson for their support during my PhD study in Rolla.

Last but not the least, I wish to extend my special and sincere thanks to my wife Xiuzhen Fan, my parents, my parents in law, my sons Dustin and Austin, for their love and unwavering support.

TABLE OF CONTENTS

Page

SECTION

PAPER

SECTION

LIST OF ILLUSTRATIONS

Page

PAPER I

PAPER II

PAPER III

PAPER IV

PAPER V

LIST OF TABLES

Page

PAPER I

PAPER V

SECTION

1. INTRODUCTION

1.1. BACKGROUND

Additive Manufacturing (AM) is an increasingly popular technology used to create three dimensional parts using deposition processes. AM has long been used for creating structural elements where the transparency of the part was not among the important design constraints. Recently several groups have demonstrated using AM of optical components. This work has been primarily based on polymers and includes studies using ink-jet printing [1-3], ink jet printing with in-situ UV curing [4], The Selective Laser Sintering (SLS) of polymers infiltrated with indexed matched plastic in post processing [5], and multiphoton stereolithography (SLA) [6]. These process have allowed the rapid prototyping of non-imaging optics, display surfaces of arbitrary geometries, sensors, interactive devices [1-3, 7], and GRadient INdex (GRIN) devices.

While significant progresses have been made in printing transparent polymers, polymers are typically used for low cost and low power optics. Inorganic materials like glasses are widely used in high-quality, high power optics because they have high transmissivity (particularly in the ultraviolet and infrared), glasses have lower coefficients of thermal expansion and, unlike polymers, their indices of refraction are thermally stable [8]. Also, glasses are amorphous and do not present crystalline boundaries for scattering.

Compared to polymers, glasses have significantly higher processing temperature, and they are brittle that they are easy to crack in cooling process. These limitations makes AM of glass much more challenging. In recent years, several techniques have been developed for printing of transparent glass. The SLS process has been used to print fused quartz [9], borosilicate [10], and soda-lime glasses [11, 12]. Extrusion techniques have been used to print bone scaffolds of bioactive glass [13], and to print pattern colored glass [14]. Marchelli et al. have demonstrated printing glass using an inkjet method with a maltodextrin binder that was burnt out in post processing [15]. These studies have focused on the ability to create dimensionally accurate glass parts, but rely on an organic binder that must be burnt-out in post processing. This leads to small gas inclusions which act as scattering sites and leave the final parts not transparent. Luo et al. previously showed that a continuous filament fed process was capable of printing fully dense and optically transparent soda lime glass [12]. This process is similar to the AM Fused Deposition Modeling (FDM) process for depositing thermoplastics and laser wire-deposition processes used in metal AM [16]

1.2. RESEARCH OBJECTIVES

The objective of this study is to create a system for printing optically transparent glass. In this dissertation, two different techniques for glass AM have been studied.

The first technique is Selective Laser Melting (SLM) of soda lime glass. Optimal parameters were determined for scanning single tracks in a powder bed. Moreover, semi-transparent glass walls were printed, which shows the potential for printing fully transparent glass parts using powder bed process. Additionally, the SLM technique was compared with a wire fed process in this study. The filament fed process appears to be more robust and promising for printing optically transparent glass parts.

Since filament fed process was proved to be a better solution for AM of glass, this dissertation is focused on filament fed process for different types of glass, including soda lime glass, fused quartz and boroslicate glass. An experimental system was developed for this technique. In this system, a 125 W CW CO_2 laser is used to locally melt a glass filament fed into a melt pool, glass substrates are clamped to a heater, which is positioned on a set of numerically controlled 3-axis stages.

Paper II presents the filament fed process for soda lime glass printing. The optical quality of the best printed part was found to be as good as furnace cast glass part using the same type of filaments. Optical defects and refractive index inhomogeneity can be linked to the molten region temperature illustrating that insufficient heating produces striaes, and excessive heating in the molten region generates bubbles. Furthermore, the mechanism of bubble formation in soda lime glass printing was also reported in Paper IV Different regimes of bubble formation were found.

In Paper III, filament fed printing of fused quartz was studied. 3D solid transparent cubes were printed. The numerical model that considers both energy and mass balance agrees with the experimental results, therefore it can predict the occurrence of vaporization.

Paper V describes filament fed printing of borosilicate glass. 3D fully transparent parts were printed, and the optical quality of best printed sample is as good as conventionally manufactured borosilicate glass. Moreover, samples with cylindrical surfaces were printed by overlapping of three monolayers. The optical measuring result shows that these samples can function as cylindrical lenses.

PAPER

I. ADDITIVE MANUFACTURING OF GLASS

Junjie Luo, Heng Pan and Edward C. Kinzel
Department of Mechanical and Aerospace Engineering
Missouri University of Science and Technology, Rolla, Missouri 65409, U.S.A

ABSTRACT

Selective Laser Melting (SLM) is a technique for the additive manufacturing of metals, plastics and even ceramics. This paper explores using SLM for depositing glass structures. A CO_2 laser is used to locally melt portions of a powder bed to study the effects of process parameters on stationary particle formation as well as continuous line quality. Numerical modeling is also applied to gain insight into the physical process. The experimental and numerical results indicate that the absorptivity of the glass powder is nearly constant with respect to the processing parameters. These results are used to deposit layered single-track wide walls to demonstrate the potential of using the SLM process for building transparent parts. Finally, the powder bed process is compared to a wire-fed approach. Additive manufacturing of glass is relevant for gradient index optics, systems with embedded optics, and the formation of hermetic seals.

1. INTRODUCTION

Additive Manufacturing (AM) has drawn significant attention as it moves from rapid prototyping to the fabrication of production parts. Powder bed processes such as Selective Laser Sintering (SLS) or Selective Laser Melting (SLM) are among the most popular techniques for making complex 3D parts directly from CAD models. In these processes, a laser beam is scanned relative to the powder bed. The laser locally heats the powder, melting it (or partially melting it in the case of SLS) which causes the powder to coalesce. The unprocessed powder is removed to reveal the solid part. Besides partial and full melting there are three other consolidating mechanisms for SLS and SLM technologies; solid state sintering, chemical induced binding, liquid-state sintering [1]. The SLS/SLM process has been widely studied for manufacturing metal parts, such as iron based alloys [2-3], steels [4-11], aluminum alloys [12-13], magnesium [14], titanium alloys [15-17], copper alloys [8,18]. It can also be used in sintering/melting ceramic parts [19-22], glasses [23-26] and polymers [27-29].

A critical challenge for metal and ceramics powder SLS/SLM processing is the densification of the parts [8, 19]. With the correct processing parameters, densities as high as 99% in SLM process have been reported [13,16] and SLM produced parts can have mechanical properties comparable or even exceeding those of conventionally cast parts [13]. This success has seen the use of SLM for AM of production parts in the aerospace and medical industries albeit at low volumes. SLS/SLM has also been applied to fabricate parts with low density and high porosity. This is particularly useful for replacement of bone because the pores provide space for bone tissues to grow [17].

The properties of additively manufactured parts depend strongly on each layer and in turn on each laser-melted track. For example, Yadroitsev et al. [9] studied the single track melting in metal powder SLM process. They explored effects of the processing parameters to show a considerable negative correlation between the thermal conductivity of bulk material and the range of optimal scanning speed for the continuous single track melting. In determining the optimal parameters for stainless steel powders, Childs et al. [10] showed that the absorptivity changes with the scanning speeds. Sammons et. al [11] set up a model that dynamically related the process inputs (laser power, material mass flow rate, and scan speed) to the melt pool dimensions and temperature. Similar studies have been applied to ceramic powders. Yves-Christian et al. [20] studied net-shape forming of Al_2O_3-ZrO_2 parts using SLM and demonstrated the effectiveness of preheating the powder bed prior to laser exposure.

Glass has widespread applications such as windows, optics (imaging and non-imaging) and hermetic seals. Traditionally, glass powder is melted in a furnace, and cast in molds to form specific shapes. There is comparatively little literature available about additive manufacturing of glasses. SLM was proposed for fabricating structures on Mars from indigenous materials [30] and researchers from HP experimented with extruding glass fritted polymers [31]. Several references have reported on laser sintering ceramics and glasses using low melting temperature binders to form composites. This has included ammonium phosphate [21], UCAR 430 Acrylic Polymer Latex [22], monoclinic HBO_2 [23]. Marchelli et al. [24] studied 3D printing of glass using maltodextrin as a binder which could be burned out in a kiln. Klocke et al. [25] studied laser sintering borosilicate glass volumes including post deposition densification in a furnace. While these studies demonstrate the ability to form solid glass/ceramic parts, the parts were not transparent. On the other hand, Niino et al. [29] demonstrated forming transparent polymer parts by infiltrating high porosity SLS deposited resin blocks with index matched plastic. The physical properties of glass are significantly different from metals or plastics. Glasses typically have much lower thermal conductivity and many orders of magnitue greater viscosity in the liquid phase than metals [32]. In addition, glass is a brittle material which leads to cracking due to thermal fracture [33]. Finally, soda-lime glass is transparent in the visible and near-IR [34] which creates processing issues with lasers commonly used in SLM/SLS.

In this paper, we apply the SLM process to soda-lime glass. We start by using a stationary laser beam to form isolated particles. This shows that the melted volume scales with the energy input. Next we experiment with single track scanning and identify the parameter sets required for the deposition of continuous lines. Both stationary and scanned melting are modeled numerically which helps to understand the results. Finally, solid walls are built using a powder bed process. These results are compared to those achieved using a wire fed process. This demonstrates that transparent parts can be built using powder bed SLS but it is more straightforward to start with a fully dense glass filament.

2. EXPERIMENTAL SETUP

Figure 2.1 shows a schematic of the experimental setup. The powder bed is 5×5 cm^2 and 0.25 cm deep. It is supported on a refractory block which is positioned by 3-axis numerically controlled stages (direct-drive brushless servo motors in x and y with a lab-jack pantograph type mechanism in z) under a fixed focus laser beam. While soda lime glass is nearly transparent at visible and near-IR wavelengths, it is opaque with low reflection to long-wave infrared radiation (7-14 μm) [34]. For this reason we use a continuous wave Coherent GEM100 CO_2 laser (λ=10.6 μm) to locally heat the glass. The laser is focused onto the surface of the powder bed with an *f*/3 lens. The FWHM diameter of the beam is measured to be 70 μm at its focus. Spherical soda lime glass particles (diameters ranging from 1-37 μm) from the Mo-Sci Corporation are used throughout this study.

Particle melting: The glass powder is irradiated by the laser beam with the stage in a fixed location. The temperature rises to the point that the powder softens and fuses, coalescing to form a small particle. Conduction away from the melted region also heats the surrounding material and surface tension draws surrounding powder into the particle. Experimentally, the laser power was adjusted between 10 and 40 W while the exposure duration ragned from 0.1 and 20 s. The beam was focused to a size of 70 μm for the experiment. The diameter of the melted region was measured with an optical microscope.

Single track melting: The powder bed was scanned in one direction under the laser beam. The height of the stage was adjusted relative to the fixed laser focus to produce three different beam sizes, 70 μm, 200 μm and 350 μm. At each beam size, lines were drawn at different scan speeds ranging from 0.5 to 100 mm/s. The laser power was adjusted from 10 to 50 W. The track width was measured using an optical microscope prior to removing the fused material from the powder bed.

Glass walls: Glass walls were fabricated by melting single tracks in a powder bed layer-by-layer. After each track was written, the stage was lowered and powdered glass was leveled to form a new layer. We also added an electrical strip heater to the substrate which minimizes temperature gradients in the workpiece. Finally, we introduce an alternative wire-fed process. After deposition the pieces were polished with 1 µm grid cloth to observe their transmission characteristics.

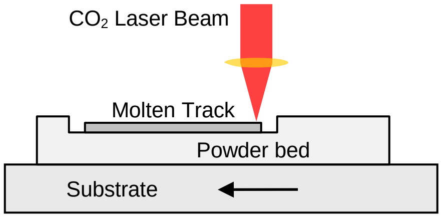

Figure 2.1 Illustration of powder bed SLM setup.

3. NUMERICAL MODELING

There are two principal numerical methods to model the melting process; Finite Element Method (FEM) and Finite Volume Method (FVM). FEM models generally only model the conduction heat-transfer. Melting and coalescence are accounted for by locally changing the density and specific heat when the temperature exceeds the melting point. This approach was used by Shiomi et al. to model the balling process of metal powder laser melting [35] and by Childs et al. to simulate the single track melting process with metal and polymer powders [10,36]. Paul et al. [37] studied thermal deformation on part errors in metal powder based additive manufacturing by a three-dimensional thermomechanical FEM model. It is important to note that the fluid dynamics of the melting process is neglected in FEM.

FVM also simulates the heat transfer but includes the melting and re-solidification process to capture the liquid motion within the melt pool. This is handled numerically by incorporating the enthalpy of fusion into the specific heat leading to a mushy zone. The Volume of Fluid (VOF) model can also be incorporated into a FVM model and used to track the free surface of the melt pool. VOF is widely used to simulate welding, for example, Tsai et al. used FVM with VOF to model the laser keyhole welding, arc welding, gas tungsten arc welding and MIG welding processes [38-41]. Zhang et al. presented a model of the SLS process of two-component metal powders by FVM [42-43]. An FEM and FVM coupled model, which can predict laser welding geometry formation and joint strength, was created by Marimuthu et al. [44]. Jamshidinia et al. [45] and Mahamood et al. [46] also modeled melting process of metal powder by FVM.In this paper, we use ANSYS Fluent 14, a commercial FVM solver to model the melting process. The solidification/melting model calculates the liquid fraction throughout the whole domain based on the temperature (not using the VOF method). As in the experiment, the size of the melted region of the powder bed was measured at different laser powers and exposure durations or scanning speeds. The following assumptions were made to simplify the analysis of glass circulation and heat transfer:

1) The molten glass acts is an incompressible, homogeneous, and Newtonian fluid.
2) Variation of glass composition in the melting process is neglected and chemical reactions are neglected. This ignores the effects of any evaporation of volatile species from the glass surface, or the presence of gas bubbles on the thermal physical properties [32];
3) The density does not change with temperature after coalescence.
4) Glass is opaque to the laser beam with a constant absorptivity which allows the laser beam to be modeled as a heat flux
5) Radiation heat transfer within the glass is neglected.

Given these assumptions and material properties the governing equations for modeling molten glass can be expressed as:

Continuity Equation:

$$\frac{\partial \rho}{\partial t} + \nabla \cdot \left(\rho \vec{v} \right) = 0 \tag{1}$$

Momentum Equation:

$$\rho \frac{D\vec{v}}{Dt} = \nabla \cdot \left(\mu \nabla \vec{v} \right) - \nabla p + \rho g \tag{2}$$

Energy Equation:

$$\rho c_p \left(\frac{\partial T}{\partial t} + \vec{v} \cdot \nabla T \right) = \nabla \cdot \left(k \nabla T \right) \tag{3}$$

where ρ, $\vec{v}$, p, T, μ, k, g and t denote the density, velocity vector, pressure, temperature, dynamic viscosity, heat conductivity and time respectively. All of the thermal properties except for the density, ρ, are functions of the local temperature. Outside the molten region the velocity vector is equal to zero, and the equations reduce to the heat diffusion equation. The thermal properties of soda lime glass powder used for the numerical study are shown in Table 3.1. This neglects the porosity of the glass powder bed by initially modeling it as solid glass. However, this is not as significant as in metal powder bed processes because there is less of a mismatch between the properties of glass and air, specifically the thermal conductivity.

Table 3.1 Thermal properties of soda lime glass [32]

ρ (kg/m^3)	1400	Powder state
	2500	Molten
μ (Pa·s)	$10^{\left(-1.626+\frac{4236}{T{}^{\circ}C-266}\right)}$	
c_p (J/kg·K)	1256	
k (W/m·K)	1.5	Powder state
	3.5–4.5	Molten

Boundary conditions: The laser beam is treated as a heat flux on the top surface of the powder bed. It follows a Gaussian distribution [47] with heat flux, q”, given by

$$q'' = \alpha \frac{2P}{\pi r_0^2} \exp\left[-2\left(r/r_0\right)^2\right] \tag{4}$$

where P is the laser power, α is the absorptivity, r_0 is the laser beam waist, r is the distance from the beam center. The boundary condition of the exposed face of the glass is

$$-k\frac{\partial T}{\partial n} = h\left(T_\infty - T\right) + \varepsilon\sigma\left(T_\infty^4 - T^4\right) + q'' \tag{5}$$

which includes convection, radiation, and the laser energy input. In this equation, *n* represents the direction of heat transfer. On the side surfaces and far away from the center of the laser beam the *q''* term is absent. The substrate rests on a piece of thermal insulation material so the lower boundary is treated as adiabatic.

4. RESULTS AND DISCUSSION

4.1. PARTICLE MELTING

Figure 4.1 how the melted particle's diameter, d, varies with the exposure duration and laser power. Four particles were made under each set of experimental conditions, and the error bars denote the minimum and maximum diameters. Surface tension causes the particles to coalesce to a nearly spherical shape with volume roughly proportional to d^3. The thermal energy imparted to the system varies with the laser power and the exposure duration, $E=P\times\tau$. A good first order approximation is that the melted volume is proportionate to the thermal energy. For longer exposure lengths there is more time for the heat to diffuse without melting the glass. In addition some powder will agglomerate to the outside of the sphere without fully melting. The linear relationship of power to volume implies that the absorptivity is insensitive to the temperature of the melt pool (which would be higher for larger powers) as well as other parameters in the study.

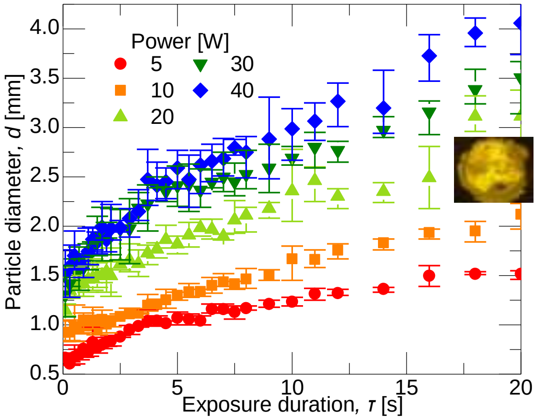

Figure 4.1 Experimental results showing particle diameter as a function of exposure duration and laser power. The image in the inset shows the result for P=10W and τ=1 s

Figure 4.2 shows the particle diameter determined from simulation where the size of the particle was determined by the molten region at a given time. The numerical model shows similar trends to the experimental results, however, on average the simulation underestimates the diameter by a factor of 0.76. The numerical model neglects heat diffusion and melting after the end of the heat pulse. Another contributing factor is that in the experiment, unmelted powder coming into contact with the melt pool becomes attached and fused to the particle increasing its diameter.

4.2. SINGLE TRACK MELTING

Depending on the laser power, scanning speed, and beam size, we identify four regimes. Tracks are either (A) continuous lines (B) discontinuous line; (C) discrete particles; (D) only partially melted. When the scanning speed is high and the power is sufficiently low, there is no observable change to the powder bed. To vary the beam size the height of the powder bed is adjusted relative to the fixed focus of the laser beam to give measured beam diameters of 70 μm, 200 μm, and 350 μm.

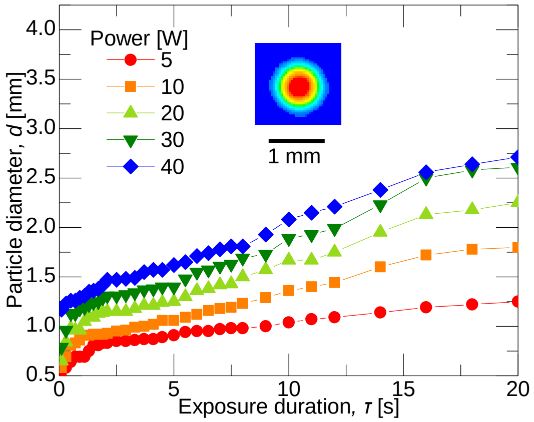

Figure 4.2 Particle diameter as a function of exposure duration and laser power from simulation.

Figure 4.3 shows the experimental parameters leading to each of the four regimes. At each height there is an optimal region that produces continuous lines. Generally this regime is broader for the smaller, tighter focused beam. At a given scan speed, as the power increases the melt pool becomes unstable and the track breaks up to form discrete particles. The shape of particles is irregular and they form at irregular intervals. When the power is lower than the continuous range, the track is also discontinuous but forms regular round shaped particles at regular intervals. Figure 4.3 shows that the range of parameters producing continuous lines is broadest for the focused beam with the smallest diameter, shrinking as the beam size is expanded.

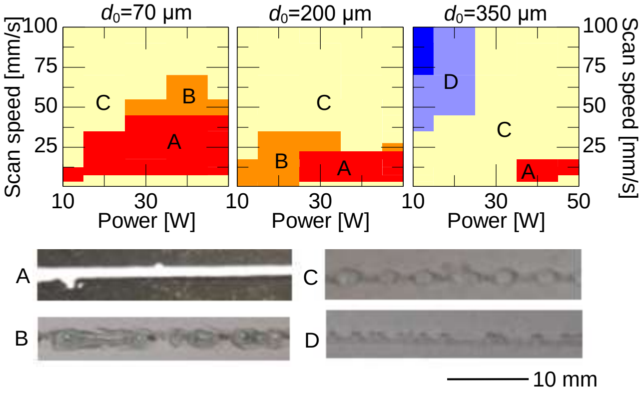

Figure 4.3 Shape distribution of tracks: (a) beam size 75 µm; (b) beam size 200 µm; (c) beam size 350 µm; (d) photographs of different track regimes

The width of the continuous lines decreases with increasing scan speed or decreasing power. This is shown in Figure 4.4. The volume of the continuous track is proportional to the square of the width and scales with the ratio of the power to the scan speed. This relationship is similar to what was observed for the particle melting experiments. In both cases the volume is linearly dependent on the energy intensity which supports the assumption that the absorptivity of glass to the CO_2 laser is insensitive to temperature.

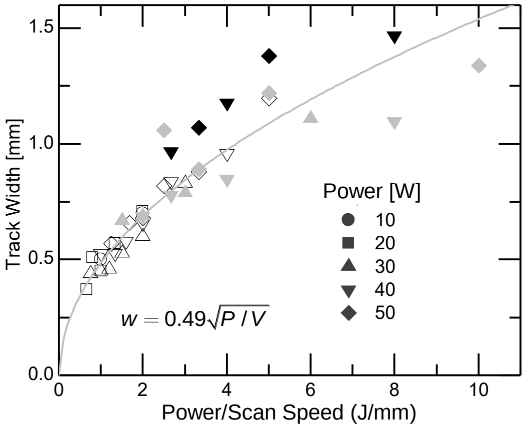

Figure 4.4 Continuous line width distribution. White, gray, and black correspond to a beam sizes of 70 μm, 200 μm and 350 μm, respectively.

For all three beam sizes, all continuous tracks are in the width range of 0.5-1.5 mm which defines the line-to-line pitch for building continuous parts. For larger beam diameters, there is no set of scan speeds that produce continuous tracks at low power (10W, 20W) because the peak energy intensity of the laser beam is insufficient to deposit continuous tracks.

Figure 4.5 shows simulation results of the scanned tracks for a beam diameter of 70 μm. As would be expected the maximum temperature in the melt pool decreases with high scan speed and lower power. The peak temperature of the melt pool exceeds 2000 K for most points, indicating that vaporization would occur within the melt pool. In the experiment we observe the presence of visible fumes rising from the melt pool under these conditions. The model does not capture the instability leading to the breakup of the melt pool and all lines in the simulation are continuous. For example, when the parameters that produced discrete particles in the experiment (regime C) are simulated, the resulting track width is smaller than the continuous lines. The model does adequately predict the experimental width of the lines in the continuous regime (A) to a difference of less than 100 µm.

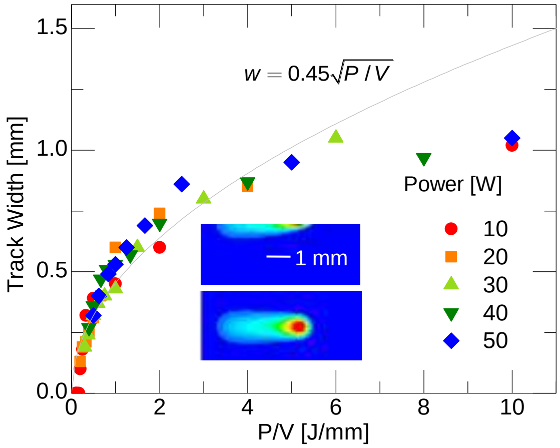

Figure 4.5 Numerical modeling of single track scanning with inset showing temperature profile in the powder bed.

4.3. GLASS WALLS

The next step was to deposit a simple 1-track wide wall layer-by-layer. After each track was written the workspace was lowered and a fresh layer of powder spread over the powder bed. This introduces the additional parameter of the layer thickness, *s*. Figure 4.6(a) shows a photograph of a wall built with a layer-to-layer thickness of *s*=1 mm using laser power of 50W and a scanning speed of 20 mm/s with a beam spot size of 70µm. These parameters created consistent tracks with a width of 0.8 mm (shown in Figs. 4.3 and 4.4). The part in the figure was 10 layers thick and was not transparent. In addition, it proved to be brittle and broke apart into smaller pieces during polishing. The inset of

Figure 4.6(a) shows one piece after polishing both sides to remove the sides. Porosity and small cracks in the part lead to significant scattering limiting transparency.

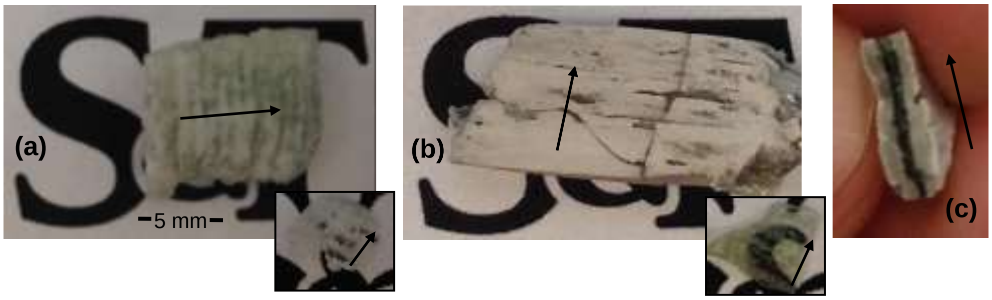

Figure 4.6 Wall built using powder bed process (a) 1 mm layer thickness (b) 0.5 mm layer thickness and (c) side view of 0.5 mm parts. Photographs are as deposited while insets show a portion of the same parts after cutting and polishing. The arrows indicate the build direction.

Much of the cracking was due to thermal stresses created in the part during the deposition process. The wall in Figure 4.6(a) was deposited without heating the underlying substrate which led to large thermal gradients in the glass between the top and bottom of the part. This demonstrates the need for annealing to relieve stresses in the part.

Figure 4.6(b) and (c) show a part built on a substrate held at 530°C. It was deposited using the same laser/speed parameters as Figure 4.6(a) but with a thinner layer-to-layer thickness of h=0.5 mm. In addition, following deposition the piece was surrounded with an insulating fiber blanket to allow it to cool to room temperature gradually over about an hour. Despite this partial annealing step the part still broke during polishing. However, the polished piece (shown in the inset of Figure 4.6(b)) demonstrates significant transparency. Figure 4.6(c) shows that the transparent core is sandwiched between two thick layers of partially fused glass. It is only in this transparent core where the temperature is sufficient to melt and fully fuse the glass. Air bubbles become trapped in the partially melted glass and cannot escape due to the high viscosity of the lower temperature glass. This is a larger issue for thicker layer heights and led to the lack of transparency of the piece in Figure 4.6(a).

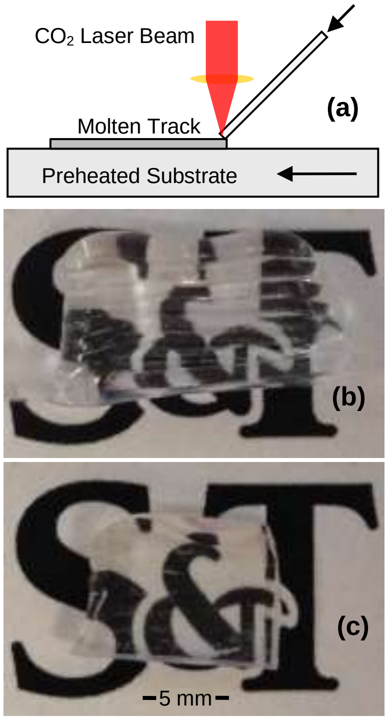

Figure 4.7 Illustration of wire-fed process and photographs of part (b) as deposited (c) after cutting and polishing.

We also experimented with feeding a glass filament into the melt pool. The filament was fully dense and could be melted and fused to previous layers. Figure 4.7 illustrates this process. In this work, the filament was a 1 mm diameter glass stringer (Bullseye Glass Co.) and was fed by hand at ~1 mm/s. The laser power was set to 25 W and the stage was scanned at 1 mm/s. The substrate for this experiment was a glass microscope slide and was maintained at a temperature of 530°C throughout the experiment. The sample was also allowed to cool gradually. These steps permit deposition of large pieces without cracking. Figure 4.7(b) shows the piece as deposited and Figure 4.7(c) shows the same piece after polishing. These results show a continuous transparent piece that is much more robust than the powder bed results. It is worth noting that in addition to having a smooth free surface, the wire-fed process is more conducive to locally varying the composition of the melt pool which will be advantageous for gradient index optics.

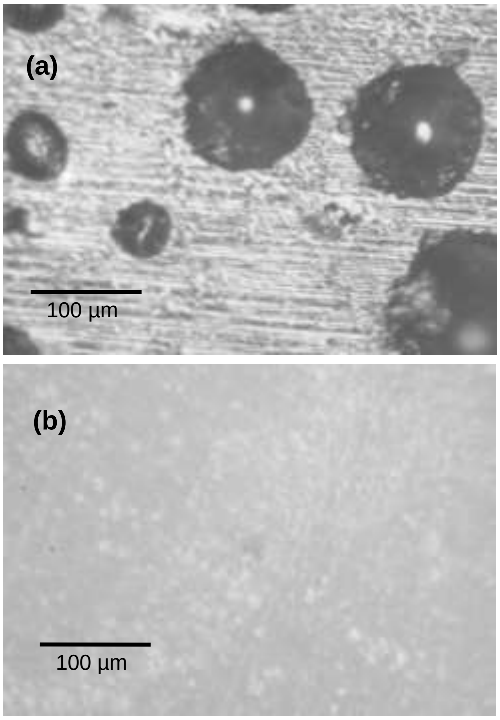

Figure 4.8 Micrographs of polished surfaces (a) powder bed part shown with 1 mm layer thickness and (b) wire fed part.

Figure 4.8 shows brightfield reflected light microscope images of the polished samples in Figure 4.6(a) and Figure 4.7(c). The sample produced with the powder bed process has a significant portion of the image covered by bubbles which scatter light. The wire fed process produces a smoother surface without the inclusions. It was possible to heat the melt pool to the point that convection within the molten region becomes violent due to boiling. However, moderate heating successfully softens the glass to the point that it bonds with the underlying layers without trapping air. These results suggest starting with fully dense feedstocks will be a more direct way of manufacturing optical quality components using additive manufacturing

5. CONCLUSION

This paper explored melting soda lime glass using a CO_2 laser for additive manufacturing. Generally the deposited volume is proportional to the laser energy incident on the glass for both stationary and scanned experiments. Optimal parameters were determined for scanning single tracks in a powder bed. Both experiments were simulated in al regimes which estimate the volume of melted powder. These results were the basis for building walls using a powder bed process. This showed the importance of layer height and controlling the temperature profile within the heated part. Finally these results were compared with a wire fed process using a fully dense starting material. Both approaches are shown to have the potential for depositing optically transparent parts using additive manufacturing. However, the wire-fed process appears to be more robust and promising.

ACKNOWLEDGMENT

The authors are grateful for useful discussions with Dr. Clara Rivero-Baleine (Lockheed-Martin) and Dr. Hai-Lung Tsai (Missouri S&T). In addition the authors are also very thankful to Dr. Glenn Boreman (UNCC), who in addition to giving useful feedback, provided the laser used in this work.

REFERENCES

[1] Kruth, J. P., Levy, G., Klocke, F., and Childs, T. H. C., 2007, "Consolidation phenomena in laser and powder-bed based layered manufacturing," CIRP Annals - Manufacturing Tech., 56(2), pp. 730-759.

[2] Kruth, J. P., Froyen, L., Van Vaerenbergh, J., Mercelis, P., Rombouts, M., and Lauwers, B., 2004, "Selective laser melting of iron-based powder," J. of Materials Processing Tech., 149(1-3), pp. 616-622.

[3] Rombouts, M., 2006, Selective laser sintering/melting of iron-based powders, Katholieke Universiteit Leuven.

[4] Badrossamay, M., and Childs, T. H. C., 2007, "Further studies in selective laser melting of stainless and tool steel powders," Int. J. of Machine Tools and Manufacture, 47(5), pp. 779-784.

[5] Childs, T., Hauser, C., and Badrossamay, M., 2005, "Selective laser sintering (melting) of stainless and tool steel powders: experiments and modeling," Proc. of the Institution of Mechanical Engineers B, 219(4), pp. 339-357.

[6] Hao, L., Dadbakhsh, S., Seaman, O., and Felstead, M., 2009, "Selective laser melting of a stainless steel and hydroxyapatite composite for load-bearing implant development," J. of Mat. Processing Technology, 209(17), pp. 5793-5801.

[7] Xie, F., He, X., Cao, S., and Qu, X., 2013, "Structural and mechanical characteristics of porous 316L stainless steel fabricated by indirect selective laser sintering," J. of Mat. Processing Technology, 213(6), pp. 838-843.

[8] Rombouts, M., Kruth, J. P., Froyen, L., and Mercelis, P., 2006, "Fundamentals of Selective Laser Melting of alloyed steel powders," CIRP Annals - Manufacturing Technology, 55(1), pp. 187-192.

[9] Yadroitsev, I., et al., 2010, "Single track formation in selective laser melting of metal powders," J. of Materials Processing Tech., 210(12), pp. 1624-1631.

[10] Childs, T. H. C., Hauser, C., and Badrossamay, M., 2004, "Mapping and Modelling Single Scan Track Formation in Direct Metal Selective Laser Melting," CIRP Annals - Manufacturing Technology, 53(1), pp. 191-194.

[11] Sammons, P. M., Bristow, D. A., and Landers, R. G., 2013, "Height Dependent Laser Metal Deposition Process Modeling," ASME J. Manuf. Sci. Eng., 135(5), pp. 054501-054501.

[12] Buchbinder, D., Schleifenbaum, H., Heidrich, S., Meiners, W., and Bültmann, J., 2011, "High Power Selective Laser Melting (HP SLM) of Aluminum Parts," Physics Procedia, 12, pp. 271-278.

[13] Kempen, K., Thijs, L., Van Humbeeck, J., and Kruth, J. P., 2012, "Mechanical Properties of AlSi10Mg Produced by Selective Laser Melting," Physics Procedia, 39, pp. 439-446.

[14] Taltavull, C., Torres, B., López, A. J., Rodrigo, P., Otero, E., and Rams, J., 2012, "Selective laser surface melting of a magnesium-aluminium alloy," Materials Lett., 85, pp. 98-101.

[15] Leuders, S., Thöne, M., Riemer, A., Niendorf, T., Tröster, T., Richard, H. A., and Maier, H. J., 2013, "On the mechanical behaviour of titanium alloy TiAl6V4 manufactured by selective laser melting: Fatigue resistance and crack growth performance," Int. J. of Fatigue, 48, pp. 300-307.

[16] Vandenbroucke, B., and Kruth, J.-P., 2007, "Selective laser melting of biocompatible metals for rapid manufacturing of medical parts," Rapid Prototyping Journal, 13(4), pp. 196-203.

[17] Warnke, P. H., et al., 2008, "Rapid prototyping: porous titanium alloy scaffolds produced by selective laser melting for bone tissue engineering," Tissue engineering C: Methods, 15(2), pp. 115-124.

[18] Tang, Y., Loh, H. T., Wong, Y. S., Fuh, J. Y. H., Lu, L., and Wang, X., 2003, "Direct laser sintering of a copper-based alloy for creating three-dimensional metal parts," J. of Mat. Processing Technology, 140(1), pp. 368-372.

[19] Shishkovsky, I., Yadroitsev, I., Bertrand, P., and Smurov, I., 2007, "Alumina–zirconium ceramics synthesis by selective laser sintering/melting," Appl. Surface Science, 254(4), pp. 966-970.

[20] Yves-Christian, H., Jan, W., Wilhelm, M., Konrad, W., and Reinhart, P., 2010, "Net shaped high performance oxide ceramic parts by selective laser melting," Physics Procedia, 5, pp. 587-594.

[21] Lakshminarayan, U., Ogrydiziak, S., Marcus, H. L., 1990, " Selective Laser Sintering of Ceramic Materials," Solid Freeform Fabrication Symposium Proceedings, Austin, Texas, pp. 16- 26.

[22] Vail, N. K., & Barlow, J. W., 1991, " Effect of Polymer coatings as intermediate binders on Sintering of Ceramic parts," Solid Freeform Fabrication Symposium Proceedings, Austin, Texas, pp. 195-204.

[23] Lee, I., Manthiram, A., & Marcus, H. L., 1995, "Selective Laser Sintering of Alumina-Zinc Borosilicate Glass Composites using Monoclinic HB02 as a Binder," Solid Freeform Fabrication Symposium Proceedings, Austin, Texas, pp. 46- 54.

[24] Marchelli,G., Storti, D., Ganter,M., Prabhakar, M., 2010, "An Introduction to 3D Glass Printing," Solid Freeform Fabrication Symposium Proceedings, Austin, Texas, pp. 95-107.

[25] Klocke, F., McClung, A., & Ader, C., 2004, “Direct laser sintering of borosilicate glass,” Solid Freeform Fabrication Symposium Proceedings, Austin, Texas, pp. 214-219.

[26] Quadrini, F., and Santo, L., 2008, "Selective laser sintering of resin-coated sands—part i: the laser-material interaction," ASME J. Manuf. Sci. Eng., 131(1), pp. 011004-011004.

[27] Kandis, M., and Bergman, T., 2000, "A simulation-based correlation of the density and thermal conductivity of objects produced by laser sintering of polymer powders," ASME J. Manuf. Sci. Eng., 122(3), pp. 439-444.

[28] Mazzoli, A., Moriconi, G., and Pauri, M. G., 2007, "Characterization of an aluminum-filled polyamide powder for applications in selective laser sintering," Materials & Design, 28(3), pp. 993-1000.

[29] NIINO, T., YAMADA, H., 2009, “Fabrication of transparent parts by laser sintering process,” Journal of the Japan Society for Precision Engineering, 75(12), pp. 1454-1458

[30] Fateri, M., and Khosravi M., 2012, “On-site additive manufacturing by selective laser melting of composite objects,” Concepts and Approaches for Mars Exploration, Houston TX, 4368.

[31] Klein, S. Simske, S., Parraman, C. Walters, P. Hunson, D. and Hoskins, S. 2012, “3D Printing of transparent glass,” Hewlett-Packerd Development Company Technical Report (www.hpl.hp.com/techreports/2012/HPL-2012-198.pdf)

[32] Napolitano, A. and Hawkins, E.G., 1964. “Viscosity of a standard soda-lime-silica glass,” J. Res. Nat. Bur. Stand. A. A, 68, pp.439-48.

[33] Wiederhorn, S. M., 1969, "Fracture surface energy of glass," Journal of the American Ceramic Society, 52(2), pp. 99-105.

[34] Rubin, M., 1985, "Optical properties of soda lime silica glasses," Solar Energy Materials, 12(4), pp. 275-288.

[35] Osakada, K., and Shiomi, M., 2006, "Flexible manufacturing of metallic products by selective laser melting of powder," International Journal of Machine Tools and Manufacture, 46(11), pp. 1188-1193.

[36] Childs, T., and Tontowi, A., 2001, "Selective laser sintering of a crystalline and a glass-filled crystalline polymer: experiments and simulations," Proc. of the Institution of Mechanical Engineers, B, 215(11), pp. 1481-1495.

[37] Paul, R., Anand, S., and Gerner, F., 2014, "Effect of thermal deformation on part errors in metal powder based additive manufacturing processes," ASME J. Manuf. Sci. Eng., 136(3), pp. 031009-031009.

[38] Zhou, J., Tsai, H.-L., and Wang, P.-C., 2006, "Transport phenomena and keyhole dynamics during pulsed laser welding," J. of Heat Transfer, 128(7), p. 680.

[39] Xu, G., Hu, J., and Tsai, H. L., 2008, "Three-dimensional modeling of the plasma arc in arc welding," J. of Appl. Phys., 104(10), p. 103301.

[40] Zhou, J., and Tsai, H. L., 2008, "Modeling of transport phenomena in hybrid laser-MIG keyhole welding," Int. J. of Heat and Mass Transfer, 51(17-18), pp. 4353-4366.

[41] Xu, G., Hu, J., and Tsai, H. L., 2012, "Modeling three-dimensional plasma arc in gas tungsten arc welding," ASME J. Manuf. Sci. Eng., 134(3), pp. 031001-031001.

[42] Chen, T., and Zhang, Y., 2006, "Three-Dimensional Modeling of Selective Laser Sintering of Two-Component Metal Powder Layers," ASME J. Manuf. Sci. Eng., 128(1), p. 299.

[43] Zhang, Y., Faghri, A., Buckley, C. W., and Bergman, T. L., 1999, "Three-dimensional sintering of two-component metal powders with stationary and moving laser beams," Journal of Heat Transfer, 122(1), pp. 150-158.

[44] Marimuthu, S., Eghlio, R. M., Pinkerton, A. J., and Li, L., 2013, "Coupled computational fluid dynamic and finite element multiphase modeling of laser weld bead geometry formation and joint strengths," ASME J. Manuf. Sci. Eng., 135(1), pp. 011004-011004.

[45] Jamshidinia, M., Kong, F., and Kovacevic, R., 2013, "Numerical modeling of heat distribution in the electron beam melting® of ti-6al-4v," ASME J. Manuf. Sci. Eng., 135(6), pp. 061010-061010.

[46] Mahamood, R. M., Akinlabi, E. T., Shukla, M., and Pityana, S., 2013, "Characterizing the effect of laser power density on microstructure, microhardness, and surface finish of laser deposited titanium alloy," ASME J. Manuf. Sci. Eng., 135(6), pp. 064502-064502.

[47] Steen, W. M. and Mazumder J., 2010, Laser material processing. Springer, London UK.

II. ADDITIVE MANUFACTURING OF TRANSPARENT SODA-LIME GLASS USING A FILAMENT-FED PROCESS

Junjie Luo, Luke J. Gilbert, Chuang Qu, Robert G. Landers, Douglas A. Bristow, Edward C. Kinzel
Department of Mechanical and Aerospace Engineering
Missouri University of Science and Technology, Rolla, Missouri 65409, U.S.A

ABSTRACT

Although there are many scientific and engineering applications of glass including optics, communications, electronics, and hermetic seals, there has been minimal research towards the Additive Manufacturing (AM) of transparent glass parts. This paper demonstrates a filament-fed technique for AM of transparent glass. A transparent glass filament is melted by a CO_2 laser and solidifies as the workpiece is translated relative to the stationary laser beam. To prevent thermal shock, the workpiece rests on a heated build platform. In order to obtain optically transparent parts, several challenges must be overcome, notably producing index homogeneity and avoiding bubble formation. The effects of key process parameters on the morphology and transparency of the printed glass are explored experimentally. These results are compared to a low order model relating the process parameters to the temperature of the molten region, which is critical to the quality of the deposited glass. At lower temperatures, the glass is not fully melted, resulting in index variations in the final part, while at higher temperatures, phase separation introduces bubbles and other defects into the part. The correct process avoids these issues and deposits optically transparent glass.

1. INTRODUCTION

Additive Manufacturing (AM) describes the technology used to fabricate three-dimensional parts using layer-by-layer deposition. This technology permits arbitrary geometries to be built directly from digital 3D models. Additive Manufacturing offers advantages in design versatility, rapid realization of low production volumes, the ability to deposit materials that are difficult to process using subtractive methods, and the possibility of combining multiple materials in a single build. Additive Manufacturing is most often used for creating structural elements and, thus, there is limited published work on AM for parts where optical properties are the primary consideration. Due to the advantage of AM, it is worthwhile to apply AM techniques in printing of transparent optical materials. Compare Processes that have been demonstrated for printing optically transparent polymers include ink-jet printing [1-3], ink-jet printing with in-situ UV curing [4], Selective Laser Sintering (SLS) with post process infiltration of an index matched plastic [5], and multiphoton stereolithography (SLA) to directly polymerize resin [6]. These techniques have been used for rapid prototyping of non-imaging optics using PMMA like plastics [7]. They have also been used to create curved display surfaces, sensors, display devices, interactive devices [1-3], and to print 3D GRadient INdex (GRIN) devices by locally adjusting the index of refraction during the layer-by-layer fabrication [4]. While suitable for some applications, polymers are not typically used for high quality optics. Inorganic materials, particularly glasses, have better optical properties than polymers including higher transmission (especially at UV and IR wavelengths), lower coefficients of thermal expansion, and a stable index of refraction with respect to temperature [8]. The literature on applying AM techniques to glass is limited compared to polymers. Stereolithography was optimized for the deposition of quartz [9], borosilicate [10], and soda-lime glasses [11, 12], with a focus on dimensional accuracy. Three-dimensional printing was also studied using maltodextrin as a binder, which was subsequently burnt out in a kiln [13]. Extrusion techniques have been used to pattern colored glass [14], as well as to print bone scaffolds using bioglass [15]. While these studies demonstrate the ability of AM to form solid glass and ceramic parts, the parts produced in these studies were not transparent, even after post deposition firing. A recent report demonstrated the fabrication of transparent glass parts where the glass was allowed to flow under gravity from a kiln [16]. However, this is a very high temperature process and may be difficult to control. The objective of this work is to create a system for printing optically transparent glass.

The principal obstacle for the AM of transparent glass is achieving full densification [12]. Gas trapped during deposition is an issue for many additive processes, including welding. In structural applications, gas inclusions limit the strength of the printed parts; however, in transparent materials bubbles or voids scatter transmitted light. Even a small number of bubbles affect transparency when they exceed the wavelengths of the transmitted light [17-18]. Bubble formation is also a significant issue in conventional glass manufacturing. There are multiple potential sources of bubbles, including air trapped in the feed-stock, decomposition of batch material, and precipitation from the melt. A major source of bubbles is the reboil process, when gases are released from bubble-free melts due to high temperatures [19]. There are two main mechanisms to remove bubbles from glass in conventional glass manufacturing [20-22]. First, at high temperatures, bubbles in glass may combine with other existing bubbles until the buoyancy forces are sufficient to escape through the surface. Second, if low temperatures are held for a time period, bubbles have the potential to dissolve into the glass melt. Both of these mechanisms are time consuming, with holding times greater than 40 hours required to reach steady state in some conditions [23].

These factors make it very difficult to create optically transparent glass parts using powder bed AM methods. When the powder melts and fuses, air in the powder bed becomes trapped. In order to maintain its structural integrity, glass cannot remain heated long enough for the bubbles to coalesce and escape due to buoyancy without the geometry of the printed glass slumping and collapsing. Similar constraints limit the burnout/densification process for extrusion methods. An alternative is to start with fully dense glass, which minimizes the bubbles trapped during the fusion process. One way to achieve this is to use a wire or filament fed process. This is similar to the widely used polymer based Fused Deposition Modeling (FDM) process, which consists of the extrusion of a spool of thermoplastic through a nozzle. The softened material cools and hardens when it leaves the nozzle and intersects the build platform or previously deposited layers. The wire fed method has also received interest for the AM of metallic parts. The wire fed approach minimizes hazards associated with loose powder and can support higher deposition rates. It also provides lower contamination, material savings, and mechanical properties as good as those for cast products [24-26]. Various studies have optimized the metal wire fed approach, including determining the effects of the feed direction and angle [27-28], and demonstrated height and stability control [26, 29-30], as well as printing microscale parts [31]. Beyond the fabrication of freeform parts, metal wire fed processes have also been used for surface cladding and for repairing damaged structures [32-33].

This paper presents an experimental study of a filament-fed process for printing transparent glass. A laser was used to locally melt a glass filament fed into a melt pool. The substrate was heated throughout the process to provide stress relief and reduce thermal gradient. This paper identifies and explores the effects of the process parameters on the morphology and optical transparency of the resulting printed glass. The relevant process physics were determined and used to construct a first-order model of the melt pool temperature. These results were correlated with the experiments and used to understand/predict observed phenomena.

2. EXPERIMENTAL PROCEDURE

The properties of glass prevent the use of conventional techniques for AM employed for polymers or metals. The glass transition temperature of optical glasses makes it difficult to employ an extrusion nozzle. In addition, glass wets oxides, raising issues of nozzle clogging. Furthermore, electric arc generated plasmas used to melt metals are not able to be used, as glass is nonconductive.

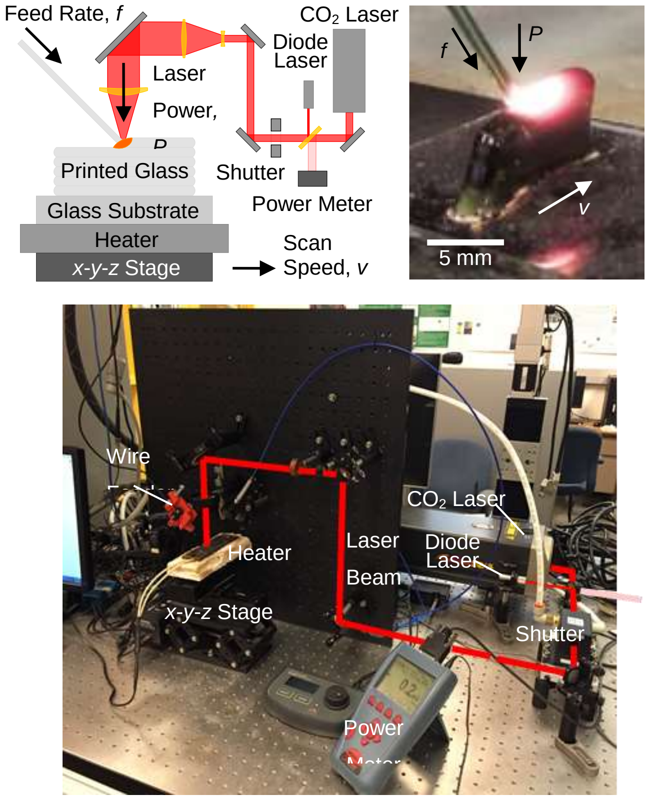

Figure 2.1 Illustration and photograph of filament-fed glass AM process.

Figure 2.1 shows a schematic and a photo of the experimental setup and additive manufacturing approach used in this paper. Microscope slides (1 mm thick) made of soda-lime glass are used as the substrate, and are clamped to a strip heater. This is positioned on a set of numerically controlled 3-axis stages. Direct-drive brushless servo motors are used for the x and y axes (Thorlabs DDMS100), while a scissor type lab jack (Thorlabs L490MZ) raises and lowers the build platform. While soda-lime glass is nearly transparent at visible and near-IR wavelengths, it is opaque with low reflection to long-wave infrared radiation [34]. A fixed CO_2 laser beam (Synrad Evolution 125, $\lambda_0 = 10.6$ μm) is focused onto the substrate and maintains a melt pool. The beam is defocused so that its diameter at the workpiece is 200 μm. The power of this beam is monitored during the experiment by reflecting 1% of the beam onto a thermopile type power meter (Ophir 10A-V1). To maximize power stability, the laser was set to a constant power (measured variation ±1.5%) and turned on and off with a shutter during processing.

Glass is significantly more prone to brittle fracture than polymers and metals. Thermally induced stresses during deposition and cooling can lead to the workpiece cracking. This issue can be minimized by the selection of a substrate with a similar Coefficient of Thermal Expansion (CTE) to that of the deposited material. Heating the substrate minimizes the thermal gradients in the workpiece during deposition. The substrate is maintained above the annealing point of soda-lime glass during the build process but below the temperature at which the glass slumps (flows under gravity). The temperature outside of the melt pool should be low enough to prevent the workpiece from slumping under gravity. Experimentally, it has been found that maintaining the substrate at 530°C allows the laser to locally increase the temperature of soda-lime glass without cracking or affecting the shape of the workpiece.

In this work, 1 mm diameter soda-lime glass filaments (glass stringers, Bullseye Glass) are used as the feedstock. The glass filaments are side fed at a 45° angle with the substrate using a custom-designed filament feeder (similar to those found in the literature on metal wire-fed AM [27-28]). The filament feeder is driven by a computer-controlled stepper motor, allowing the feed rate, f, to be varied. The glass filament is carefully aligned so that it passes through the intersection of the laser beam and workpiece. The laser energy maintains a melt pool and, as the workpiece is translated under the laser, material leaving the melt pool solidifies quickly. The viscosity of glass is much higher than that of molten metal, and the filament can be deflected by inadequately heating the melt pool. Feeding the filament into the melt as the substrate moves produces a track with uniform height and width. Three-dimensional structures are formed by repeating this process layer-by-layer, lowering the substrate between layers.

3. EXPERIMENTAL RESULTS

The morphology of the deposited material is dependent on three principal process parameters: laser power, feed rate, and scan speed. This study starts by examining how these process parameters affect the geometry of a single track. These results are then used to print thin, single track walls. The optical transmission is measured through the printed wall and compared to furnace cast glass with the same material composition.

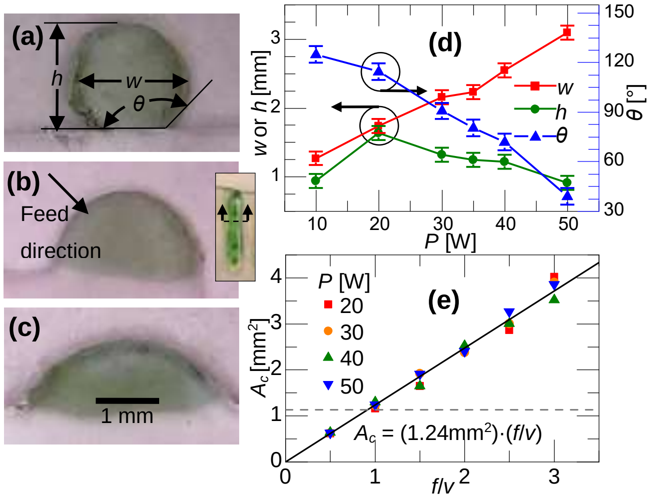

Figure 3.1 Single track cross-sectional geometries. Photographs of polished tracks deposited with (a) 20 W, (b) 35 W and (c) 50 W for f = 1 mm/s and v = 0.5 mm/s, (d) Track width, height and contact angle, (e) Cross-sectional area as a function of laser power

3.1. SINGLE TRACK FABRICATION

Six single tracks were fabricated with the same feed rate and scan speed, but with different laser powers. To distinguish the track shapes from the clear glass substrate, green colored glass filaments were used. Figure 3.1 shows the results for a constant feed rate of f = 1 mm/s and a constant scan speed of v = 0.5 mm/s, while the laser power was adjusted from P = 10 to 50 W. The tracks were cross-sectioned and polished to allow the width, w, height, h, and contact angle, θ, to be measured using a microscope.

The cross-section of the track fabricated using P = 10 W has a significantly smaller cross-sectional area than the tracks fabricated with the higher powers. In this case, the laser does not fully melt the filament and, since the feed rate exceeds the substrate scan speed, after a short distance the filament buckles and breaks. For higher laser powers, the cross-sectional area remains nearly constant. The contact angles and track widths of the fabricated tracks decrease with increasing laser power, while the contact angle is smaller than 90° for laser powers exceeding 35 W, indicating full melting and bonding with the substrate. Visible light is emitted for laser powers greater than 20 W with increasing brightness for increasing laser power. It is notable that there is a well demarcated boundary between the printed material and the substrate for all six power levels tested. That is, although there is some flow of the underlying transparent substrate, there does not appear to be substantial mixing between the two glasses.

3.2. GLASS WALL FABRICATION

To characterize the effects of the process parameters on the fabrication of multilayer parts, walls one track wide (15 mm long, 10 to 20 layers high) were built. After each layer was deposited, the substrate was lowered by 0.5 mm. Figure 3.2(a) shows the tool path of the printed walls in this experiment. This layer-to-layer height was kept constant for all of the experiments conducted in this paper. The values of the laser power, feed rate, and scan speed were constant for each wall. Four general results are observed: (A) flat top (the top surface is flat along the build direction) , (B) round top (the top surface is curved along the build direction), (C) irregular shape, and (D) failure. Photographs of the different types of builds are shown in Figure 3.2(b).

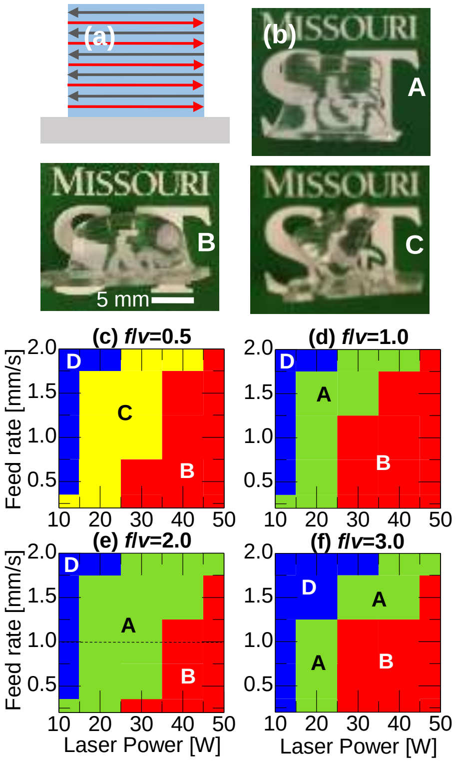

Figure 3.2 Morphology of single-track wide glass walls: (a) Tool path and build direction of single wall printing; (b) photographs of different wall types placed in front of university logo for better visualization; A: flat top, B: round top, and C: irregular shape. (c-f) process maps showing type of wall printed as a function of laser power and feed rate for different feed-rate to scan speed ratios

Figure 3.2 also charts the morphological outcomes for feed rate to scan speed ratios ranging from *f*/*v* =0.5 to 3.0. At each *f*/*v*, five laser powers ranging from 10 to 50 W, and four feed rates ranging from 0.5 to 2 mm/s were employed. The broadest range of parameters producing flat top glass walls was *f* = 2*v*, as shown in Figure 3.2(e). The wall geometry can be correlated to the single track results. In general, the parameters creating single tracks with the contact angles greater than 90° create a flat-top wall (compare Figure 3.2(e) to Figure 3.1(d)).

For the case of a failed build, there is insufficient energy input to melt the glass filament. In these cases the rigid filament is deflected by the rigid substrate and eventually breaks. The process was stopped during the build. Irregular shaped walls, an example of which was given in Figure 3.2(b), are formed when the feed rate was too high or the laser power was too low. In this case, the glass wire insufficiently bonded to the proceeding layer or the substrate. As the build progresses, the cumulative thermal energy provided by the laser increased the workpiece temperature and resulted in greater deposition. When the laser power was too high or the feed rate wasa too low, the absorbed energy exceeded the amount required to melt and fuseed the filament to the substrate (or preceding layers). The temperature of portions of the workpiece stayed above the glass working temperature for a long enough time for it to reflow/slump as seen in Figure 3.2(b). This was particularly significant at the edges of the wall where the stage decelerates before changing directions.

Correctly balancing the process parameters to produce flat-top walls is essential for future efforts to build more complex geometries. For example, when using process parameters P = 20 W, f = 2 mm/s, and v = 0.25mm/s, the desirable flat-top wall shown in Figure 3.2(a) was fabricated, while using process parameters P = 40 W, f = 0.5 mm/s, and v = 0.25 mm/s produced the round-top wall shown in Figure 3.2(b).

Wall thickness depends on the width of single track, which is a function of the laser power and feed rate. Figure 3.3(a) shows the cross-section of a flat top wall, showing obvious ripples between layers. Figure 3.3(b) shows a round top wall, where there is no gap between the layers and the cross-section edge is very smooth. In addition the thickness of single track walls can vary as a function of height, particularly for the flattop walls, shown in Figure 3.3(a), where individual layers are visible.

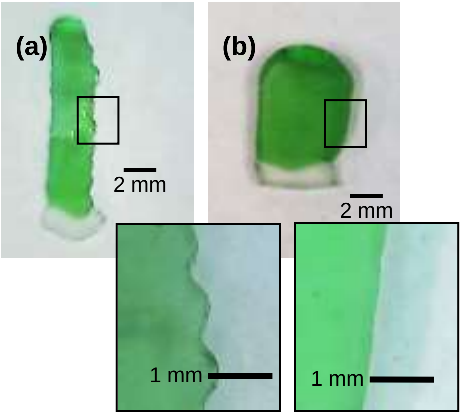

Figure 3.3 Micrographs of glass wall cross-sections (a) $f = 1$ mm/s, $v = 0.5$ mm/s, and $P = 20$ W and (b) $f = 1$ mm/s, $v = 0.5$ mm/s, and $P = 50$ W

3.3. OPTICAL RESULTS

The process parameters also have a dramatic effect on the transparency and refractive index of the printed glass. Deposited walls were polished on both sides prior to measuring transmission. Polishing standardized the thickness of the walls and removed the effects of morphology generated refraction.

To measure transparency, the transmission of a He-Ne laser ($\lambda_0 = 633$ nm) beam through the sample was measured at normal incidence. The incident beam was collimated with a diameter of 2 mm and collected from a solid angle of 0.66 Sr. The power of incident and transmitted beam were both measured using a Newport Model 1935-C power meter.

The extinction coefficient for each polished glass wall was calculated using the Beer-Lambert law

$$\alpha = \frac{1}{L}\ln\left[(1-R)^2/\tau\right] \tag{1}$$

where τ is the measured transmittance of the laser beam, R is the reflectivity of one interface, and L is the sample thickness. The reflectivity was calculated from the refractive index, n, and is $R = [(1-n)/(1+n)]^2$ at normal incidence [35]. The reflectance is measured to be in the range 0.036 to 0.041.

Figure 3.4 shows the dependence of the extinction coefficients on the laser power for five different feed rates. In each experiment the scan speed is half of the feed rate. Figure 3.4 shows that there is an optimum laser power to achieve the minimum extinction coefficient for laser powers ranging from 20-50 W and feed rates ranging from 0.2-2 mm/s.

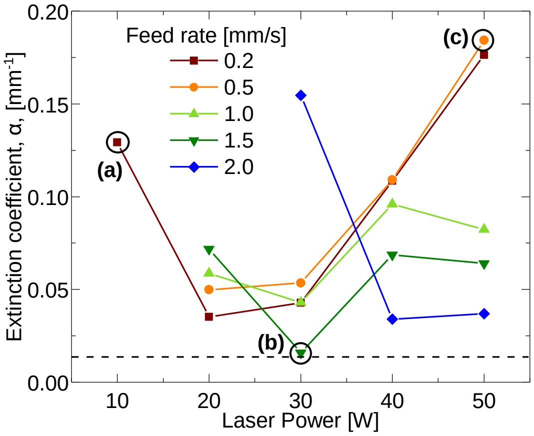

Figure 3.4 Measured extinction coefficient of glass walls as a function of processing parameters. (a), (b) and (c) are samples shown in Figure 3.5.

To compare the AM process to conventional casting, a baseline part was cast from the same soda-lime glass stock. Glass filaments were broken into small pieces and placed into a small alumina crucible, which was heated to 1100°C in a muffle furnace for 5 hr and then cooled gradually at a rate of 2°C/min to relieve thermal stresses. The cast glass piece was polished prior to measuring its transmission using the same procedure applied to the printed glass. This produced an extinction coefficient of 0.015 mm^{-1} at 633 nm (dashed line in Figure 3.4). It should be noted that the glass used in these experiments is marketed for art projects and is not precision optical quality glass. The lowest measured extinction coefficient of all laser melted glass pieces is 0.0143 mm^{-1}, equivalent to 85.8% transmission through a piece 5 mm thick, including reflectance at the front/back surfaces. This illustrates that the transmittance of laser printed glass can be as high as the furnace cast pieces. To evaluate process variability, four glass walls were made with identical process parameters (f = 0.5 mm/s, v = 0.25 mm/s, P = 20 W) and polished. The transmission through each sample was measured to calculate the extinction coefficient, and ranged from 0.071-0.082 mm^{-1}.

Figure 3.5 shows photographs of a pattern imaged through the samples marked (a), (b), and (c) in Figure 3.4. The first column shows the samples in contact with a printed image. The sample produced with low power, Figure 3.5(a), shows a target contrast similar to the cast sample. However, multiple voids and fractures can be observed in the sample produced with high power (Figure 3.5(c)). Next, photographs were taken of the target with the samples separated from the target by a 30 mm gap. These results are shown in the second column of Figure 3.5. Light originating from a point on the object plane passes through the entire sample before being focused by the camera lens onto the image plane. The contrast for the cast glass and the best printed sample (medium power) are similar, however, the sample printed using low power is significantly blurred despite the lack of noticeable defects. This is attributable to the optical index inhomogeneity in the sample. No image can be observed through the sample in (c) due to significant scattering in the sample. These results are reinforced by dark-field images, which were produced by side illuminating the samples and imaging light scattered by defects into the camera. Discrete small bubbles in all of the samples including the furnace cast specimen and several larger bubbles trapped in the best sample (b) can be observed. Further, both discrete bubbles and foam can be observed in sample (c) in addition to cracks.

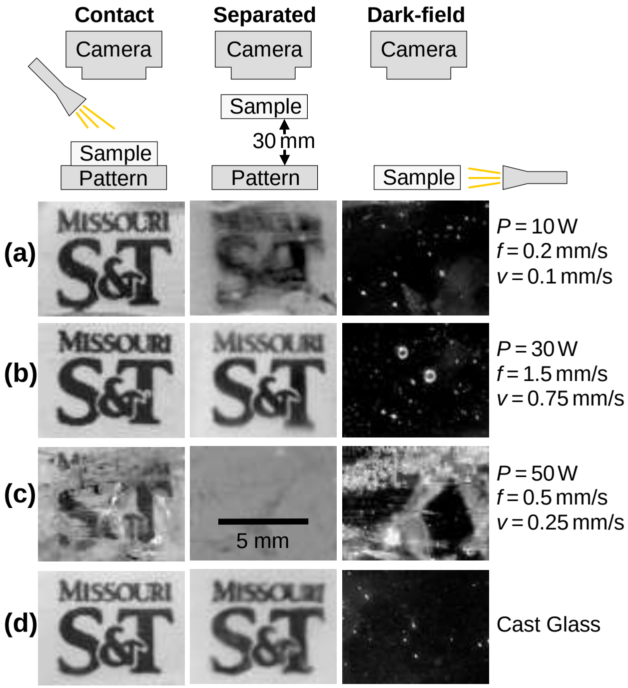

Figure 3.5 Photographs of samples under different conditions; in contact with background (left column), separated from the background (middle column), and dark-field (right column). (a) low-power sample, (b) medium power sample, (c) high-power sample and (d) furnace cast sample

The refractive indices of samples (b), (c) and (d) in Figure 3.5 were measured using a J.A. Woollam M-VASE Variable Angle Spectroscopic Ellipsometer. Each sample was measured at three different points and a Cauchy model was fit to the data (including scattering losses for the sample in (d) in Figure 3.5). Figure 3.6 shows the refractive indices of these samples in the 400-1000 nm wavelength range. The experimental measurement of the indices of refraction shows that the process parameters used to create sample (b) produce a piece that has higher index homogeneity. The other samples, on the other hand, have lower homogeneity. This implies that the process parameters used to create the pieces have a strong influence on the homogeneity of their index of refraction.

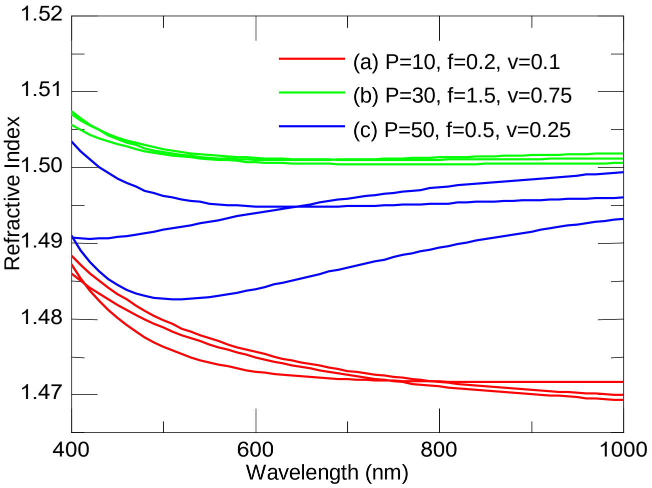

Figure 3.6 Refractive indices in 400-1000 nm wavelength range of (a) low-power sample, (b) medium power sample, and (c) high-power sample

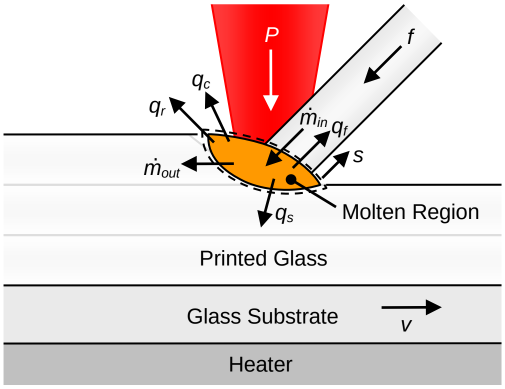

Figure 3.7 Mass and energy balance surrounding molten region

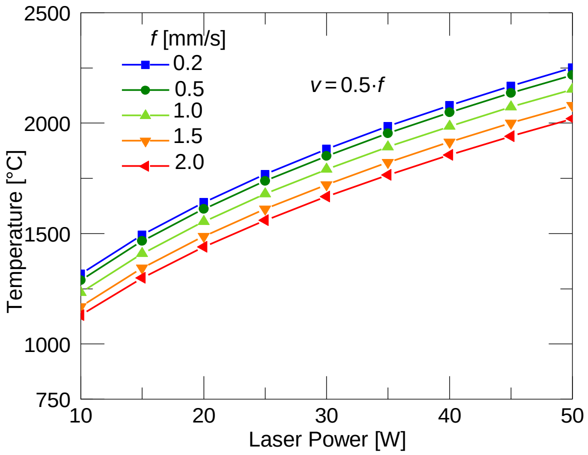

Figure 3.8 Estimated molten region temperature using energy balance model for $f = 2v$

4. DISCUSSION

The molten region temperature is critical to both the morphology and the transparency of the fabricated glass parts. The effects of the process parameters can be understood from a first-order model of the deposition process. For this analysis, the continuous deposition of a single track, as shown in Figure 3.7, is considered. This neglects the effects of acceleration and deceleration at the edges and simplifies the problem to the constant mass and energy balances on a control volume around molten region.

4.1. MASS BALANCE DISCUSSION

Glass enters the melt pool with the filament and exits with the deposited track. The density of glass is not strongly dependent on temperature and the mass balance can be expressed as

$$\dot{m}_{in} = \frac{\pi}{4} D_f^2 \cdot f = \dot{m}_{out} = A_c \cdot v \tag{2}$$

where D_f is the filament diameter and A_c is the cross-sectional area of the printed track. This model explains the results seen in Figure 3.1(e) where the cross-sectional area is independent of laser power and scales linearly with the ratio of the feed rate f to the scan speed: A_c=(1.24 mm^2)·f/v. This also agrees with the average measured diameter of the filaments, D_f=1.25 mm, suggesting it is possible to locally draw the glass to a track width significantly less than the filament diameter because the heated glass will support a tensile load. While the cross-sectional area does not depend on the deposition temperature, the shape of the printed track (i.e., width, height, and contact angle shown in Figure 3.1(d)) is strongly dependent on the surface tension and viscosity of the glass, both of which vary significantly with temperature [36-37]. For this analysis, it is assumed that the molten region is a hemisphere with the same diameter as the filament, i.e., $D_m = D_f$.

4.2. ENERGY BALANCE DISCUSSION

At steady state the change in energy around the molten region is zero and is expressed as

$$\Delta E = \alpha P - \left(\dot{m}\Delta h + Q_s + Q_f + Q_c + Q_r\right) = 0 \tag{3}$$

where P is the laser power, α is the absorptivity of glass at 10.6 μm wavelength, Δh is the specific enthalpy increase of the glass from inlet to outlet, Q_s is the heat lost to the substrate, Q_f is the heat transferred to the filament, and Q_r and Q_c represent the heat exchanged with the surroundings via radiation and convection, respectively. The absorptivity α is 94%, since glass is fully opaque at 10.6 μm wavelength, and there is only 6% loss due to the surface reflection [38]. The heat transfer from the melt pool to the glass wall is a complex process with temperature dependent thermal properties. The following assumptions are made to significantly simplify the heat transfer analysis: 1) the temperature is uniform in the molten region; 2) the shape of the molten region is hemispherical and constant; and 3) the convection coefficient is 10 $W/m^2 \cdot K$, and is temperature independent.

As the temperature of glass entering and exiting the molten region is the same, there is no enthalpy change between the inlet and outlet of the molten region. The heat transfer from the melt pool to the air includes convection (Q_c) and radiation (Q_r). For a hemispherical molten region of diameter, D_m, heat transfer due to conduction and radiation, respectively, are

$$Q_c = h_c \left(\frac{\pi}{4} D_m^2 \right) \left(T_m - T_\infty \right) \tag{4}$$

$$Q_r = \varepsilon\sigma \left(\frac{\pi}{4} D_m^2 \right) \left(T_m^4 - T_\infty^4 \right) \tag{5}$$

where h_c is the heat convection coefficient, T_∞ is the ambient temperature, which is assumed to be the same as the surroundings, ε is the emissivity of glass, which is a function of temperature, and σ is Stefan-Boltzmann constant

Because soda-lime glass is semitransparent over infrared wavelengths, the radiation heat transfer in glass should be considered. For example, when soda-lime glass is heated from ambient to 1100°C and 1500°C, the glass emits 90% of its radiation energy between 1 and 6.9 µm and between 1 and 5.4 µm, respectively [39]. An effective heat conductivity that includes both conduction and radiation can be used to calculate the total heat flux. The effective heat conductivity used in this calculation is obtained from Pilon et al. [40]

$$k_{eff} = \begin{cases} \left(0.021\ \mathrm{W/m}\right)T - 14.6\ \mathrm{W/m\cdot K} & T \geq 750\ ^{\mathrm{o}}\mathrm{C} \\ 2\ \mathrm{W/m\cdot K} & T < 750\ ^{\mathrm{o}}\mathrm{C} \end{cases} \tag{6}$$

The total heat flux from the melt pool to the glass wall is

$$q_s = k_{eff} S \left(T_m - T_s \right) \tag{7}$$

where T_m is the average temperature of melt pool and T_s is the temperature of the glass wall far from the melt pool [41]. In this case, S is the shape factor for this heat conduction process, which is obtained from a finite-element simulation of the conduction away from the molten region. In the simulation, a laser beam was scanned along the center of a rectangular wall. The simulation is allowed to progress until the temperature distribution is invariant with respect to distance. The linearization of the temperature dependence of the thermal conductivity leads to a nearly linear relationship between power and the melt temperature. These simulation results predict that the shape factor is nearly a linear function of the scan speed (v) for a wall with constant width and height. Moreover, this linear function is dependent on the wall height and width. When the wall height is 10 mm and wall width is 1.25 mm, the shape factors is

$$S = 0.3432v + 1 \tag{8}$$

The filament diameter is relatively small relative to its length and, thus, heat conduction along the filament is assumed to be solely along the length direction. A second order ordinary differential equation is obtained by truncating the Taylor expansion of q_f as

$$-\frac{d}{ds}\left(k_{eff}\frac{dT_f}{ds}\right)\left(\frac{\pi D^2}{4}\right)-h_c\pi D\left(T_f-T_\infty\right)-\varepsilon\sigma\pi D\left(T_f{}^4-T_\infty^4\right)-\rho A_c fc_p\frac{dT_f}{ds}=0 \tag{9}$$

where s is the position along the filament, D is the filament diameter, T_f is the temperature of the filament at a distance s from the laser, and ρ is the glass density. Assuming that the filament is infinitely long (justified due to the low thermal conductivity of the glass), the boundary conditions are: $T|_{s=0} = T_m$ at the end touching in the molten region, and $T|_{s=\infty} = T_\infty$ at the other end. When T_m is known, the temperature distribution inside the filament is obtained by solving (9) numerically and Q_f is calculated from the temperature gradient (i.e., $Q_f = kA_c dT/ds|_{s=0}$). The heat lost to the filament, Q_f, is a function of both the melt pool temperature and the feed rate. It is solved by evaluating Eq. (9) using a finite difference method.

The molten region temperature is estimated by solving Eq. (3). This is plotted as a function of the laser power in Figure 3.8 for $f = 2v$. The fraction of the laser power lost to the environment varies significantly with process parameters, ranging from 55% to 84% for the data in Figure 3.8. At higher feed rates, the molten region temperature is lower. This makes the process more efficient due to lower losses to the substrate and filament. Even with the substrate preheated to 530°C, conduction heat transfer to the substrate ranges from 43% to 62%, which increases with laser power and decreases with feed rate. The heat transfer lost directly to convection proves to be negligible. Radiation directly emitted from the molten region becomes significant when the temperature rises, however, this effect is mitigated by lower effective emissivity of the glass at shorter wavelengths.

4.3. MORPHOLOGY DISCUSSION

When the laser power is 10 W, the scan speed is 0.5 mm/s, and the feed rate is 1 mm/s (corresponding to the conditions in Figure 3.1d), the model estimates the temperature of the molten region to be 1233°C, which is 56° higher than the commonly accepted working temperature of soda-lime glass (1177°C) [39]. As a result, the viscosity of the molten region is in the order of 1000 Pa·s [39], which is stiff enough to deflect and break the filament, resulting in a failed build and confirming observed results. When the laser power is between 20 W and 30 W the temperature is estimated to be 1554°C to 1791°C, respectively. Under these conditions the filament is fully melted, and the process is continuous with the mass and energy balances in dynamic equilibrium. This is consistent with the results in Figure 3.1, which showed that these conditions produce a contact angle greater than 90°. There is insufficient energy to melt the previous layer fully, so the new deposited track essentially lies on the previous layer. Figure 3.1 showed that the width of the melted track increases linearly with the laser power as the laser power increases from 30 to 50 W. Both the viscosity and the surface tension decrease with temperature [36], allowing the molten glass to spread laterally and leading to contact angles less than 90°. This produces round top walls with the smooth sidewalls shown in Figure 3.3(b). Fumes can be observed when the laser power is above 35 W, indicating vaporization and possible chemical reactivity [42].

4.4. OPTICAL RESULTS DISCUSSION

Figure 3.5 demonstrated that there is an optimal set of process parameters having the lowest extinction coefficient (highest transmission). According to the optical results and energy balance analysis, when the temperature is too low or too high, the extinction coefficient will become much higher and the refractive index will become much more inhomogeneous. There are two different causes for the higher extinction coefficient and index inhomogeneity. At lower laser power, numerous striaes are formed. Striaes are streaks formed in glass with refractive indices different from that of the surrounding glass [43]. The temperature of the molten region of the sample in Figure 3.5(a) is estimated to be 1289°C, 112° higher than the working temperature of soda-lime glass. The laser energy is not sufficient to remelt the previous layer, leading to an inhomogeneity of the stress field between the layers. On the other hand, when the power is higher, the glass reboil is intensified and is accompanied by fumes. The heating duration is only a few seconds and many of the bubbles formed by reboil do not have time to escape from the free surface. In Figure 3.5(c), the entire background is blocked by the bubbles. The molten region temperature for this piece is estimated to be 2217°C. When the temperature of the molten region is in an optimal range, glass can be melted with very few bubbles and striaes. In Figure 3.5(b), the background is as clear as the cast glass in Figure 3.5(d) with similar bubble density. The molten region temperature is estimated to be 1721°C. The experimental results show that the filament fed process can produce highly transparent glass pieces with smooth surfaces using these process parameters.

Figure 4.1 Convex shape made using filament-fed glass AM process

To further demonstrate this process, a simple convex geometry was printed (r = 5 mm) on a glass slide and is shown in Figure 4.1. This sample was made by three layers of circular paths (four, two, and one concentric circles for the first, second, and third layer, respectively, with radii from 3.5mm to 1.5 mm). P = 30 W, f = 1 mm/s, and v = 0.5 mm/s. These parameters were selected to allow longer heating and facilitate more reflow into voids between the printed tracks. The part was printed continuously with the stage being lowered 0.5mm after the completion of each layer. The backside of the substrate which was in contact with the heater was polished to remove contamination, but the top surface is smooth as printed (no subsequent polishing). The top surface assumes a convex shape due to the printed topography and localized reflow caused by laser heating during the printing of subsequent layers (analogous to flame polishing).

5. SUMMARY AND CONCLUSIONS

This paper demonstrates the fabrication of transparent glass parts using a filament fed additive manufacturing process. The effects of the process parameters on the morphology and transparency of printed glass were empirically explored. By studying single track melting and single wall printing, it was found that the molten region temperature determines the contact angle, establishing the morphology of the glass wall. This effect can be correlated to the molten region temperature calculated from the thermal modeling. The transmission of laser melted glass pieces and a furnace melted glass piece were also measured. The extinction coefficient of the printed glass was measured and shown to approach that of cast glass. Optical defects and refractive index inhomogeneity can also be linked to the molten region temperature illustrating that insufficient heating produces striaes, and excessive heating in the molten region generates bubbles. The optical quality of the best printed part is as good as furnace cast glass part using the same type of filaments. While the glass used in these experiments was not intended for optics, the results can be extended to engineered technical glasses that have better optical qualities. The experiments in this report show the potential of additive manufacturing for printing optics and photonics.

ACKNOWLEDGMENT

We are grateful to Dr. Glenn Boreman at the University of North Carolina at Charlotte, to Dr. Clara Rivero-Baleine at Lockheed Martin, and to Drs. Augustine Urbas and Jonathan Goldstein at the Air-Force Research Laboratory for the helpful discussions.

FUNDING

This work was supported by the Missouri S&T Materials Research and Intelligent Systems Centers, as well as grants from the Department of Education (P200A120062), and National Science Foundation (CMMI-1301414), (EEC-1004839).

REFERENCES

[1] Pereira, T., Rusinkiewicz, S., and Matusik, W., 2014, "Computational light routing: 3D printed optical fibers for sensing and display," ACM Transactions on Graphics (TOG), 33(3), p. 24.

[2] Willis, K., Brockmeyer, E., Hudson, S., and Poupyrev, I., 2012, "Printed optics: 3d printing of embedded optical elements for interactive devices," Proceedings of the 25th annual ACM symposium on User interface software and technology, ACM, Cambridge, MA, Oct. 7-10, pp. 589-598.

[3] Brockmeyer, E., Poupyrev, I., and Hudson, S., 2013, "PAPILLON: designing curved display surfaces with printed optics," Proceedings of the 26th annual ACM symposium on User interface software and technology, ACM, St. Andrews, Scotland, United Kingdom, Oct. 8-11, pp. 457-462.

[4] Urness, A. C., Moore, E. D., Kamysiak, K. K., Cole, M. C., and McLeod, R. R., 2013, "Liquid deposition photolithography for submicrometer resolution three-dimensional index structuring with large throughput," Light: Science and Applications, 2(3), p. e56.

[5] Niino, T., and Yamada, H., 2009, "Fabrication of transparent parts by laser sintering process:-transparentization of laser sintered plastic parts by infiltrating thermosetting epoxy with tuned refractive index," Journal of the Japan Society for Precision Engineering, 75(12), pp. 1454-1458.

[6] Marder, S. R., Brédas, J.-L., and Perry, J. W., 2007, "Materials for multiphoton 3D microfabrication," MRS Bulletin, 32(07), pp. 561-565.

[7] Blessing, K., 2014, "Print head, upgrade kit for a conventional inkjet printer, inkjet printer and method for printing optical structures," U.S. Patent No. 8,840,235. (23 September 2014).

[8] Weber, M. J., 2002, Handbook of Optical Materials, CRC press, Boca Raton, FL.

[9] Khmyrov, R., Grigoriev, S., Okunkova, A., and Gusarov, A., 2014, "On the possibility of selective laser melting of quartz glass," Physics Procedia, 56, pp. 345-356.

[10] Klocke, F., McClung, A., and Ader, C., 2004, “Direct laser sintering of borosilicate glass,” Solid Freeform Fabrication Symposium Proceedings, Austin, TX, Aug. 3–5, pp. 214–219.

[11] Fateri, M., and Gebhardt, A., 2015, "Selective laser melting of soda-lime glass powder," International Journal of Applied Ceramic Technology, 12(1), pp. 53-61.

[12] Luo, J., Pan, H., and Kinzel, E. C., 2014, "Additive manufacturing of glass," Journal of Manufacturing Science and Engineering, 136(6), pp. 061024-1-6. doi:10.1115/1.4028531.

[13] Marchelli, G., Prabhakar, R., Storti, D., and Ganter, M., 2011, "The guide to glass 3D printing: developments, methods, diagnostics and results," Rapid Prototyping Journal, 17(3), pp. 187-194.

14] Klein, S., Simske, S., Adams, G., Parraman, C., Walters, P., Huson, D., and Hoskins, S., 2012, "3D printing of pransparent glass," Proceedings NIP and Digital Fabrication Conference, Society for Imaging Science and Technology, Quebec City, Canada, Sep. 9-13, pp. 336-337.

[15] Fu, Q., Rahaman, M. N., Dogan, F., and Bal, B. S., 2008, "Freeze casting of porous hydroxyapatite scaffolds. I. Processing and general microstructure," Journal of Biomedical Materials Research Part B: Applied Biomaterials, 86(1), pp. 125-135.

[16] Klein, J., Stern, M., Franchin, G., Kayser, M., Inamura, C., Dave, S., Weaver, J.C., Houk, P., Colombo, P., Yang, M., and Oxman, N., “Additive manufacturing of optically transparent glass,” 3D Printing and Additive Manufacturing (online).

[17] Pilon, L., and Viskanta, R., 2003, "Radiation characteristics of glass containing gas bubbles," Journal of the American Ceramic Society, 86(8), pp. 1313-1320.

[18] Baillis, D., Pilon, L., Randrianalisoa, H., Gomez, R., and Viskanta, R., 2004, "Measurements of radiation characteristics of fused quartz containing bubbles," Journal of the Optical Society of America A: Optics and Image Science, and Vision, 21(1), pp. 149-159.

[19] Shelby, J. E., 2005, Introduction to glass science and technology, Royal Society of Chemistry, London, UK.

[20] Beerkens, R., 1995, "The role of gases in glass melting processes," Glass Science and Technology, 68(12), pp. 369-380.

[21] Weinberg, M. C., Onorato, P. I., and Uhlmann, D. R., 1980, "Behavior of bubbles in glassmelts: I, Dissolution of a stationary bubble containing a single gas," Journal of the American Ceramic Society, 63(3-4), pp. 175-180.

[22] Balkanli, B., and Ungan, A., 1996, "Numerical simulation of bubble behaviour in glass melting tanks. Part II. Dissoved gas concentration," Glass Technology, 37(3), pp. 101-105.

[23] Pilon, L., Fedorov, A. G., Ramkrishna, D., and Viskanta, R., 2004, "Bubble transport in three-dimensional laminar gravity-driven flow – mathematical formulation," Journal of Non-Crystalline Solids, 336(2), pp. 71-83.

[24] Mok, S. H., Bi, G., Folkes, J., Pashby, I., and Segal, J., 2008, "Deposition of Ti–6Al–4V using a high power diode laser and wire, Part II: Investigation on the mechanical properties," Surface and Coatings Technology, 202(19), pp. 4613-4619.

[25] Martina, F., Mehnen, J., Williams, S. W., Colegrove, P., and Wang, F., 2012, "Investigation of the benefits of plasma deposition for the additive layer manufacture of Ti–6Al–4V," Journal of Materials Processing Technology, 212(6), pp. 1377-1386.

[26] Heralić, A., Christiansson, A.-K., and Lennartson, B., 2012, "Height control of laser metal-wire deposition based on iterative learning control and 3D scanning," Optics and Lasers in Engineering, 50(9), pp. 1230-1241.

[27] Syed, W. U. H., and Li, L., 2005, "Effects of wire feeding direction and location in multiple layer diode laser direct metal deposition," Applied Surface Science, 248(1-4), pp. 518-524.

[28] Mok, S. H., Bi, G., Folkes, J., and Pashby, I., 2008, "Deposition of Ti–6Al–4V using a high power diode laser and wire, Part I: Investigation on the process characteristics," Surface and Coatings Technology, 202(16), pp. 3933-3939.

[29] Heralić, A., Christiansson, A.-K., Ottosson, M., and Lennartson, B., 2010, "Increased stability in laser metal wire deposition through feedback from optical measurements," Optics and Lasers in Engineering, 48(4), pp. 478-485.

[30] Xiong, J., and Zhang, G., 2014, "Adaptive control of deposited height in GMAW-based layer additive manufacturing," Journal of Materials Processing Technology, 214(4), pp. 962-968.

[31] Katou, M., Oh, J., Miyamoto, Y., Matsuura, K., and Kudoh, M., 2007, "Freeform fabrication of titanium metal and intermetallic alloys by three-dimensional micro welding," Materials and Design, 28(7), pp. 2093-2098.

[32] Nowotny, S., Scharek, S., Beyer, E., and Richter, K.-H., 2007, "Laser beam build-up welding: precision in repair, surface cladding, and direct 3D metal deposition," Journal of Thermal Spray Technology, 16(3), pp. 344-348.

[33] Clark, D., Bache, M. R., and Whittaker, M. T., 2008, "Shaped metal deposition of a nickel alloy for aero engine applications," Journal of Materials Processing Technology, 203(1-3), pp. 439-448.

[34] Rubin, M., 1985, "Optical properties of soda lime silica glasses," Solar Energy Materials, 12(4), pp. 275-288.

[35] Born, M., and Wolf, E., 1999, Principles of Optics, Cambridge University Press, Cambridge, UK.

[36] Parikh, N., 1958, "Effect of atmosphere on surface tension of glass," Journal of the American Ceramic Society, 41(1), pp. 18-22.

[37] Pilon, L., Guochang, Z., and Viskanta, R., 2002, "Three-dimensional flow and thermal structure in glass melting furnaces. Part II. Effects of batch blanket and bubbles," Glass Science and Technology, 75(3), pp. 115-124.

[38] Pascal, D., Ciprian-Florin, M., Florin, B., and Jean-Francois, C., 2012, "Glass Marking with CO 2 Laser: Experimental Study of the Interaction Laser-Material," Journal of Surface Engineered Materials and Advanced Technology, 2012.

[39] Zeller, R., and Pohl, R., 1971, "Thermal conductivity and specific heat of noncrystalline solids," Physical Review B, 4(6), p. 2029.

[40] Pilon, L., Janos, F., and Kitamura, R., 2014, "Effective thermal conductivity of soda-lime silicate glassmelts with different iron contents between 1100 °C and 1500 °C," Journal of the American Ceramic Society, 97(2), pp. 442-450.

[41] Holman, J., 2009, Heat Transfer, McGraw-Hill, New York.

[42] Kucuk, A., Clare, A. G., and Jones, L. E., 2000, "Differences between surface and bulk properties of glass melts I. Compositional differences and influence of volatilization on composition and other physical properties," Journal of Non-Crystalline Solids, 261(1–3), pp. 28-38.

[43] Stroud, J. S., 2003, "Striae quality grades for optical glass," Optical Engineering, 42(6), pp. 1618-1624.

III. ADDITIVE MANUFACTURING OF GLASS FOR OPTICAL APPLICATIONS

Junjie Luo[a], Luke J. Gilbert[a], Douglas A. Bristow[a], Robert G. Landers[a], Jonathan T. Goldstein[b], Augustine M. Urbas[b], Edward C. Kinzel[a]

[a]Department of Mechanical and Aerospace Engineering
Missouri University of Science and Technology, Rolla, Missouri 65409, U.S.A
[b]Air Force Research Laboratory, Materials and Manufacturing Directorate, Wright-Patterson Air-Force Base, OH, USA 45433

ABSTRACT

Glasses including fused quartz have significant scientific and engineering applications including optics, communications, electronics, and hermetic seals. This paper investigates a filament fed process for Additive Manufacturing (AM) of fused quartz. Additive manufacturing has several potential benefits including increased design freedom, faster prototyping, and lower processing costs for small production volumes. However, current research in AM of glasses is limited and has focused on non-optical applications. Fused quartz is studied here because of its desirability for high-quality optics due to its high transmissivity and thermal stability. Fused quartz also has a higher working temperature than soda lime glass which poses a challenge for AM. In this work, fused quartz filaments are fed into a CO_2 laser generated melt pool, smoothly depositing material onto the workpiece. Single tracks are printed to explore the effects that different process parameters have on the morphology of printed fused quartz. A spectrometer is used to measure the thermal radiation incandescently emitted from the melt pool. Thin-walls are printed to study the effects of layer-to-layer height. Finally, a 3D fused quartz cube is printed using the newly acquired layer height and polished on each surface, and cylindrical-convex shapes with smooth surface are printed to show the capability of the filament fed process for optics printing. The transmittance and index homogeneity of the polished cube are both measured. These results show that the filament fed process has the potential to print fused quartz with optical transparency and index of refraction uniformity approaching bulk processed glass.

Keywords: Fused quartz, additive manufacturing, optically transparent

1. INTRODUCTION

Additive Manufacturing (AM) has demonstrated significant promise for printing complex and unique 3D parts quickly and cheaply. AM has been used for creating structural parts since the late 1980's [1]. Recently, the need for manufacturing transparent and structurally complex parts has led to several initial studies of the AM of transparent materials. These studies include the 3D printing of polymer [2-4], ink-jet printing [5,6], Selective Laser Sintering (SLS) of polymers infiltrated with indexed matched plastic in post processing [7], and multiphoton stereolithography [8]. These processes are capable of printing low-power polymer optics, however, they lack the ability to be implemented with glasses and other inorganic materials required for higher-quality optics.

Compared to polymers, glasses have higher transmissivity (particularly in the ultraviolet and infrared), lower coefficients of thermal expansion, and more temperature stable index of refraction [9]. These attributes are even better for fused quartz. Conventional AM techniques such as Selective Laser Melting/Sintering (SLM/SLS), extrusion techniques and inkjet processes have been demonstrated for printing glasses and ceramics [10-19]. These studies have focused on dimensional accuracy and the resultant parts were not transparent. The lack of transparency is largely due to gas inclusions. For optical applications, even a small amount of porosity is sufficient to scatter light and make the part non-transparent. This can be overcome by extruding fully dense material. For example, transparent soda-lime glass was printed using the filament fed process [13, 21-23]. Similarly, Klein et al. [24] deposited 3D structures by allowing molten soda-lime glass to flow through computer controlled orifice. While soda-lime glass has a relatively low working temperature, fused quartz's working temperature (~2300°C) exacerbates the material challenges faced in the AM of soda-lime glass [9].

This paper presents a study of a laser heated, filament fed process for printing fused quartz. The influence of different parameters on the morphology of printed single tracks is explored. The optimum parameters are than used to print thin walls and cylinders to study the effect of layer height. The best layer height is then used to print a fully dense cube.

Incandescent thermal radiation emitted by the molten glass during printing is observed spectroscopically and correlated with a basic thermal model for the process. Finally, the optical quality of the 3D cube is demonstrated by measuring the transmittance and Modulation Transfer Function (MTF).

2. EXPERIMENTAL PROCEDURE

Figure 2.1 shows the experimental additive manufacturing setup. A CW CO_2 laser (Synrad Evolution 125, λ_0=10.6 µm) is focused on the intersection of the filament and the substrate. The CO_2 laser couples to a phonon mode in the fused quartz [25]. A 1 mm thick fused quartz slide is used as the substrate and is fixed to a numerically controlled 3-axis stage. The *x* and *y* stages (Thorlabs DDMS100) are driven by direct-drive brushless servo motors while a pantograph type lab-jack (Thorlabs L490MZ) is used to raise and lower the platform.

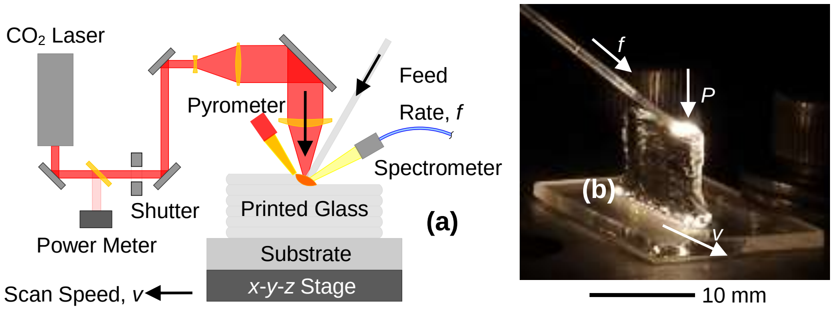

Figure 2.1 Illustration and photograph of filament-fed fused quartz AM process

Previous work using soda-lime glass required preheating the substrate.[13] This proved not to be necessary for small pieces made of fused quartz because the coefficient of thermal expansion is less than 1% of soda lime glass [9]. For larger pieces, heating of the substrate may be necessary due to a larger thermal stresses. The filaments used in this work were GE 214 fused quartz rods with a nominal 0.5 mm diameter. The Full Width Half Maximum (FWHM) diameter of the laser beam at this intersection was measured to be 300 µm. A beam splitter is used to reflect 1% of the laser beam into a thermopile power meter (Ophir 10A –V1). By scaling this measured value, the power of laser energy delivered to the melt pool was obtained. For each experiment, the laser power was set at a constant level (producing a measured power variation of ±1.5%.) An OceanOptics USB-4000 fiber-coupled spectrometer (calibrated with an OceanOptics LS-1-CA 2800 K light source) was used with a 5 cm focal length lens to collect visible/NIR radiation emitted from the 1.5 mm diameter interrogation region centered on the laser-heated region. The temperature in melt pool was also monitored using a Lumasense Impac 140 pyrometer, which measures the temperature by analyzing the radiation signal at 5.14 µm.

For the following experiments, single tracks with a uniform height and width are created by a continuous feeding and laser melting of the filament. 3D structures (thin walls and cubes) were then printed by repeating this process by lowering and offsetting the platform by set amounts varying between 0.126 and 0.294 mm.

3. RESULTS AND DISCUSSION

3.1. SINGLE TRACK RESULTS

The properties of a printed part depend strongly on the properties of each single track. To characterize the effects of the process parameters on the morphology of deposition, single tracks were printed with different parameters. Four general classes of result were observed: (A) under melted, (B) continuous track, C) discontinuous track, and (D) strong vaporized. Figure 3.1 charts the morphological outcomes for feed rate to scan speed ratios f/v =1, 2 and 3, along with representative photographs of each class of result.

An under melted track occurs when the absorbed energy is insufficient to fully melt the filament. The unmelted filament is deflected by the rigid substrate and eventually breaks. In order to produce continuous deposition, the laser must supply sufficient energy to fully melt the filament. As the specific laser energy increases beyond this point, the fused quartz balls up at the end of the filament due to surface tension. The filament only makes contact with the substrate intermittently as it is advanced toward the intersection of the substrate and laser beam. In this state, vaporization of the filament also starts to be apparent. For even higher laser power, the rate of vaporization increases to the point that the rate of deposition of fused quartz onto the substrate is negative and material is removed to create a groove in the substrate.

Figure 3.2 plots the cross-sectional area, A_c, of tracks printed with f/v=2. The dashed line shows the cross-sectional area obtained from conservation of mass between the fed filament and the printed track. The negative values of A_c correspond to vaporization of the substrate. The figure shows that vaporized mass increases with increasing laser power, and decreases with increasing feed rate (scan speed).

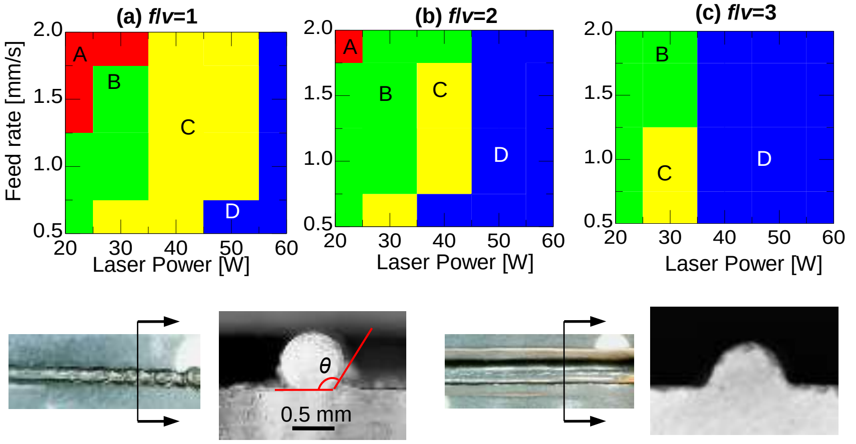

(d) Under melted

(e) Continuous

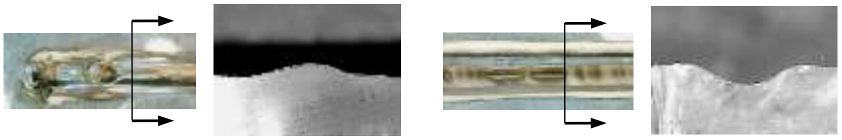

(f) Discontinuous

(g) Strong vaporized

Figure 3.1 (a)-(c) Morphology result of the quartz single track printing, (d)-(g) the top and cross-sectional views of the four types of morphology

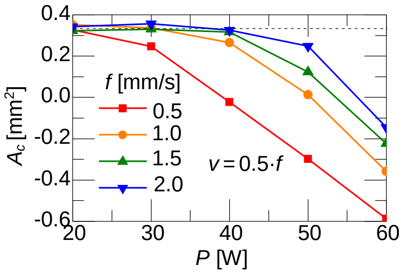

Figure 3.2 Cross-section areas of all tracks made with *f*/*v*=2

3.2. THIN WALL RESULTS

Thin walls were printed by lowering the substrate by a predefined height after each layer was printed. In these experiments, the substrate was scanned back and forth so that glass was continuously deposited. Correct selection of the layer height proved to be critical to successful wall deposition. If the layer height did not match the other parameters the wall would fail to be built due to a misalignment of the work piece, tip of the filament, and the laser beam.

Based on the results of the single track experiments the parameter set f=1 mm/s, v=0.5 mm/s, P=30 W were selected for printing thin wall. These parameters produced a track with a height of h_0=0.21 mm. Walls were printed with constant layer heights ranging from 0.13 to 0.29 mm (0.6h_0 to 1.4h_0). Figure 3.3 shows representative results. Continuous walls were deposited when the layer height is 0.17-0.21 mm (0.8 h_0 to 1.0 h_0)

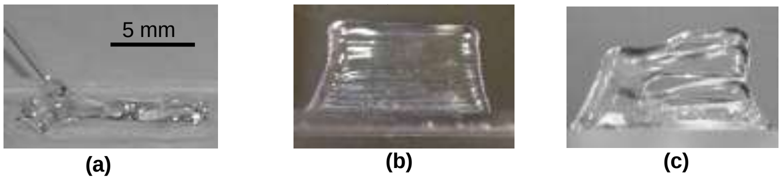

Figure 3.3 Three types of single wall printing result: (a) too low layer height (b) appropriate layer height (c) too high layer height

When the layer height was too low, the intersection of the laser beam and filament tip was beneath the top of the previous layer. The filament tip was deflected from the center of the melt pool and was no longer able to be fully melted. As shown in Figure 3.3(a), the filament then pushed the printed wall with a sufficient force to distort the previously deposited layer and the filament was broke off at the feeder. When the layer height matches the other process parameters, the filament could be fed into the melt pool at each layer appropriately so that the printed wall was continuous. An example of the continuous wall is shown in Figure 3.3(b). If the layer height was higher than the appropriate range, molten glass would ball up at the tip of the filament. The diameter of the ball increased during the feeding process, and the ball touched the previous layer intermittently as it gained mass through the feeder, then subsequently lost mass by contacting the substrate. This produced a 2D discontinuous wall as shown in Figure 3.3(c).

Figure 3.4 shows a thin-walled cylinder (diameter 6 mm, height 5 mm). This result also illustrates that the deposition was also dependent on the scanning direction relative to the feeding direction. In particular, when the stage was scanned in the opposite direction as the filament feed direction, the filament was deflected so that the beam shifts to directly irradiate to the filament before it intersects the substrate. In this case the deposited track was slightly wider and less high than when the feed direction is parallel or perpendicular to the scan direction.

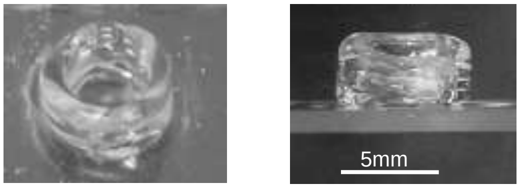

(a)

Figure 3.4 Photos of the printed fused quartz cylinder: (a) oblique view (b) side view

3.3. CUBE PRINTING RESULTS

The single wall printing process is only the deposition of one layer in vertical direction. However, the printing of 3D parts requires the deposition in horizontal direction. For 3D part printing, new problems appear. Glass has a different refractive index than air, so any voids inside the 3D part will scatter light inside glass. The requirement for transparent glass printing is more challenging than other materials printing, which often are only concerned about the mechanical properties and morphology. To further explore the potential for printed fused quartz, a 6×6×6 mm cube was printed with the same parameters (f=1 mm/s, v=0.5 mm/s, P=30 W). The cube was built up with a series of monolayers, and each monolayer is printed with a pattern of single tracks. The space between tracks is set to be 0.4 mm on each layer. Figure 3.5a-b shows the cube as printed. The undulations from individual layers are visible, however, the top layer is very smooth. After printing, the cube is ground flat and two opposing surfaces are polished with 1 μm fabric plate for optical testing. Figure 3.5c shows the photographs of the cube after polishing. Patterns directly behind the quartz on a 1951 USAF resolution chart be seen clearly without obvious distortion. It is worth noting that there are no voids inside the sample. This is because the depositing track is melted together with previous tracks, and the interface between two tracks are transferred to a smooth surface due to surface tension.

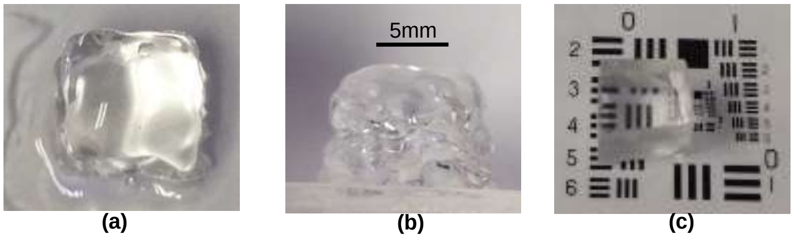

(a) **(b)** **(c)**

Figure 3.5 Two issues that limit the morphology of printed cubes (a) top view (b) side view (c) after polishing

3.4. CURVATURE SURFACE PRINTING RESULTS

By overlapping monolayers with different widths, curvature profiles can be printed. However, the smoothness of the printed surface is limited by the size of filament. This unsmooth surface can be smoothened by a CO_2 laser scanning after printing, which is which is driven by surface tension in the laser molten region. Figure 3.6(a) shows a printed sample before and after laser reflowing

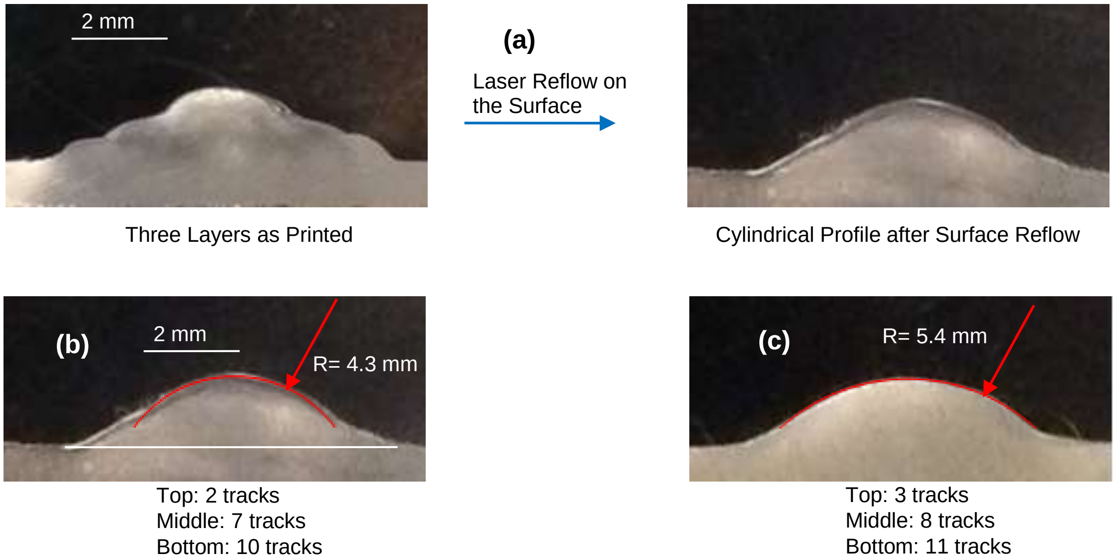

Figure 3.6 The printed cylindrical-convex geometries (a) a printed sample before and after laser reflowing; (b) and (c) the cross-section view of two printed cylindrical surfaces

Two sections of cylindrical surfaces were printed with 0.5 mm/s scan speed and 1 mm/s feed rate and 30 W laser power, and reflowed on the surface with 25 W laser power and 0.3 mm/s scan speed are shown in Fig. 3.6(b) and (c). Both samples consist of three monolayers, the details of each layer are depicted in Fig. 3.6(b) and (c). The radii of the both samples are close to the design value at the top of surfaces, but they deviate from the design value near the interface with substrates because the edges were flattened with the substrate during the laser reflowing process.

Due to the surface features of the printed cylindrical-convex samples, they may function as cylindrical lenses at the top of the profile. In order to determine the focusing capability of the printed samples, a fiber laser beam (λ= 1.06 μm) focused by the samples was measured using a Ophir NanoScanV2 beam profiler. Fig. 3.7(a) shows the profile of incident laser beam, which is in Gaussian distribution. The laser beam profiles that were focused by the two samples are shown in Fig. 3.7(b) and (c). It is obvious that a larger surface radius leads to a larger focused beam width and a longer focal distance, which agrees with optics theory. This result proves the assumption that the printed cylindrical-convex geometries can function as cylindrical lenses.

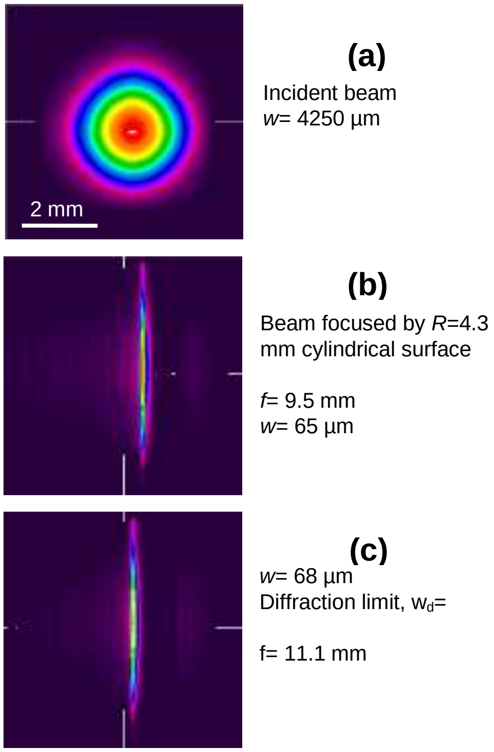

Figure 3.7 (a) Profile of the incident laser beam (b) profile of the focused beam through the R= 4.3 mm sample (c) profile of the focused beam through the R= 5.4 mm sample

3.5. MELT POOL RADIATION SPECTRA MEASUREMENTS

As shown in Figure 2.1b, the laser heats the fused quartz to the point that emits visible light. The intensity of the emitted light varies with the laser power and other processing parameters. The emitted light is potentially a useful measurement for feedback control because it relates to the temperature of the molten region. Figure 3.8 shows spectral data collected using a spectrometer when depositing single tracks using f=2 and v=1 with laser power ranging from 20 W to 60 W. All the data was collected while the laser beam was near the center of the deposition track, after process was invariant with respect to scan distance. The results in Figure 3.8(a) were recorded with an integration time 100 ms. At this integration time, the emission from the 20 to 35 W experiments are too low to resolve. These experiments were repeated with a larger integration time in Figure 3.8(b).

Planck's law cannot be used to directly calculate the average temperature of the interrogation region because the interrogation region is not at a uniform temperature. In addition the molten quartz does not appear to exhibit a gray body spectral response. However, the results clearly show that both the peak wavelength and intensity correlate with laser power. In particular, the maximum wavelength shows a blue shift from laser powers between 20 and 40W (Fig. 3.8b), but above 40 W, the wavelength distribution is constant and only increases in intensity. This transition appears to correspond to the onset of significant vaporization from the molten region.

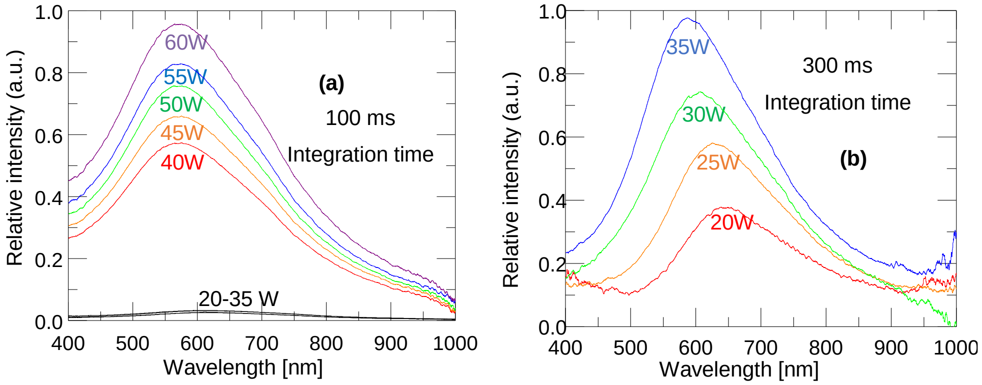

Figure 3.8 Radiation spectra of fused quartz melt pools in different track morphologies: (a) laser power range 40-60 W (b) laser power range 20-35 W

3.6. MASS AND ENERGY BALANCE ANALYSIS

Figure 3.9 shows a simple model of the AM process. The fused quartz filament enters the melt pool and exits as a printed track. A mass balance can be expressed as:

$$\dot{m}_{in} - \dot{m}_{out} = \dot{m}_v \,, \tag{1a}$$

where $$\dot{m}_{in} = \rho f \left(\pi D_f^2/4\right) \text{ and } \dot{m}_{out} = \rho A_c v \,, \tag{1b}$$

In these expressions, $\dot{m}_v$ is the mass of vaporized fused quartz, ρ is the density of the fused quartz, D_f is the diameter of the filament, f is the feed rate of filament, v is the scan speed of the state, and A_c is the cross-sectional area of the printed track. Solving for the cross-sectional area gives

$$A_c = \frac{\pi}{4}\frac{fD_f^2}{v} - \frac{\dot{m}_v}{\rho v} \tag{2}$$

The measured cross sectional area was plotted for different powers in Fig. 3.2. Equation 2 allows calculation of the vaporized mass. The amount of vaporized material scales with the power and is significantly greater for lower feed rates, as shown in Fig. 3.2.

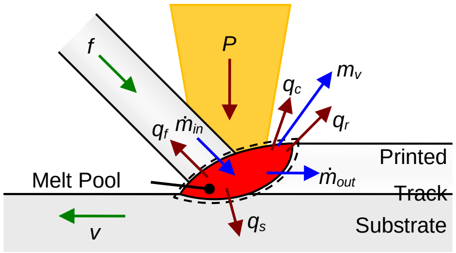

Figure 3.9 Mass and energy balance surrounding melt pool

The energy balance is significantly simplified by modeling the problem as quasi-steady state. This assumes that the temperature of the molten region is invariant with the scanning position and is reasonable in the center of a long track or thin wall. Under these conditions, the change in the thermal energy over a control volume surrounding the molten region is zero:

$$\Delta \mathrm{E} = P - \left(Q_c + Q_r + Q_f + \dot{m}_v h_v + Q_s \right) = 0 \tag{3}$$

where P is the laser power, h_v is energy required for the vaporizing a unit mass of glass (specific latent heat), Q_s is the heat conducted to the substrate, Q_f is the heat transfer to the filament, Q_r is the net heat transfer exchanged with surroundings via radiation, and Q_c represents the heat lost to the air by convection.

Even at quasi-steady state, the heat transfer from the molten region is a complex process with temperature dependent thermal properties. The following assumptions are made to significantly simplify the heat transfer analysis: 1) temperature in the melt pool is uniform; 2) the shape of the melt does not change with time; 3) the convection coefficient is taken to be 10 W/m^2·K, and is temperature independent; and 4) the filament acts as a 1D extended surface subject to convection and radiation.

For a hemispherical molten region, the heat lost to the surrounding via convection and radiation are

$$Q_c = h\left(\frac{\pi}{4} D_m^2\right)\left(T_m - T_\infty\right) \tag{4}$$

and

$$Q_r = \varepsilon\sigma\left(\frac{\pi}{4} D_m^2\right)\left(T_m^4 - T_\infty^4\right) \tag{5}$$

where D_m is the diameter of the melt pool, h is the heat convection coefficient, T_∞ is the ambient temperature , ε is the emittance of glass, and σ is Stefan-Boltzmann constant.

While not as significant as in metal wire-fed AM processes, some thermal energy is lost to conduction along the filament, q_f. Because the filament is slender, it can be modeled as a 1D conduction problem with the temperature only varying along the length (feeding direction). This temperature distribution can be derived from applying energy conservation inside the filament. Combining axial conduction, radiation and convection, along with advection gives:

$$-\frac{d}{ds}\left(k\frac{dT_f}{ds}\right)\left(\frac{\pi D_f^2}{4}\right)-h\pi D_f\left(T_f-T_\infty\right)-\varepsilon\sigma\pi D_f\left(T_f^4-T_\infty^4\right)-f\rho A_c c_p\frac{dT_f}{ds}=0 \tag{6}$$

where T_f is the temperature of the filament at distance *s* from the molten region. The boundary conditions for Eq. 6 are that the temperature of the filament where it contacts the molten region is T_m ($T_f|_{s=0}=T_m$) and the filament is long enough that its temperature approaches ambient far away from the molten region ($T_f|_{s=\infty}=T_\infty$). T_f along the filament is obtained by solving (6) with the finite difference method. The heat transfer to the filament, q_f, can than be calculated from Fourier's law

$$Q_f=-kA_c\left.\frac{dT}{ds}\right|_{s=0} \tag{7}$$

SiO_2 gas is not thermodynamically stable at atmospheric pressure and all of the vaporized quartz is converted to SiO by the chemical reaction: $2SiO_2 \Leftrightarrow 2SiO+O_2$ [26] Yang et al. reported that the evaporation of quartz starts to be significant at 2800 K, and is constant with respect to temperature after above the boiling point (~3100 K).[27] Elhadj et al. reported that the vaporization rate of fused quartz follows:[28]

$$V_m''=\left(6.25\times10^3\frac{\mu\mathrm{g}}{\mu\mathrm{m}^2\cdot\mathrm{s}}\right)\exp\left[\left(-120.1\frac{\mathrm{kcal}}{\mathrm{mol}}\right)\Big/\left(RT\right)\right] \tag{8}$$

where *R* is the ideal gas constant. This mass flux was applied over the area of the molten region $\dot{m}_v=\left(\pi D_m^2/4\right)V_m''$.

The heat conduction from the molten region to the substrate (Q_s) was calculated using the finite volume method in ANSYS FLUENT. Again, the scanning path was assumed to be infinitely long to avoid edge effects. This required scanning the laser to the point that the peak temperature was invariant with respect to the scanned distance (typically 40-60 mm for *v*=0.25-1.0 mm/s). Simulations were run for a full range of laser powers and translation velocities to generate a semi-empirical relationship between the temperature of the molten region and power supplied by the laser. These results were combined with Eqs. 3-7 to solve for the temperature of the molten region. This is plotted in Fig. 3.9 for a constant feed rate/scan speed ratio, *f*/*v*=2. The figure shows that the temperature of melt pool increases with laser power until it reaches the vaporization region. The onset of vaporization significantly reduces the rise in temperature with laser power. As the temperature approaches the boiling point, the energy removed from the system via latent heat dominates the thermal response.

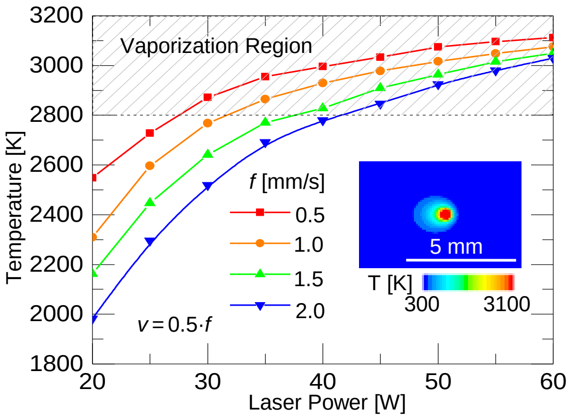

Figure 3.10 Melt pool temperature calculated from the energy balance analysis with inset showing surface temperature from FLUENT model

The calculated temperature in this model is consistent with the mass balance result. Specifically, Figures 3.2 and 3.10 show that the mass loss occurs when the temperature of the molten region is sufficient for vaporization. The higher temperatures associated with lower feed rates also correspond to lower cross section areas. When the feed rate is *f*=2.0, the temperature enters the vaporization region for powers greater than 40 W. This agrees well with the significant rise in thermal emission intensity observed in the spectroscopic study, including the observation that the peak emission wavelength does not continue to shift with increased power for powers greater than 40 W.

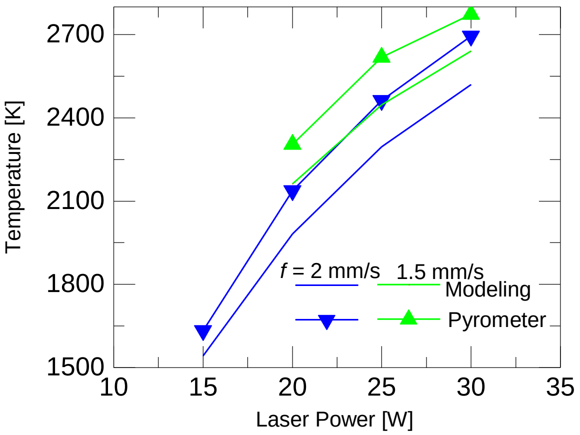

Figure 3.11 Melt pool temperature from thermal modeling and pyrometer measuring with f = 2 mm/s and v = 1 mm/s at various laser powers

In order to validate the thermal modeling results, a Lumasense Impac 140 pyrometer was used to measure the melt pool temperature at lower laser powers, since the maximum value of the temperature range is 2500 °C. Figure 3.11 shows the temperatures from the pyrometer and from the modeling result. The temperatures calculated form this model were about 5% lower than the measured value. It is also worth noting that, while the laser power is increasing from low to high, vaporization occurs at temperatures above 2700 K. This result also agrees with the study of Elhadj et al. [28] that strong vaporization occurs at temperatures above 2800 K.

3.7. OPTICAL MEASUREMENTS

The transmittance of the sample was measured using a 5 mW HeNe laser (632.8 nm) at normal incidence using an integrating sphere. For the 6 mm thick sample printed with f=1 mm/s, v=0.5 mm/s, P=30 W, the transmittance was measured to be 0.924. Spectroscopic ellipsometery (M-VASE, J.A. Woollam) was used to measure the index of refraction for the printed fused quartz. At λ=633 nm, the index is n=1.468 corresponding to a reflectance at normal incidence of R=0.036. After accounting for reflectance at the front and back surfaces, this predicts at normal incidence transmittance of 0.929. This measurement indicates that less than 0.005 of the energy is absorbed or scattered by the printed quartz, or a uniform extinction coefficient of α=13.2 m^{-1}. We attribute the larger extinction coefficient to scattering in the printed quartz from small inclusions due to the condensation of vaporized silica soot in the specimen.

Another potentially important factor for printed optics is the refractive index homogeneity. Even small index variances inside of a sample will significantly degrade the spatial resolution of an optical system. Figure 3.12 shows an image of a 1951 USAF test pattern taken through the quartz sample taken with ambient lighting. The printed quartz window is positioned ~10mm above the object so that a light from points in the object space pass through the entire sample before being focused onto the image plate. Qualitatively this image is similar to an image taken with the same system without the printed quartz window (Figure 3.12c). One way to quantify this is to measure the Modulation Transfer Function (MTF).The parameter M is defined as[29]

$$M = \frac{I_{\max} - I_{\min}}{I_{\max} + I_{\min}} \tag{9}$$

where I_{max} is the maximum intensity and I_{min} is the minimum intensity of fringes on the recorded image. Both images, with and without the sample, were processed in MATLAB in gray scale. Figure 3.12d compares the MTF for the system with the printed quartz window to the system without the window. The MTF of both images starts to drop at 57 mm^{-1} and are very similar. This suggests that the quartz cube's index of refraction is homogenous.

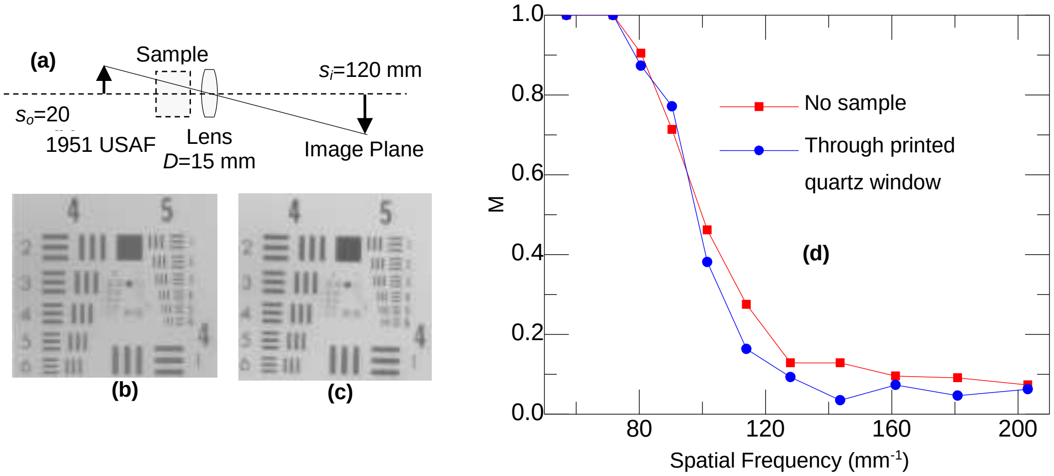

Figure 3.12(a) Imaging setup (b) the image taken through 6 mm of printed quartz (c) image without sample in the path (d) the MTF results for these two images

4. SUMMARY AND CONCLUSIONS

This paper demonstrated additive manufacturing of GE 214 fused quartz using a filament fed process. Continuous single tracks, single walls, a cylinder and a cube are all successfully printed. Also, cylindrical-convex shapes with smooth surface are printed, and these printed shapes can function as cylindrical lenses by focusing a He-Ne laser beam. There is a strong effect of vaporization on the morphology of printed single tracks at higher laser powers and lower feed rates. Spectroscopy shows significantly greater incandescent emission associated with the onset of vaporization. Analysis of mass and energy balances is used to predict the thermal response. This substantiates the evaporation and agrees with the empirically established operational process window. The modeling result is also validated by the pyrometer measurement at temperatures under 2500 °C. Optical measurements show that the printed fused quartz cube has high transmittance and index homogeneity. The coefficient of thermal expansion of fused quartz proves to be advantageous for additive manufacturing which can be used to create complex geometries for both optical and structural applications. Future work will be focus on the 3D parts printing and precision control of the process.

ACKNOWLEDGEMENTS

This work was supported by the Missouri S&T Materials Research Center, Lockheed-Martin, and the National Science Foundation (CMMI-1538464)

REFERENCES

[1] Gibson, I., Rosen, D. W., and Stucker, B., 2010, Additive manufacturing technologies, Springer.

[2] Brockmeyer, E., Poupyrev, I., and Hudson, S., 2013, "PAPILLON: designing curved display surfaces with printed optics," Proceedings of the 26th annual ACM symposium on User interface software and technology, ACM, St. Andrews, Scotland, United Kingdom, pp. 457-462.

[3] Willis, K., Brockmeyer, E., Hudson, S., and Poupyrev, I., "Printed optics: 3d printing of embedded optical elements for interactive devices," Proc. Proceedings of the 25th annual ACM symposium on User interface software and technology, ACM, pp. 589-598.

[4] Pereira, T., Rusinkiewicz, S., and Matusik, W., 2014, "Computational Light Routing: 3D Printed Optical Fibers for Sensing and Display," ACM Trans. Graph., 33(3), pp. 1-13.

[5] Blessing, K., and Richard Van, d. V., 2014, "Print head, upgrade kit for a conventional inkjet printer, inkjet printer and method for printing optical structures," Luxexcel Holding Bv., United States.

[6] Urness, A. C., Moore, E. D., Kamysiak, K. K., Cole, M. C., and McLeod, R. R., 2013, "Liquid deposition photolithography for submicrometer resolution three-dimensional index structuring with large throughput," Light Sci Appl, 2, p. e56.

[7] Niino, T., and Yamada, H., 2009, "Fabrication of transparent parts by laser sintering process:-transparentization of laser sintered plastic parts by infiltrating thermosetting epoxy with tuned refractive index," Journal of the Japan Society for Precision Engineering, 75(12), pp. 1454-1458.

[8] Marder, S. R., Brédas, J.-L., and Perry, J. W., 2007, "Materials for multiphoton 3D microfabrication," MRS Bulletin, 32(07), pp. 561-565.

[9] Weber, M. J., 2002, Handbook of optical materials, CRC Press, FL, USA.

[10] Khmyrov, R., Grigoriev, S., Okunkova, A., and Gusarov, A., 2014, "On the possibility of selective laser melting of quartz glass," Physics Procedia, 56, pp. 345-356.

[11] Khmyrov, R. S., Protasov, C. E., Grigoriev, S. N., and Gusarov, A. V., 2015, "Crack-free selective laser melting of silica glass: single beads and monolayers on the substrate of the same material," The International Journal of Advanced Manufacturing Technology, pp. 1-9.

[12] Klocke, F., McClung, A., and Ader, C., 2004, "Direct laser sintering of borosilicate glass," The Proceedings of the 15th Annual SFF Symposium, University of Texas, Austin, TX, USA, pp. 214-219.

[13] Luo, J., Pan, H., and Kinzel, E. C., 2014, "Additive manufacturing of glass," Journal of Manufacturing Science and Engineering, 136(6), pp. 061024.061021-061026.

[14] Fateri, M., and Gebhardt, A., 2014, "Selective Laser Melting of Soda-Lime Glass Powder," International Journal of Applied Ceramic Technology.

[15] Fu, Q., Rahaman, M. N., Dogan, F., and Bal, B. S., 2008, "Freeze casting of porous hydroxyapatite scaffolds. I. Processing and general microstructure," Journal of Biomedical Materials Research Part B: Applied Biomaterials, 86(1), pp. 125-135.

[16] Klein, S., Simske, S., Adams, G., Parraman, C., Walters, P., Huson, D., and Hoskins, S., "3D Printing of Transparent Glass," Proc. NIP & Digital Fabrication Conference, Society for Imaging Science and Technology, pp. 336-337.

[17] McMillen, D., Li, W., Leu, M. C., Hilmas, G. E., and Watts, J., 2016, "Designed extrudate for additive manufacturing of zirconium diboride by ceramic on-demand extrusion," Proceedings of the 26th Annual International Solid Freeform Fabrication Symposium University of Texas, Austin, TX.

[18] Ghazanfari, A., Li, W., and Leu, M. C., 2015, "Adaptive rastering algorithm for freeform extrusion fabrication processes," Virtual and Physical Prototyping, 10(3), pp. 163-172.

[19] Li, W., Ghazanfari, A., McMillen, D., Leu, M. C., Hilmas, G. E., and Watts, J. L., "Properties of partially stabilized zirconia components fabricated by the ceramic on-demand extrusion process," Proc. Annual International Solid Freeform Fabrication Symposium, pp. 916-928.

[20] Marchelli, G., Prabhakar, R., Storti, D., and Ganter, M., 2011, "The guide to glass 3D printing: developments, methods, diagnostics and results," Rapid Prototyping Journal, 17(3), pp. 187-194.

[21] Luo, J., Gilbert, L., Qu, C., Wilson, J., Bristow, D., Landers, R., and Kinzel, E., 2015, "Wire-Fed additive manufacturing of transparent glass parts," ASME 2015 International Manufacturing Science and Engineering Conference, ASME, Charlotte, NC, USA, pp. V001T002A108-1-8.

[22] Luo, J., Gilbert, L. J., Qu, C., Landers, R. G., Bristow, D. A., and Kinzel, E. C., 2017, "Additive manufacturing of transparent soda-lime glass using a filament-fed process," Journal of Manufacturing Science and Engineering, 139(6), pp. 061006-1-8.

[23] Luo, J., Gilbert, L. J., Peters, D. C., Bristow, D. A., Landers, R. G., Goldstein, J. T., Urbas, A. M., and Kinzel, E. C., 2016, "Bubble formation in additive manufacturing of glass," SPIE Defense+ Security, International Society for Optics and Photonics, pp. 98220D-1-6.

[24] Klein, J., Stern, M., Franchin, G., Kayser, M., Inamura, C., Dave, S., Weaver, J. C., Houk, P., Colombo, P., and Yang, M., 2015, "Additive Manufacturing of Optically Transparent Glass," 3D Printing and Additive Manufacturing.

[25] Kitamura, R., Pilon, L., and Jonasz, M., 2007, "Optical constants of silica glass from extreme ultraviolet to far infrared at near room temperature," Applied optics, 46(33), pp. 8118-8133.

[26] Chang, D. B., Drummond, J. E., and Hall, R. B., 1970, "High-power laser radiation interaction with quartz," Journal of Applied Physics, 41(12), pp. 4851-4855.

[27] Yang, S. T., Matthews, M. J., Elhadj, S., Draggoo, V. G., and Bisson, S. E., 2009, "Thermal transport in CO_2 laser irradiated fused silica: in situ measurements and analysis," J. Appl. Phys, 106(10), p. 103106.

[28] Elhadj, S., Qiu, S. R., Monterrosa, A. M., and Stolz, C. J., 2012, "Heating dynamics of CO_2-laser irradiated silica particles with evaporative shrinking: Measurements and modeling," Journal of Applied Physics, 111(9), p. 093113.

[29] Boreman, G. D., 2001, Modulation transfer function in optical and electro-optical systems, SPIE Press Bellingham, WA, USA.

IV. BUBBLE FORMATION IN ADDITIVE MANUFACTURING OF GLASS

Junjie Luo[a], Luke J. Gilbert[a], Daniel C. Peters[a], Douglas A. Bristow[a], Robert G. Landers[a], Jonathan T. Goldstein[b], Augustine M. Urbas[b], Edward C. Kinzel[a]

[a]Department of Mechanical and Aerospace Engineering
Missouri University of Science and Technology, Rolla, Missouri 65409, U.S.A
[b]Air Force Research Laboratory, Materials and Manufacturing Directorate,
Wright-Patterson Air-Force Base, OH, USA 45433

ABSTRACT

Bubble formation is a common problem in glass manufacturing. The spatial density of bubbles in a piece of glass is a key limiting factor to the optical quality of the glass. Bubble formation is also a common problem in additive manufacturing, leading to anisotropic material properties. In glass Additive Manufacturing (AM) two separate types of bubbles have been observed: a foam layer caused by the reboil of the glass melt and a periodic pattern of bubbles which appears to be unique to glass AM. This paper presents a series of studies to relate the periodicity of bubble formation to part scan speed, laser power, and material feed rate. It was found that the cause of the periodic bubbles was gas being trapped as the glass filaments melted onto the substrate. These bubbles can be eliminated by scanning over the deposited glass a second time with the laser, which allows the glass to soften and the bubbles to escape.

Keywords: periodic, bubbles, additive manufacturing, glass

1. INTRODUCTION

The avoidance of bubbles in glass is an important aspect of glass manufacturing, especially for the fabrication of optical glasses. In glass small gas bubbles can cause light to be scattered leading to poor image transmission [1]. In fact, in industry, six bubbles per ton of glass results in a 10% rejection rate for CRT television screens [2]. The bubbles that occur in glass come from a variety of sources: trapped air, decomposition of the individual components that make up glass, and galvanic oxidation reduction reactions. Bubbles can also appear when super saturated glasses are reheated and begin to precipitate. This phenomenon is known as “reboil” [3]. The composition of the gasses depends on the methods with which the bubbles are formed, but are usually composed of N_2, O_2, CO_2, SO_2, and H_2O [4]. Due to the tight tolerances used of the glass industry, a great deal of work has been conducted in the literature to predict and limit the amount of bubbles that are formed in the initial melting and subsequent reheating processes [2,5-15].

In a previous study of glass additive manufacturing, it was found that bubbles formed in the printed glass is also a key factor that limits its optical quality [16]. The foam layer described in the glass literature has been observed in glass AM at high temperatures for soda-lime glass. More interesting, however, is the generation of uniform periodic bubbles in the laser melting process which does not appear to occur in conventional glass processing.

The problem of periodic bubbles does not only occur in glass filament fed AM processes. A similar phenomenon of periodic bubbles was observed in the study of 3D printing of glass done by HP Lab [17]. Chen et al. [18] studied the bubble formation in Fused Deposition Modeling (FDM) process by Nano-CT characterization. Two types of bubbles were found: internal bubbles and necking bubbles. The necking bubbles usually distribute as a series in a line, which is very similar to the periodic bubbles formed in glass AM processes.

2. EXPERIMENTAL SETUP

The experimental approach for the glass printing process is illustrated in Figure 2.1. A glass filament was continuously fed into a laser generated melt pool. The intersection of the filament, laser beam and substrate defined the build plane. Phonon modes in glass allowed the absorption of LWIR radiation and led to the selection of a CW CO_2 laser (Synrad Evolution 125, λ_0 = 10.6 μm) to locally heat the glass. A strip heater maintained the substrate temperature at 550°C during printing. A heated substrate was necessary to avoid thermally shocking the workpiece during deposition.

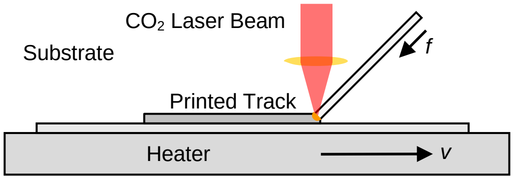

Figure 2.1 Glass printing experimental setup

The laser was slightly defocused to give a Full Width Half Maximum (FWHM) diameter of 300 μm at the build plane. The heater was positioned by *x* and *y* stages (Thorlabs DDMS100) using direct-drive brushless servo motors. The *z* stage, a pantograph type lab-jack (Thorlabs L490MZ), raised and lowered the workpiece into and out of the build plane. The experiments in this paper used one mm thick soda-lime microscope slide substrates and one mm diameter (nominal) clear soda-lime glass stringers (Bullseye Glass Co.) for the filaments.

Two different experiments were conducted. The first experiment maps the periodicity of the bubbles to the process parameters of the filament fed process. The second experiment removed the filament feeding and maps the periodicity of the bubbles to the process parameters of the laser scanning process.

In both experiments, the same phenomenon of bubble formation was observed.

3. RESULTS

In the first experiment, the glass filament was continuously advanced toward the substrate by a home-built filament feeder. Only a single track was printed to simplify the process. To print a complicated part, the process would be repeated to build the geometry layer-by-layer. Three different results were found: (a) no bubbles or only sporadic bubbles, (b) periodic bubble patterns along the deposition, and (c) foam layers. Dark field images of the three results are shown in Figure 3.1.

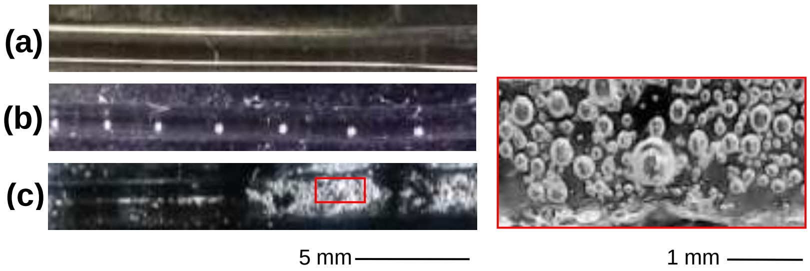

Figure 3.1 Dark field images of the three results (a) no bubbles (sporadic), (b) periodic bubble pattern, and (c) foam layers

Figure 3.2 shows the bubble periodicity with respect to laser power and scan speed for a constant feed rate of *f*=1 mm/s. Tracks that have no bubbles, or bubbles that occur sporadically without visible periodicity, are assigned infinite bubble spacing. Tracks where a foam layer is generated are assigned a bubble spacing of zero. In the latter case the bubbles are not periodic and the distance between the bubbles is negligible. The distances between bubbles are measured manually using a microscope by averaging the separation between eight consecutive spaces. For each parameter set, four 30 mm long tracks were printed. At each scan speed, the distance between bubbles decreases with laser power. When the laser power is very low, only sporadic bubbles or no bubbles formed in the track. As the laser power increases, periodic bubbles appear in the track, and foam layers form when the laser power is even higher. As would be expected the distance between bubbles increases as the scan speed increases regardless of the laser power.

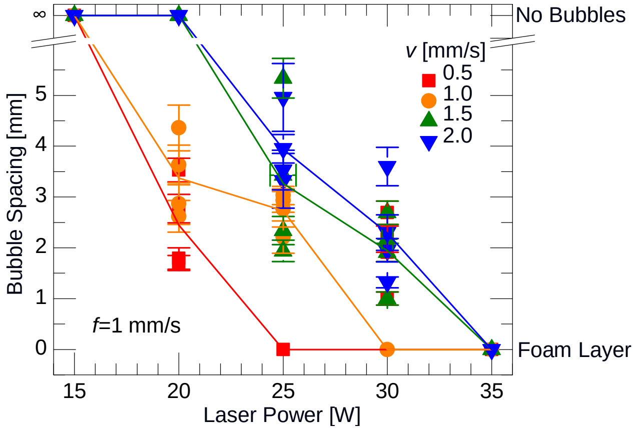

Figure 3.2 Bubble periodicity results with 1 mm/s feed rate

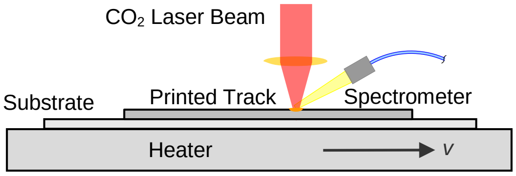

Figure 3.3 Schematic of filament scanning process with spectrometer focused on the molten region.

Due to the complex nature of the dynamics of the melt pool during the filament feeding process, the problem was simplified by eliminating the feeding process as a possible cause of the periodic bubbles. As illustrated in Figure 3.3, a glass filament was placed horizontally on the substrate and scanned along its center by the laser. The only control variables were the scan speed, *v*, and laser power, *P*. A USB 4000+ (Ocean Optics) visible spectrometer was positioned to collect visible radiation emitted from the molten region. This was calibrated to measure relative spectral irradiance using a Ocean Optics LS-1-CA 2800 K light source.

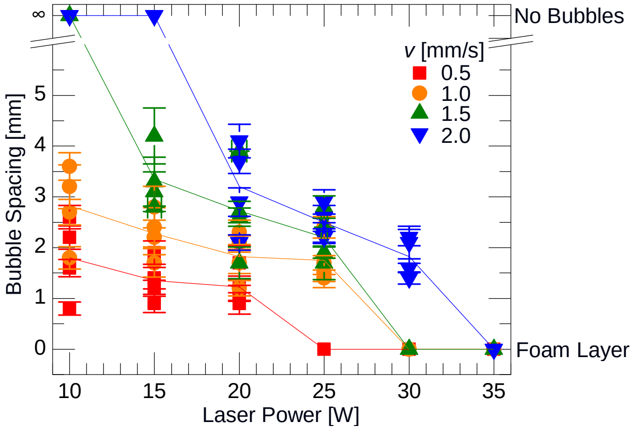

Figure 3.4 Bubble spacing for filament placed on the substrate.

In this experiment, the scan speed varied from 0.5 to 2 mm/s, and the laser power varied from 10 W to 50 W. The same bubble formation shown in Figure 3.1 was also observed. The bubble spacing was measured and shown in Figure 3.4. Similar to the filament-fed process, the bubble distances decrease with laser power and increase with scan speed. This result indicates that the formation of periodic bubbles is not caused by the filament feeding process.

In both experiments, visible light was emitted from the laser heated, molten region during deposition. The spectral irradiance on the spectrometer is plotted in Figure 3.5 for various laser powers and a scan speed of 1 mm/s. A peak at λ_0=589 nm occured for each case, except when the laser power was 10 W which corresponds to the only case at which bubbles were not observed. The generation of a foam layer was accompanied by strong fluctuations in the irradiance on the spectrometer during scanning, whereas the signal from bubble free tracks or tracks with periodic bubbles were relatively steady. This temporal signal can be related to the travel distance and the irradiance at λ_0=589 nm is plotted as a function of the length along the track in shown in Figure 3.6.

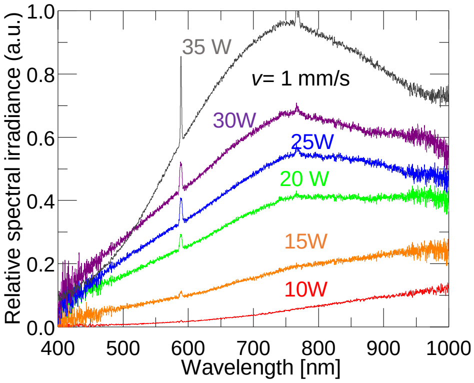

Figure 3.5 Radiation spectra of melt pools for different laser powers for filament scanning for scan speed of 1.0 mm/s

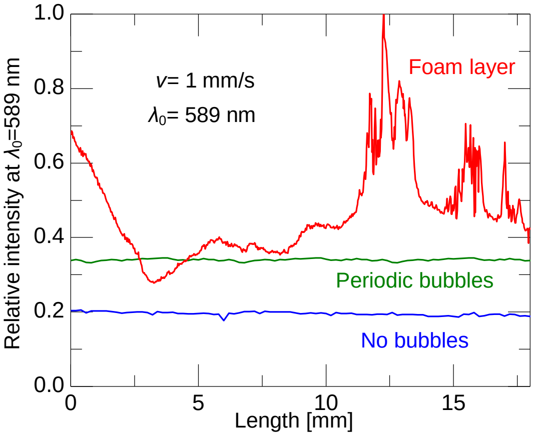

Figure 3.6 Melt pool radiative intensity at λ=589 nm with respect to position (calculated from time) for three different laser scanned filaments

4. DISCUSSION

According to Naumann et. al. [19], reboil of soda-lime glass requires a temperature of at least 1430 °C. It is difficult to precisely measure the temperature of the glass from the curves in Figure 3.5, because the interrogation region (D~1 mm) is larger than laser diameter. However the broad peak in the spectral irradiance at ~λ=770 nm for laser powers greater than 25 W, imply that the melt pool temperature is higher than 1500 °C from Wien's displacement law. This implies that the creation of the foam layer is due to the reboil of soda-lime glass. It also suggests that glass is vaporizing at the top of the molten region. The recoil pressure may be sufficient to the foam formed at the surface into the molten region. Vaporization of lighter elements in the glass is consistent with the observation of the Na doublet at 589 nm in Figure 3.5 for higher laser powers [21]. Also, the other peak at 776 nm in the spectrum intensity indicated the breakdown of potassium [22].

Finite volume simulation predicts lower temperatures for the lower laser powers, consistent with broad peaks beyond 1000 nm. This suggests the possibility that periodic bubble formation is occurring at a lower temperature than the critical temperature for reboil to occur. One possibility is that the top of the filament, directly exposed by the laser, softens to the point that it flows/slumps along the colder glass in contact with the substrate. During this process, air is trapped inside the glass. As the top of the filament melts, the material runs down the side and traps air in the gap between the bottom of the filament and the substrate. Surface tension draws the gas pockets to form spherical inclusions. Figure 3.6 supports this conclusion because there is no periodic spike intensity at 589 nm associated with bubble formation.

The tracks were polished back to the center line along the scan direction. A dark field optical micrograph is shown in Figure 4.1. The bubbles closer to the point where the laser started are closer to the top of the filament. This may indicate that the bubbles rose due to buoyancy through molten glass.

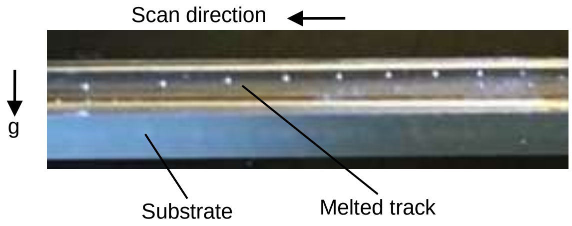

Figure 4.1 Bubble distribution in ground track

It is difficult to remove the bubbles once they have formed. For example, four tracks with periodic bubbles (created with a scan speed of 1 mm/s and a laser power of 20 W) were scanned with the same parameters the second time. The periodic bubbles remained after the track was rescanned with same parameters two times.

While it is possible to create a track with no bubbles when the laser power is very low, the bond between the filament and substrate will be weak. One possibility is to deposit bubble-free tracks. Once a good conduction path is established with the substrate, the track can be rescanned with higher laser power to reduce the contact angle. To test this hypothesis, four tracks were first scanned with a scan speed of 2 mm/s and a laser power of 10 W. No bubbles were produced, and they were attached to the substrate. These tracks were then scanned by the laser a second time with a scan speed of 1 mm/s and a laser power of 20 W. Tracing the tracks with higher laser power produced a wider track (reduced contact angle) and did not introduce bubbles.

5. SUMMARY AND CONCLUSIONS

Laser melted glass is prone to bubble formation. This paper explored bubble formation in two processes; filaments were deposited by feeding them into a laser generated melt and a laser was scanned along a stationary filament. . Three different bubble regimes were common to both experiments; bubble-free, periodic bubbles, and a bubble foam. At lower energy doses (laser power normalized to scan speed) bubbles do not occur. For very high energy doses, a foam forms consisting of multiple bubbles and is consistent with the vaporization and reboil phenomena in the glass. Periodic bubbles occur in the at intermediate energy doses with a greater bubble density for higher energy doses. From a process control standpoint, the foam layers can be avoided by minimizing the laser power. This has a distinct spectral signature which will help with process monitoring. Establishing good contact between the filament and the substrate appears to be critical for minimizing the formation of periodic bubbles and it has been demonstrated that well bonded bubble free tracks can be formed by reflowing tracks deposited with lower power. The physical phenomena behind the periodic bubbles is interesting and remains an open question.

ACKNOWLEDGMENT

This work was supported by the National Science Foundation (CMMI-1538464).

REFERENCES

[1] Luo, J., Pan, H., and Kinzel, E. C., 2014, "Additive manufacturing of glass," Journal of Manufacturing Science and Engineering, 136(6), pp. 061024.1-6.

[2] Pilon, L., Fedorov, A. G., Ramkrishna, D., and Viskanta, R., 2004, "Bubble transport in three-dimensional laminar gravity-driven flow – mathematical formulation," Journal of Non-Crystalline Solids, 336(2), pp. 71-83.

[3] Shelby, J. E., 2005, Introduction to glass science and technology, Royal Society of Chemistry.

[4] Schreiber, H. D., Kozak, S. J., Balazs, G. B., Fritchman, A. L., and Schreiber, C. W., 1989, "Equilibrium and Transport Properties of Gases in E-Glass Melts," Journal of the American Ceramic Society, 72(9), pp. 1680-1691.

[5] Cowan, J. H., Buehl, W. M., and Hutchins, J. R., 1966, "An electrochemical theory for oxygen reboil," Journal of the American Ceramic Society, 49(10), pp. 559-562.

[6] Ramos, J., 1986, "Behavior of multicomponent gas bubbles in glass melts," Journal of the American Ceramic Society, 69(2), pp. 149-154.

[7] Pilon, L., and Viskanta, R., 2004, "Bubble transport in three-dimensional laminar gravity-driven flow–numerical results," Journal of non-crystalline solids, 336(2), pp. 84-95.

[8] Kloužek, J., Němec, L., Arkosiova, M., Jebava, M., and Tonarová, V., 2008, "Determination of gas propertiers in glass melts," Ceramics− Silikáty, 52(2), pp. 66-71.

[9] Beerkens, R. G., and Schaaf, J., 2006, "Gas release and foam formation during melting and fining of glass," Journal of the American Ceramic Society, 89(1), pp. 24-35.

[10] Fedorov, A. G., and Pilon, L., 2002, "Glass foams: formation, transport properties, and heat, mass, and radiation transfer," Journal of Non-Crystalline Solids, 311(2), pp. 154-173.

[11] Pilon, L., 2002, "Interfacial and transport phenomena in closed-cell foams," Purdue University.

[12] Goldman, D. S., Brite, D. W., and Richey, W. C., 1986, "Investigation of Foaming in Liquid-Fed Melting of Simulated Nuclear Waste Glass," Journal of the American Ceramic Society, 69(5), pp. 413-417.

[13] Jebava, M., Nemec, L., and Klouzek, J., 2004, "Kinetic and equilibrium data of gasses in glass melts," Ceram. Silik, 48, pp. 121-127.

[14] Pigeonneau, F., Martin, D., and Mario, O., 2010, "Shrinkage of an oxygen bubble rising in a molten glass," Chemical Engineering Science, 65(10), pp. 3158-3168.

[15] Němec, L., and Cincibusová, P., 2005, "The bubble distribution in glass refining channels," Ceramics− Silikáty, 49(4), pp. 269-277.

[16] Luo, J., Gilbert, L., Qu, C., Wilson, J., Bristow, D., Landers, R., and Kinzel, E., 2015, "Wire-Fed additive manufacturing of transparent glass parts," ASME 2015 International Manufacturing Science and Engineering Conference, ASME, Charlotte, NC, USA, pp. V001T002A108. 1-5.

[17] Klein, S., Simske, S., Adams, G., Parraman, C., Walters, P., Huson, D., and Hoskins, S., "3D Printing of Transparent Glass," Proc. NIP & Digital Fabrication Conference, Society for Imaging Science and Technology, pp. 336-337.

[18] Chen, R. K., Lo, T. T., Chen, L., and Shih, A. J., 2015, "Nano-CT Characterization of Structural Voids and Air Bubbles in Fused Deposition Modeling for Additive Manufacturing," ASME 2015 International Manufacturing Science and Engineering Conference, ASME, Charlotte, NC, pp. V001T002A071.1-7.

[19] Naumann, K., and Ott, F., 2000, "Earth-alkaline aluminoborosilicate glass for lamp bulbs," Schott Glass, Germany.

[20] Pilon, L., Janos, F., and Kitamura, R., 2014, "Effective thermal conductivity of soda-lime silicate glassmelts with different iron contents between 1100°c and 1500°c," Journal of the American Ceramic Society, 97(2), pp. 442-450.

[21] Allcock, G., Dyer, P., Elliner, G., and Snelling, H., 1995, "Experimental observations and analysis of CO_2 laser-induced microcracking of glass," Journal of applied physics, 78(12), pp. 7295-7303.

[22] Lee, Y.-I., Song, K., and Sneddon, J., 2000, Laser-induced breakdown spectrometry, Nova Publishers.

V. ADDITIVE MANUFACTURING OF TRANSPARENT BOROSILICATE GLASS USING A FILAMENT-FED PROCESS

Junjie Luo[a], John M. Hostetler [a], Douglas A. Bristow[a], Robert G. Landers[a],
Jonathan T. Goldstein[b], Augustine M. Urbas[b], Edward C. Kinzel[a]
[a]Department of Mechanical and Aerospace Engineering
Missouri University of Science and Technology, Rolla, Missouri 65409, U.S.A
[b]Air Force Research Laboratory, Materials and Manufacturing Directorate, Wright-Patterson Air-Force Base, OH, USA 45433

ABSTRACT

This paper investigates Additive Manufacturing (AM) of transparent borosilicate glass using a filament-fed process. Borosilicate glass is widely used in science, engineering, optics, and other areas due to its high transmissivity, low coefficient of thermal expansion (CTE), and high chemical resistance. In this study, borosilicate glass filaments are fed into the workpiece and melted by a CO_2 laser beam to deposit the glass continuously. The heat transfer inside the glass is the most important factor for determining the morphology and optical quality of the printed glass. Initially, laser scanning over 2mm and 3mm filaments is studied. It is found that the filament size is a key factor for the morphology of the track. A larger filament diameter resulted in a longer time for heat conduction, and bubbles from reboil were found in all fully melted 3mm filaments. Monolayers were printed with different track spacing and feed rates, the result of which proved that void-free monolayers may be obtained by depositing fully melted tracks with appropriate track spacing. In addition, 3D cubes were printed with void-free monolayers. The measured transmissivity of the best printed cube was only 1% less than the ideal value (zero absorption). Finally, cylindrical surfaces with designed diameters were obtained via the overlapping of monolayers. A fiber laser beam focused by the printed cylindrical surfaces was measured by a beam profiler, the results of which implied that the printed samples may also function as cylindrical lenses.

Key words: additive manufacturing, borosilicate glass, filament fed process, transparent

1. INTRODUCTION

Additive manufacturing (AM) technology has been a field of particular interest in recent years, due in part to the advances in manufacturing that these processes entail. Such advances relate to the printing of complex structures both quickly and affordably, as well as the ability to fabricate unique structures that are impossible to replicate with conventional manufacturing.. Various AM techniques for transparent materials have been studied, among which include 3D printing of transparent polymers, ink-jet printing of polymers [1-4], ink-jet printing with in-situ UV curing [5], and selective laser sintering of polymer powders with post processing of index-matched plastic infiltration [6]. Transparent polymer parts have also been printed using these techniques, such as curved display surfaces, sensors and interactive devices [1-3], non-imaging optics using PMMA [4], and even GRIN devices [5].

While transparent polymers have their applications, they are not typically suitable for high quality optics due to their limitations in optical and mechanical properties. In comparison to polymers, glasses have a higher transmittance, lower coefficient of thermal expansion, better chemical resistance, and a more stable index of refraction when subjected to large temperature gradients [7]. Despite this, there have only been a handful of studies conducted on AM of glass, most of which are focused on the realization of 3D structures. Selective laser melting/sintering (SLM/SLS) was studied for the printing of soda lime glass [8, 9], fused quartz [10] and borosilicate glass [11] with an emphasis on the dimensional accuracy of fabricated parts. Glass powder mixing with a maltodextrin binder was deposited using 3D printing, and fired in a kiln to burn out the binder [12]. Cold extrusion of wet paste has been used to build colored glass parts, bioglass bone scaffolds [13, 14], and ceramics [15-17]. All of these processes require post-processing in a furnace to evaporate the water out of the paste, densify glass particles to allow high mechanical strengths to be obtained. While the above processes are capable of printing solid glass parts, these printed parts are all opaque. Klein et al. has developed a hot extrusion technique that can print transparent soda lime glass [18], but this soft glass flowing process is hard to control. Luo et al. developed a filament fed process that can print 3D transparent parts of soda lime glass fused quartz [19-24].

In addition to soda lime and fused quartz, borosilicate glass is widely used in science and engineering fields such as optics, chemistry, electronics, and hermetic seals. In comparison to soda lime glass, borosilicate glass (Duran 3.3) has a higher transmittance in the visible wavelength range, and a much smaller coefficient of thermal expansion ($\sim 3.3\times10^{-6}$ K^{-1}) [25] which is only one third that of soda lime glass ($\sim 9.5\times10^{-6}$ K^{-1}) [26]. Therefore, borosilicate has a much greater resistance to thermal shock. Additionally, the working point of Duran 3.3 (~1260 °C) [25] is about 1300 °C lower than that of fused quartz (~2600 °C) [26], which makes it much more easily melted by the CO_2 laser beam. Therefore, borosilicate glass is a suitable material for AM process using laser melting.

In this paper, borosilicate glass filaments were studied for their viability in glass AM. Filaments with diameters of 2mm and 3mm were scanned by the laser in order to study the effect of filament diameter on the morphology of melted single tracks. 2mm filaments were subsequently selected for further printing experiments. Void-free monolayers and 3D cubes were then printed with the appropriate parameters. Finally, three cylindrical lenses were printed to match designed surface profiles, and the focal distances of these cylindrical lenses are validated experimentally.

2. EXPERIMENTAL SETUP

The experimental setup and a photo of the printing process are shown in Figure 2.1. 3mm thick borosilicate glass plates were clamped to a heater and used as a substrate. The heater was fixed on a set of x-y-z stages. The *x* and *y* stages (Aerotech ANT130-160XY) realized the horizontal movements, and a *z* stage (Aerotech ATS100-150) was used to move the platform upwards and downwards. Schott Duran 3.3 glass 2mm and 3mm filaments were used in this study. A CW CO_2 laser (Synrad Evolution 125, λ_0=10.6μm) was incident on the printing surface. The filament was fed into the melt pool (intersection of laser beam and substrate) by a custom-designed filament feeder. The Full Width Half Maximum (FWHM) diameter of the laser beam at the melt pool was measured to be 4.2mm. 1% of the laser energy was reflected into a thermopile type power meter (Ophir 10A-V1) so that the laser power at the printing surface could be determined. Incandescent light was emitted from the melt pool during the printing process; the spectrum of the radiation was dependent on the temperature of the melted glass. This incandescent emission was collected using an OceanOptics USB-4000 fiber-coupled spectrometer (calibrated with an OceanOptics LS-1-CA 2800K light source) which has a 0.8mm diameter interrogation region centered on the laser heated area.

Borosilicate glass may be printed on non-heated substrates without fracture for small volume parts (< 10mm thickness) due to the material's low CTE. However, for larger volume printing cracking is inevitable without preheating the substrate. In order to solve this cracking issue, a heater was used to maintain the substrate at a temperature of 450°C, at which point no printed parts were observed to crack in the experiments.

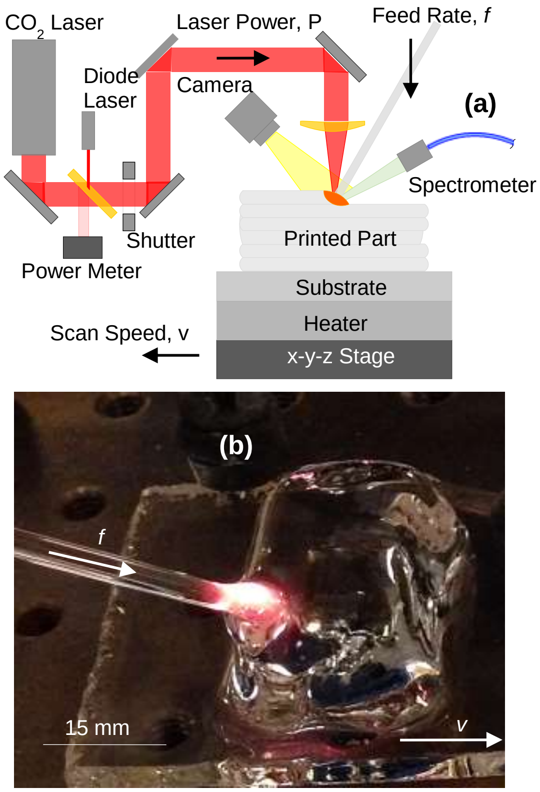

Figure 2.1 (a) Schematic of the experimental setup (b) an example of the printing process

In this study, 2mm and 3mm diameter Duran 3.3 borosilicate glass filaments manufactured by Schott AG were used. The physical properties of this glass are given in Table 2.1 [25].

Table 2.1 Physical properties of Duran 3.3 glass

Density (20 °C) [g/cm3]	2.23	Annealing Point [°C]	560
Young’s Modulus [kg/mm2]	6400	Strain Point [°C]	525
Working Point [°C]	1260	Softening Point [°C]	825
Refractive Index (λ= 587.6 nm)	1.473	Young’s modulus [N·mm^{-2}]	63×10^3

3. RESULTS AND DISCUSSION

3.1. PREVENTION OF BUBBLE FORMATION IN THE PRINTED GLASS

Several different bubble regimes were observed in the printed glass, and subsequently three different mechanisms for bubble formation were found through experimental study. The first mechanism involved contaminants on the filament surface. An experiment was conducted to verify the effect of filament contamination on bubble formation: Two 30mm long filaments were selected to be scanned by the laser beam with identical platform parameters, in which one of the filaments was cleaned prior to laser melting and the other filament was contaminated with silica powder on the surface. It was found that the track melted from the contaminated filament contains a large number of bubbles, while the track melted from the cleaned filament was nearly bubble free. The other two mechanisms of bubble formation were surface defects on the filaments and reboil of glass at high temperatures, which were both demonstrated in our previous studies [24]. Bubbles caused by surface defects and contamination may easily be avoided by screening and cleaning the filaments, while bubbles caused by reboil can be prevented by using appropriate platform parameters.

In the interest of minimizing bubble formation in printed parts, all of the filaments were selected to be defect-free and cleaned for subsequent experiments. However it was still possible that bubbles would due to contamination of dust from the air, as all of the experiments were conducted in an open environment. Additionally, bubbles may also result from small scratches on the filaments that could not be detected by human eyes. However, the amount of these bubbles are relatively insignificant and are maintained at the lowest degree.

3.2. SINGLE TRACK SCANNING

Due to the low thermal conductivity of borosilicate glass, changes in filament diameter may lead to significant differences in the laser deposition process. In order to compare the deposition performance of the two filament diameters, the process of laser beam scanning of the filaments was investigated.

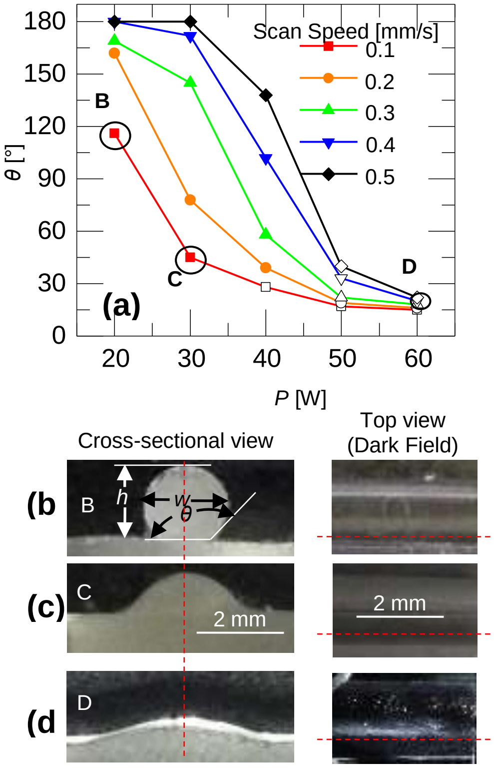

Figure 3.1. Experimental results for laser scanning 2mm filaments

There are three main features of the deposited track: the height, *h*, width, *w*, and contact angle, θ (Figure 3.1(b)). In this experiment, the cross-sectional area of each track was the same due to the fact that the deposition rate (volume of filament per unit length) is fixed. As a result, the height and width of the deposited track are both a function of contact angle. In multi-track layer printing, a contact angle larger than 90° would result in voids inside the layer because the gap between the previous track and the substrate could not be filled by the next track. Therefore, the contact angle is the most important feature in the single track deposition process. If the bottom of the filament is melted, the contact angle should be less than 90° because the gap between the filament and substrate can be filled by flowing glass at the bottom.

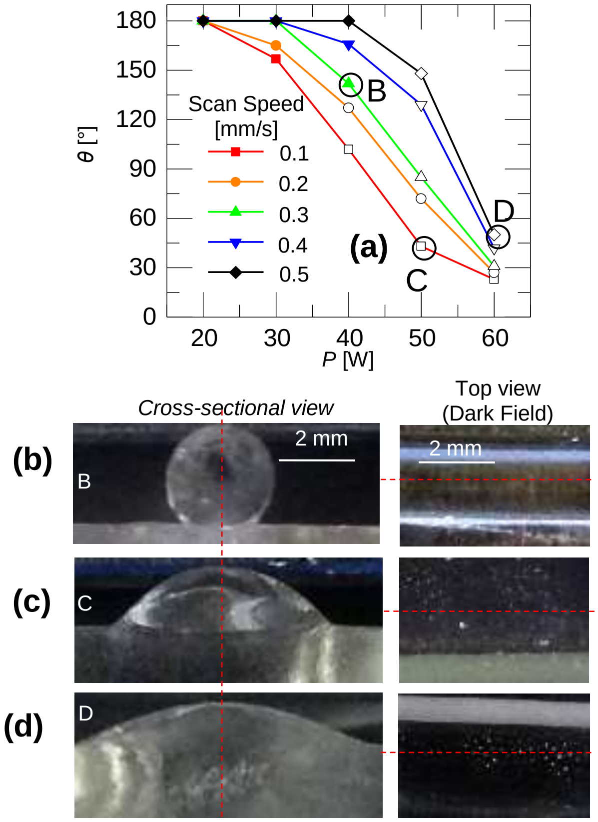

Figure 3.2. Experimental results for laser scanning 3mm filaments

Figure 3.1 depicts the contact angle distribution of tracks deposited by laser scanning of 2mm filaments with different scan speeds and laser powers, including the cross-sectional and top-down views of three representative samples where the top-down photos are taken in a dark background with light illuminating the side of samples. The empty symbol in Figure 3.1(a) represents tracks with dense bubbles inside. The contact angle decreased with increasing laser power at each scan speed due to the fact that the glass has a lower viscosity at higher laser powers and therefore flows more. With 0.1 mm/s scan speed, the contact angle decreased gradually with laser power. With a 0.5 mm/s scan speed, the contact angle was nearly 180° at 20W and 30W, indicating that the shape of the filament did not change while being laser scanned. From 40W to 50W, the contact angle drastically decreased. It is worth noting that numerous bubbles were observed in tracks with small contact angles (<90°) (Figure 3.1(g)), while no obvious bubbles were found in tracks with small contact angles which are printed with a low scan speed and laser power, as shown in Figure 3.1(c).

Similar to Figure 3.1, Figure 3.2 depicts the results of laser scanning 3mm filaments. The trend of contact angle changing with laser power and scan speed for 3mm filaments was similar to that found with 2mm filaments. However, in all of the tracks scanned with smaller contact angles, dense bubbles were observed. Because all of the filaments were cleaned and selected to be defect free on their surfaces, the dense bubbles formed in these deposited tracks were determined to be caused by reboil at high temperatures. The deposition of a track required the heat to be conducted from the top to the bottom of the filament. At high scan speeds, the temperature difference was greater than that for lower scan speeds with the same laser power, as there was less time for heat conduction to occur. For 3mm filaments, while the contact angle as smaller than 90°, reboil occurred even at a scan speed of 0.1 mm/s. This result implies that the melting of 3mm filaments requires a very high temperature difference between the top and bottom surface, which makes the deposition of 3mm filaments a much slower process than that of 2mm filaments.

3.3. SPECTROSCOPY

The incandescent light emitted from the melt pool was monitored using a spectrometer. The spectral result of laser scanning 2mm filaments at 0.1 mm/s scan speed is shown in Figure 3.3; Figure 3.3(a) demonstrates the spectral distribution corresponding to when the laser beam was at the center of the track, and Figure 3.3(b) depicts the relative intensity averaging from 600 to 750 nm versus scanning time. In Figure 3.3(a), a peak intensity at 589nm was observed for laser powers greater than 20W. Given that Duran 3.3 glass contains sodium [25], this peak at 589nm indicates the excitation of sodium ions in the glass, as proven by Allcock et al. [27].

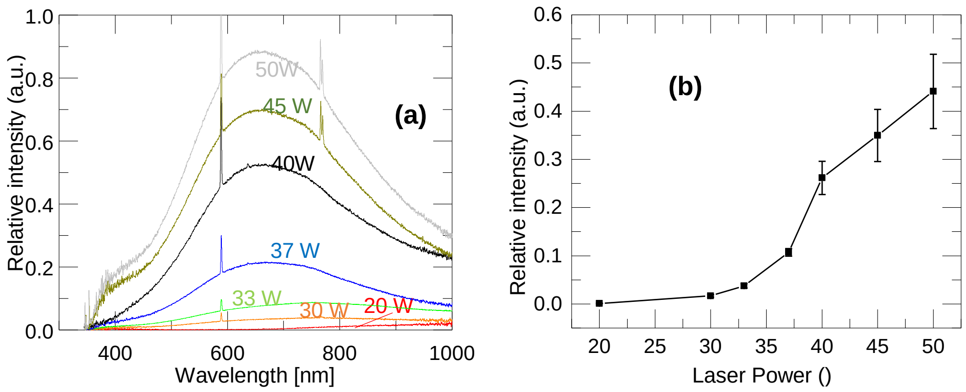

Figure 3.3 (a) Spectral distribution from the melt pool for 2mm filaments with 0.1 mm/s scan speed (b) intensity averaging from 600 to 750 nm wavelength as a function of time

Despite the peaks at 589nm, the wavelengths at the spectrum peak in these curves decrease with increasing laser power from 20-40W, but remain constant from 40-50W. This result indicates that the peak wavelength in thermal radiation for borosilicate glass shifts towards a shorter wavelength, similar to a grey body; however the radiation peak does not change as reboil occurs. At 45 W laser power, another peak at 776nm appears, indicating the breakdown of potassium in the glass [32].

In Figure 3.3(b), the intensity averaging from 600 to 750 nm was relatively stable at 20W and 30W, but fluctuated greatly above 40W. This fluctuation of intensity was the result of reboil occurring in the melt pool, as the intense bubble formation causes a strong scattering of light emission from the melt pool. This result indicates that bubble formation due to reboil may be monitored using a spectrometer focused on the melt pool.

3.4. MONOLAYER PRINTING

Monolayers may be printed by depositing single tracks in a parallel pattern along the substrate. In this experiment, laser power was maintained at a constant value of 30W because a higher laser power results in reboil on the surface at low scan speeds. The ratio of feed rate and scan speed was always equal to one, and the scan speed ranged from 0.1-0.5 mm/s. The space between adjacent tracks ranged from 1.5-3.5mm. The morphology distribution as a function of scan speed (feed rate) and track spacing is shown in Figure 3.4(e). There were four types of layer morphology, and the representative cross-sectional view of each type is shown in Figure 3.4. The four types are: a) stacking up, b) uniform height, c) separated, and d) voids at the bottom. At low scan speeds (0.1 and 0.2 mm/s), the layer height was observed to stack up while the track spacing was too small, as depicted in Figure 3.4(a). As the track spacing increases, monolayers with uniform height voids were printed, as shown in Figure 3.4(b).

At high scan speeds (0.3-0.5 mm/s), when the track spacing was too large, the tracks lose touch with adjacent tracks, as shown in Figure 3.4(c). With low track spacing, voids at the bottom of the layer were observed. The voids form because there were gaps between the track and substrate resulting from a large contact angle (>90°), which was mentioned above in the single track printing result; the gaps could not be filled by subsequent tracks. Therefore only tracks with small contact angles may be used to print void-free monolayers.

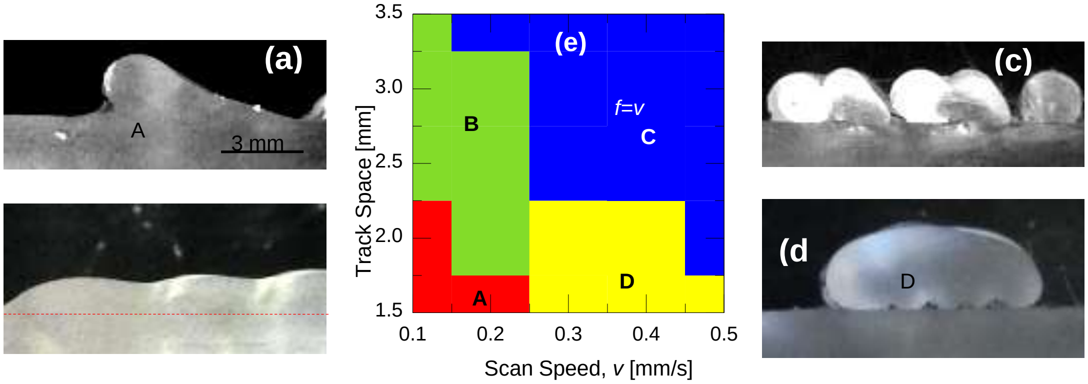

Figure 3.4 Morphology of printed monolayers: (a-d) photographs of four types of layer morphologies; (e) process map showing type of monolayer as a function of scan speed and track space

3.5. 3D CUBE PRINTING

When void-free monolayers can be printed, transparent 3D parts may be obtained through the overlapping of monolayers. In this experiment, each cube was printed with seven monolayers, and each monolayer consisted of six tracks with 2.5mm track spacing. The parameters for printing these cubes were 0.1 mm/s feed rate and scan speed, with laser powers ranging from 25-35W. All of the printed cubes were sectioned vertically at the center and polished on both sectioned plane surfaces. To quantify the transparency of the printed cubes, the transmission of a He-Ne laser (λ_0 = 633nm) beam through the sample was measured at normal incidence. A Newport Model 1935-C power meter was used to measure the power of the original laser beam and the transmitted beam.

While the thickness of the sample was reduced after polishing, the extinction coefficient is comparable. The extinction coefficient was calculated using the Beer-Lambert law

$$\alpha = \frac{1}{L}\ln\left[(1-R)^2/\tau\right] \qquad (1)$$

where τ is the measured transmittance of the laser beam, R is the reflectivity of the glass at one surface, and L is the thickness of the sample. *R* was calculated from the refractive index, *n* at λ=633 nm with $R = [(1-n)/(1+n)]^2$ at normal incidence.

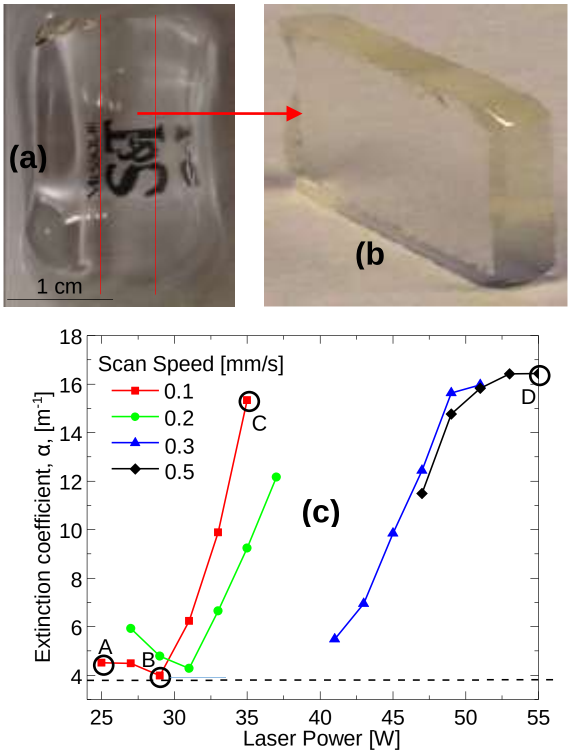

Figure 3.5 Sample printed with 29 W laser power (top) Image of a 1951 USAF resolution chart (bottom)

Figure 3.5 shows the extinction coefficient as a function of laser power at different scan speeds. At a 0.1 mm/s scan speed and laser powers ranging from 25-29W, α decreases slightly as the laser power increases, with a minimum value of 3.89 m^{-1} at 29W corresponding to a sample thickness of 4.9mm and a 0.90 transmittance. When the laser power is greater than 29W, α increases quasi-linearly with laser power. The sample printed with 35W is 5.2mm thick with a 0.86 transmittance. Dark-field images of a sectioned sample at 25W, 29W and 35W with a 0.1 mm/s scan speed are shown in figure 3.6. It may be seen that the slightly higher α at a low power is due to the striaes between layers, and the significant α increase at higher laser powers is caused by bubble formation. The trend of α at 0.2 mm/s is similar to that of 0.1 mm/s, but the lowest α observed for a 0.2 mm/s scan speed has a greater value than its 0.1 mm/s counterpart. Values for α at 0.3 mm/s and higher scan speeds simply increase with laser power since the peak temperature is much greater. It should be noted that bubbles exist in all samples for these scan speeds.

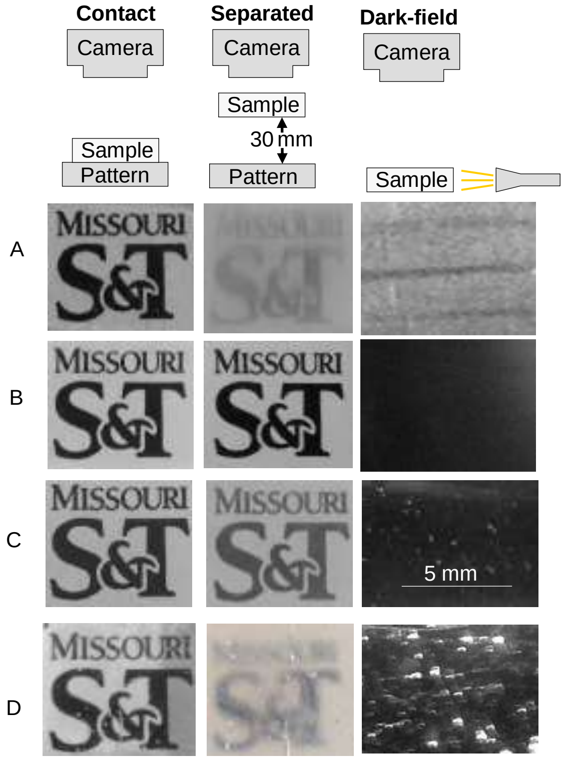

Figure 3.6 Photographs of samples in different conditions; in contact with background (left column), 30mm separation from the background (middle column), and dark-field (right column). Rows A, B, C and D represent samples marked as A, B, C and D in Figure 3.5 respectively

The transmittance of the substrate was measured using the same method outlined above. The transmittance was measured to be 0.92 with a 3.01mm sample thickness, with a corresponding extinction coefficient of 3.55 m^{-1}. Therefore the transparency of printed parts is very close to that of conventionally manufactured borosilicate glass [25], which is indicated by the dashed line in figure 3.5. In addition, this value for transmittance is much lower than that of soda lime glass, which is 8.3 m^{-1} [31].

Figure 3.6 depicts photographs of a pattern transmitted through samples marked A, B, C and D, as well as corresponding dark-field images of these samples. The images in the first column were taken while the samples are in direct contact with the pattern. The second column consists of photos which were taken after the samples were separated from the pattern by a distance of 30mm. The third column provides dark-field images which were taken by illuminating the side of the samples and imaging the light that was scattered as a result of defects in the glass. In the first column, all of the four images were clear, while some scattering was observed in sample D; this scattering is caused by bubbles formed at higher laser powers. In the second column, the image transmitted through sample B was as clear as its corresponding contact image, while the image through sample A was significantly blurred. There were no single bubbles found in the dark-field image of sample A, however striaes were observed. The blurring of this image is therefore caused by striaes which were formed due to insufficient laser energy. The images transmitted through samples C and D were also blurred by bubbles, and their respective dark-field images depicted the scattering of light due to these bubbles. Bubbles of this nature are formed because the laser energy is too high. The bubbles in sample D were much larger than those in sample C, so the image through C was more blurred. Also, the extinction coefficient in D was greater than it is for C.

3.6. CYLINDRICAL PROFILE PRINTING

Curvature profiles may be printed through the overlapping of monolayers with different widths, but the surface smoothness is limited by the filament size. According to Ref. [27-29], the unsmooth surface of the glass may be smoothened by scanning it with a CO_2 laser beam. This smoothening effect occurs as a result of a flow which is driven by surface tension in the softened region that is heated by the laser beam. Moreover, the surface tension-driven flow occurs only if the softening of the surface lasts for a sufficient amount of time. An example of the printing process for a cylindrical surface is shown in Figure 3.7(a). Therefore, through a combination of different monolayers, 3D cylindrical profiles may be printed after laser-reflowing of the surface. Three cylindrical profiles were designed with three monolayers each.

Three sections of cylindrical surfaces were printed with 0.1 mm/s scan speed and feed rate, 29W laser power, and reflowing of the surface by the laser beam at a power of 25W and 0.1 mm/s scan speed with a 2 mm space between tracks. Figure 3.7(a) provides examples of surface profiles in different stages of the printing process. Each of the samples consist of three monolayers, the surface profiles of which are depicted in Figure 3.7(b-d). The radius of each printed piece after laser reflowing is designed to match a predetermined value. At the top of the profile, the radii of the printed samples are found to be close to the design value. However the radius deviates from the design value at the edges because the edges are flattened along the substrate during the reflowing process.

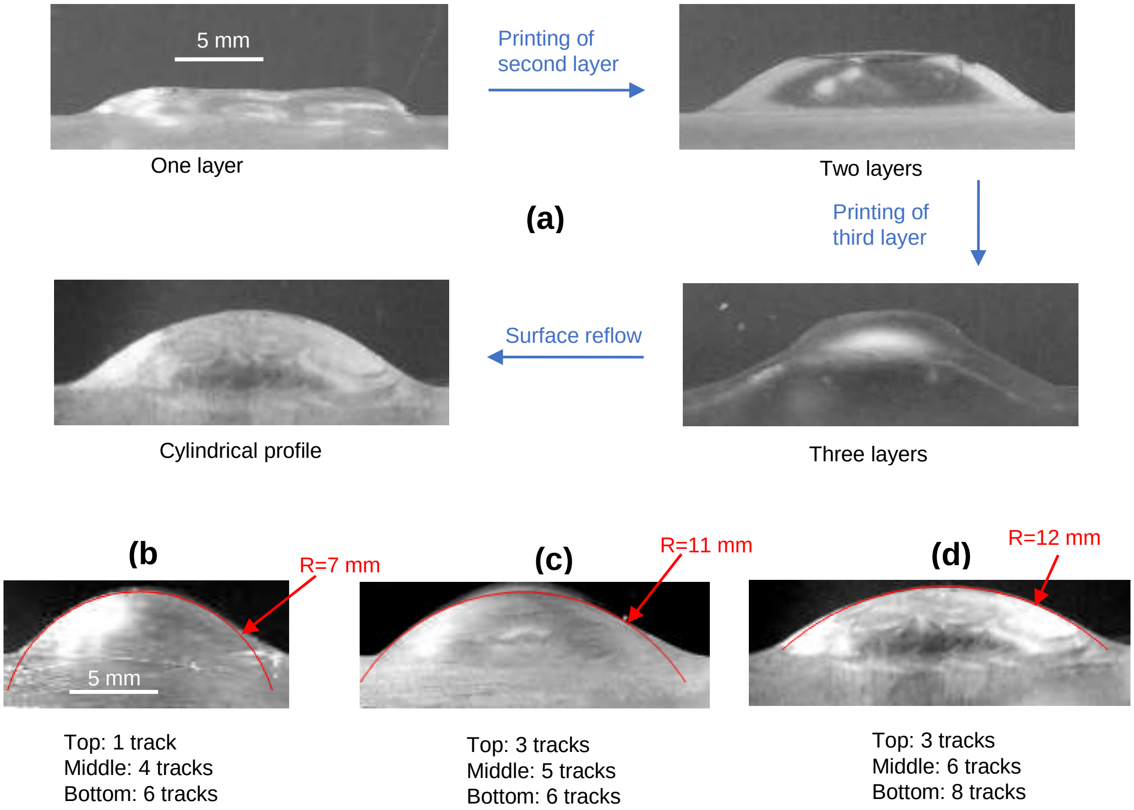

Figure 3.7 Cylindrical profile printing results

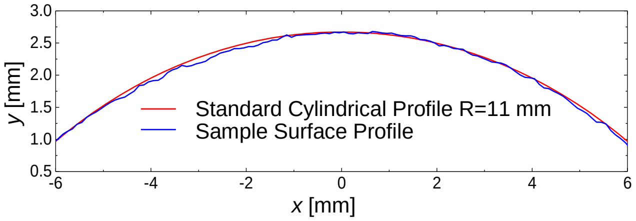

Figure 3.8 Sample surface profile obtained via laser scanning compared to a standard cylindrical profile with 11mm radius

Figure 3.8 shows the profile of the cylindrical surface depicted in Figure 3.7(c), which was obtained by laser scanning of the surface. The laser scanned profile matches very closely to a standard cylindrical surface with an 11mm diameter. It should be noted that the accuracy of the laser scanned surface is limited by the resolution of laser scanner used.

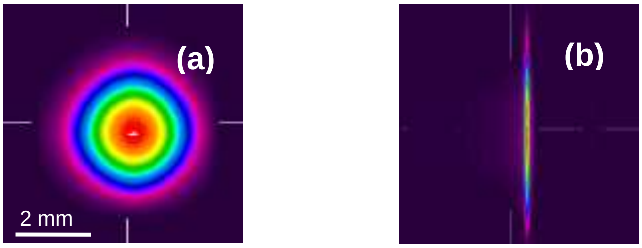

Incident beam
Beam width, *w*= 4250 µm

w= 51 µm
Diffraction limit, w_d= *8.4 µm*

f= 13.5 mm
Calculated *f*=12.75 mm

w= 58 µm
Diffraction limit, w_0= *13.3 µm*

f= 22.1 mm
Calculated f_0=21.2 mm

w= 59 µm
Diffraction limit, w_0= *14.5 µm*

f= 24.2 mm
Calculated f_0=23.3 mm

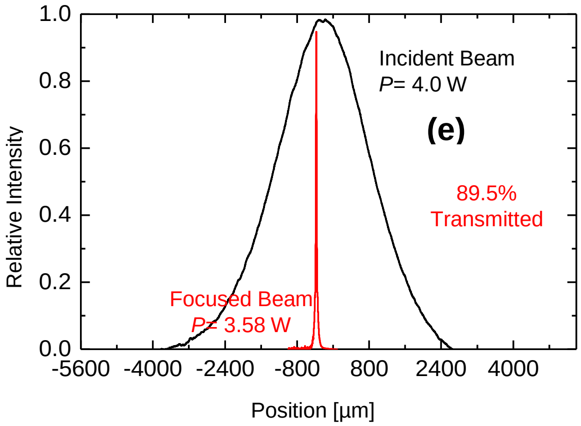

Figure 3.9 (a) Profile of the incident laser beam (b) focused laser beam through the R=7 cylindrical surface (c) focused laser beam through the R=11 cylindrical surface (d) focused laser beam through the R=12 cylindrical surface (e) normalized intensity of the incident beam and the beam focused by R= 7 mm cylindrical surface in (b)

The focusing capabilities of the printed cylindrical samples were determined by measuring the profile of a fiber laser beam (1.06 µm wavelength) focused by the samples using an Ophir NanoscanV2 beam profiler. The profile of the incident laser beam is shown in Figure 3.9(a), which follows a Gaussian distribution. The profiles of the laser beam focused by the three samples are shown in Figure 3.9(b-d). For all the three focused beams, the measured width is four times larger than the beam width of the diffraction limit, which is calculated by [32]

$$w = \left(\frac{4\lambda}{\pi}\right)\left(\frac{f}{D}\right) \tag{2}$$

where f is the focal length of the lens, λ is the wavelength of laser beam, D is the diameter of incident laser beam. Also, as indicated in the figure, the measured focal distance is about 5% larger than the value calculated from thick lens equation for all the three focused beams.

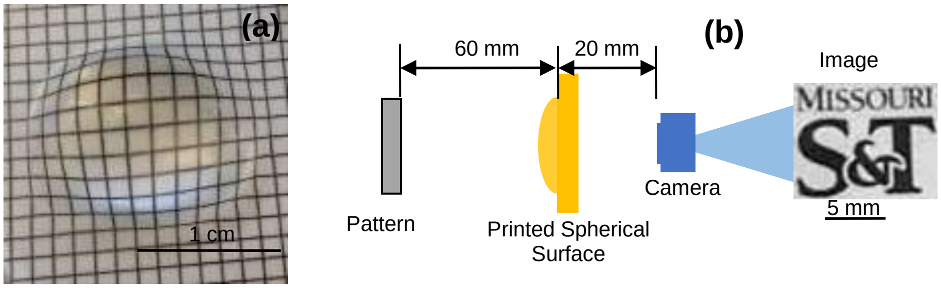

Figure 3.10 Image of the Missouri S&T logo taken through a printed convex sample

A simple spherical surface was also printed, as shown in Figure 3.10(a). This sample was made with three layers of circular paths (Figure 3.10(b)) using P = 30W, f = 0.1 mm/s, and v = 0.1 mm/s. The top surface is smooth after laser reflowing with 25 W laser power and 0.1 mm scan speed, and the back surface is polished to remove any contamination from the heater. A Missouri S&T pattern is projected on a camera through the spherical surface as shown in Figure 3.10(c). The image captured by the camera is clear, confirming the focusing capability of the printed spherical surface.

4. CONCLUSIONS

This paper demonstrates AM of Duran 3.3 borosilicate glass using a filament-fed process. 2mm and 3mm filaments were compared through a laser scanning experiment as well as with thermal modeling. 2mm filaments were shown to be the better diameter choice for the printing process due to the low thermal conductivity of borosilicate glass. Void-free monolayers were printed by depositing parallel tracks with the appropriate parameters. Also, transparent 3D cubes were printed through the overlapping of monolayers. The transmissivity of printed cubes were found to be close to that of conventionally manufactured borosilicate glass. Moreover, cylindrical surfaces were printed with three separate monolayers. The profiles of a laser beam focused by the printed cylindrical surfaces were measured, proving that the surfaces are able to function as cylindrical lenses. Finally, a convex cylindrical surface was printed, and an image was taken through the sample without distortion, confirming the high optical quality of the printed Duran glass.

REFERENCES

[1] Pereira, T., Rusinkiewicz, S., and Matusik, W., 2014, "Computational Light Routing: 3D Printed Optical Fibers for Sensing and Display," ACM Transactions on Graphics (TOG), 33(3), p. 24.

[2] Willis, K., Brockmeyer, E., Hudson, S., and Poupyrev, I., "Printed optics: 3d printing of embedded optical elements for interactive devices," Proc. Proceedings of the 25th annual ACM symposium on User interface software and technology, ACM, pp. 589-598.

[3] Blessing, K., and Richard Van, d. V., 2014, "Print head, upgrade kit for a conventional inkjet printer, inkjet printer and method for printing optical structures," Luxexcel Holding Bv., United States.

[4] Brockmeyer, E., Poupyrev, I., and Hudson, S., 2013, "PAPILLON: designing curved display surfaces with printed optics," Proceedings of the 26th annual ACM symposium on User interface software and technology, ACM, St. Andrews, Scotland, United Kingdom, pp. 457-462.

[5] Urness, A. C., Moore, E. D., Kamysiak, K. K., Cole, M. C., and McLeod, R. R., 2013, "Liquid deposition photolithography for submicrometer resolution three-dimensional index structuring with large throughput," Light: Science & Applications, 2(3), p. e56-e56.

[6] Niino, T., and Yamada, H., 2009, "Fabrication of transparent parts by laser sintering process:-transparentization of laser sintered plastic parts by infiltrating thermosetting epoxy with tuned refractive index," Journal of the Japan Society for Precision Engineering, 75(12), pp. 1454-1458.

[7] Weber, M. J., 2002, Handbook of optical materials, CRC Press, FL, USA.

[8] Fateri, M., and Gebhardt, A., 2015, "Selective Laser Melting of Soda-Lime Glass Powder," International Journal of Applied Ceramic Technology, 12(1), pp. 53-61.

[9] Luo, J., Pan, H., and Kinzel, E. C., 2014, "Additive Manufacturing of Glass," Journal of Manufacturing Science and Engineering, 136(6), pp. 061021-061026.

[10] Khmyrov, R., Grigoriev, S., Okunkova, A., and Gusarov, A., 2014, "On the possibility of selective laser melting of quartz glass," Physics Procedia, 56, pp. 345-356.

[11] Klocke, F., McClung, A., and Ader, C., 2004, "Direct laser sintering of borosilicate glass," The Proceedings of the 15th Annual SFF Symposium, University of Texas, Austin, TX, USA, pp. 214-219.

[12] Marchelli, G., Prabhakar, R., Storti, D., and Ganter, M., 2011, "The guide to glass 3D printing: developments, methods, diagnostics and results," Rapid Prototyping Journal, 17(3), pp. 187-194.

[13] Klein, S., Simske, S., Adams, G., Parraman, C., Walters, P., Huson, D., and Hoskins, S., 2012, "3D Printing of Transparent Glass," NIP & Digital Fabrication Conference, Society for Imaging Science and Technology, Canada, pp. 336-337.

[14] Fu, Q., Saiz, E., and Tomsia, A. P., 2011, "Bioinspired strong and highly porous glass scaffolds," Advanced functional materials, 21(6), pp. 1058-1063.

[15] Li, W., Ghazanfari, A., Leu, M. C., and Landers, R. G., 2015, "Methods of extrusion on demand for high solids loading ceramic paste in freeform extrusion fabrication," Annual International Solid Freeform Fabrication Symposium, University of Texas, Austin, TX, pp. 332-345.

[16] Ghazanfari, A., Li, W., and Leu, M. C., 2015, "Adaptive rastering algorithm for freeform extrusion fabrication processes," Virtual and Physical Prototyping, 10(3), pp. 163-172.

[17] Li, W., Ghazanfari, A., McMillen, D., Leu, M. C., Hilmas, G. E., and Watts, J. L., "Properties of partially stabilized zirconia components fabricated by the ceramic on-demand extrusion process," Proc. Annual International Solid Freeform Fabrication Symposium, pp. 916-928.

[18] Klein, J., Stern, M., Franchin, G., Kayser, M., Inamura, C., Dave, S., Weaver, J. C., Houk, P., Colombo, P., and Yang, M., 2015, "Additive Manufacturing of Optically Transparent Glass," 3D Printing and Additive Manufacturing, 2(3), pp. 92-105.

[19] Luo, J., Gilbert, L., Qu, C., Wilson, J., Bristow, D., Landers, R., and Kinzel, E., 2015, "Wire-Fed additive manufacturing of transparent glass parts," ASME 2015 International Manufacturing Science and Engineering Conference, ASME, Charlotte, NC, USA, p. V001T002A108.

[20] Luo, J., Gilbert, L., Qu, C., Morrow, B., Bristow, D., Landers, R., Goldstein, J., Urbas, A., and Kinzel, E., 2015, "Solid freeform fabrication of transparent fused quartz using a filament fed process," Annual International Solid Freeform Fabrication Symposium, University of Texas, Austin, TX, pp. 122-133.

[21] Luo, J., Gilbert, L. J., Qu, C., Landers, R., Bristow, D., and Kinzel, E., 2016, "Additive manufacturing of transparent soda-lime glass using a filament-fed process," Journal of Manufacturing Science and Engineering.

[22] Luo, J., Gilbert, L. J., Bristow, D. A., Landers, R. G., Goldstein, J. T., Urbas, A. M., and Kinzel, E. C., 2016, "Additive manufacturing of glass for optical applications," SPIE LASE, International Society for Optics and Photonics, pp. 97381-97389.

[23] Luo, J., Gilbert, L. J., Peters, D. C., Bristow, D. A., Landers, R. G., Goldstein, J. T., Urbas, A. M., and Kinzel, E. C., 2016, "Bubble formation in additive manufacturing of glass," SPIE Defense+ Security, International Society for Optics and Photonics, pp. 982214-982214-982216.

[24] Luo, J., Bender, T., Bristow, D., Landers, R., Goldstein, J., Urbas, A., and Kinzel, E. C., 2016, "Bubble formation in additive manufacturing of borosilicate glass," 2016 Annual International Solid Freeform Fabrication Symposium, University of Texas, Austin, TX, pp. 998-1003.

[25] 2007, Schott AG, DURAN® Edition 4 Laboratory Glassware Catalogue German / English, Chapter 9, P. 185-245

[26] Seward III, T. P., and Vascott, T., 2005, High temperature glass melt property database for process modeling, Wiley-American Ceramic Society.

[27] Allcock, G., Dyer, P., Elliner, G., and Snelling, H., 1995, "Experimental observations and analysis of CO_2 laser-induced microcracking of glass," Journal of applied physics, 78(12), pp. 7295-7303.

[28] Bol’shepaev, O. Y., and Katomin, N. N., 1997, "Laser polishing of glass articles," Glass and Ceramics, 54(5), pp. 141-142.

[29] Vega, F., Lupo´n, N. r., Cebrian, J. s. A., and Laguarta, F., 1998, "Laser application for optical glass polishing," OPTICE, 37(1), pp. 272-279.

[30] Jung, S., Lee, P. A., and Kim, B. H., 2016, "Surface polishing of quartz-based microfluidic channels using CO_2 laser," Microfluidics and Nanofluidics, 20(6), p. 84.

[31] Rubin, M., 1985, "Optical properties of soda lime silica glasses," Solar energy materials, 12(4), pp. 275-288.

[32] Lee, Y.-I., Song, K., and Sneddon, J., 2000, Laser-induced breakdown spectrometry, Nova Publishers.

SECTION

2. CONCLUSIONS

This dissertation explored two different techniques for AM of glass: SLM and filament fed process. Semi-transparent parts were able to be printed with SLM process, which shows the potential for printing fully transparent glass parts. Compared with SLM technique, filament fed process is more robust and promising. Therefore, the following studies were focused on the filament fed process.

The filament fed process for printing different types of glass were studied, including soda lime glass, fused quartz and borosilicate glass. This technique was able to print 3D multilayer, fully transparent glass without voids between layers, which was not achieved with other techniques.

For soda lime glass, single walls were printed, and the transmissivity of the best sample is as good as furnace cast sample using the same filaments. The bubble formation in soda lime glass was also studied. Different regimes of bubble formation that corresponding to different process parameters were discovered.

Fully transparent 3D fused quartz parts were printed with the filament fed process, both the transmissivity and index homogeneity were nearly as good as normal fused quartz. The mass and energy balance model created for fused quartz printing agrees with the experiments and can predict the occurrence of vaporization of glass.

In addition to printing of 3D cubes, samples with convex cylindrical and spherical surface were printed using borosilicate glass. The optical quality of printed borosilicate glass was measured to be as good as conventional manufactured glass. Furthermore, the cylindrical samples were proved to be able to function as cylindrical lenses.

BIBLIOGRAPHY

[1] Pereira, T., Rusinkiewicz, S., and Matusik, W., 2014, "Computational Light Routing: 3D Printed Optical Fibers for Sensing and Display," ACM Transactions on Graphics (TOG), 33(3), p. 24.

[2] Willis, K., Brockmeyer, E., Hudson, S., and Poupyrev, I., 2012, "Printed optics: 3d printing of embedded optical elements for interactive devices," Proceedings of the 25th annual ACM symposium on User interface software and technology, ACM, Cambridge, MA, Oct. 7-10, pp. 589-598.

[3] Brockmeyer, E., Poupyrev, I., and Hudson, S., 2013, "PAPILLON: designing curved display surfaces with printed optics," Proceedings of the 26th annual ACM symposium on User interface software and technology, ACM, St. Andrews, Scotland, United Kingdom, Oct. 8-11, pp. 457-462.

[4] Urness, A. C., Moore, E. D., Kamysiak, K. K., Cole, M. C., and McLeod, R. R., 2013, "Liquid deposition photolithography for submicrometer resolution three-dimensional index structuring with large throughput," Light: Science & Applications, 2(3), p. e56.

[5] Niino, T., and Yamada, H., 2009, "Fabrication of Transparent Parts by Laser Sintering Process:-Transparentization of laser sintered plastic parts by infiltrating thermosetting epoxy with tuned refractive index," Journal of the Japan Society for Precision Engineering, 75(12), pp. 1454-1458.

[6] Marder, S. R., Brédas, J.-L., and Perry, J. W., 2007, "Materials for multiphoton 3D microfabrication," Mrs Bulletin, 32(07), pp. 561-565.

[7] Blessing, K., 2014, "Print head, upgrade kit for a conventional inkjet printer, inkjet printer and method for printing optical structures," U.S. Patent No. 8,840,235. (23 September 2014).

[8] Weber, M. J., 2002, Handbook of optical materials, CRC press, Boca Raton, FL.

[9] Khmyrov, R., Grigoriev, S., Okunkova, A., and Gusarov, A., 2014, "On the possibility of selective laser melting of quartz glass," Physics Procedia, 56, pp. 345-356.

[10] Klocke, F., McClung, A., and Ader, C., 2004, “Direct Laser Sintering of Borosilicate Glass,” Solid Freeform Fabrication Symposium Proceedings, Austin, TX, Aug. 3–5, pp. 214–219.

[11] Fateri, M., and Gebhardt, A., 2015, "Selective Laser Melting of Soda - Lime Glass Powder," International Journal of Applied Ceramic Technology, 12(1), pp. 53-61.

[12] Luo, J., Pan, H., and Kinzel, E. C., 2014, "Additive Manufacturing of Glass," Journal of Manufacturing Science and Engineering, 136(6), p. 061024.

[13] Fu, Q., Saiz, E., and Tomsia, A. P., 2011, "Bioinspired strong and highly porous glass scaffolds," Advanced functional materials, 21(6), pp. 1058-1063.

[14] Klein, S., Simske, S., Adams, G., Parraman, C., Walters, P., Huson, D., and Hoskins, S., 2012, "3D Printing of Transparent Glass," Proc. NIP & Digital Fabrication Conference, Society for Imaging Science and Technology, Quebec City, Canada, Sep. 9-13, pp. 336-337.

[15] Marchelli, G., Prabhakar, R., Storti, D., and Ganter, M., 2011, "The guide to glass 3D printing: developments, methods, diagnostics and results," Rapid Prototyping Journal, 17(3), pp. 187-194.

[16] Mok, S. H., Bi, G., Folkes, J., Pashby, I., and Segal, J., 2008, "Deposition of Ti–6Al–4V using a high power diode laser and wire, Part II: Investigation on the mechanical properties," Surface and Coatings Technology, 202(19), pp. 4613-4619.

VITA

Junjie Luo was born in October, 1985 in Hunan Province, China. He received his Master of Science degree in Thermal Engineering in June 2011 from Chinese Academy of Sciences, China. In June 2008, he received his Bachelor of Engineering degree in Thermal Engineering from North China Electric Power University, China. He received his Ph.D. in Mechanical Engineering from Missouri University of Science and Technology in May 2017.